

# Modelling of Electrode Swelling in Lithium-ion Batteries

Master's thesis in Applied Mechanics

Anush Rajesh Matty

---

Division of Material and Computational Mechanics

CHALMERS UNIVERSITY OF TECHNOLOGY

Gothenburg, Sweden 2025

[www.chalmers.se](http://www.chalmers.se)



MASTER'S THESIS 2025

# Modelling of Electrode Swelling in Lithium-ion Batteries

Anush Rajesh Matty



Department of Industrial and Materials Science  
*Division of Material and Computational Mechanics*  
CHALMERS UNIVERSITY OF TECHNOLOGY  
Gothenburg, Sweden 2025

Modelling of Electrode Swelling in Lithium-ion Batteries  
Anush Rajesh Matty

© Anush Rajesh Matty, 2025.

Supervisors: David Carlstedt and Peter Gustavsson, Volvo Car Corporation  
Supervisor and Examiner: Fredrik Larsson, Department of Industrial and Materials Science

Master's Thesis 2025  
Department of Industrial and Materials Science  
Division of Material and Computational Mechanics  
Chalmers University of Technology  
SE-412 96 Gothenburg

Cover: Schematic illustration of lithiation and delithiation induced swelling and shrinking of the electrodes.

Typeset in L<sup>A</sup>T<sub>E</sub>X  
Printed by Chalmers Reproservice  
Gothenburg, Sweden 2025

Modelling of Electrode Swelling in Li-ion Batteries

Anush Rajesh Matty

Department of Industrial and Materials Science

Division of Material and Computational Mechanics

Chalmers University of Technology

## Abstract

As the global adoption of electric vehicle (EV) technology accelerates, the demand for safe, sustainable, and reliable battery technologies has increased. Currently, lithium-ion batteries offer the most promising option due to their high energy density and long cycle life. However, a significant concern with lithium-ion batteries is their tendency to swell during operation. This swelling is not just a cosmetic issue; it can seriously impact the battery's efficiency and safety. When battery cells swell, they may experience a reduction in energy storage capacity, which affects the overall performance of the vehicle. Additionally, this expansion can lead to mechanical failures or even pose fire hazards if not properly managed. Since the effects of swelling are long term in nature, physically testing the batteries can be both expensive and time consuming. Therefore, there is a need to develop virtual testing models to analyze the mechanical response of battery cells while considering the effects of swelling.

This study builds on the previous work and research done in the Battery Structural & Thermal Simulation department at Volvo Cars and aims to develop a methodology for predicting the mechanical response of battery cells by integrating the effects of state of charge induced swelling using a coupled electrochemical-mechanical simulation. A multiscale modeling approach is utilized to analyze the battery at micro, meso, and macro scale levels. At the microscale, the mechanical response to particle-level expansion is examined, and an effective swelling coefficient is determined through virtual tests. This effective swelling coefficient is then scaled up to the mesoscale, where coupled electrochemical and mechanical simulations are conducted to assess the impact of lithium insertion on the expansion at the electrode level. Finally, this effective expansion is further upscaled to capture the volume changes occurring at the cell level. The developed methodology in this work can be further utilized to analyze the pack or module level swelling.

A key limitation of the developed framework is that it only accounts for swelling induced by change in the state of charge. Consequently, additional work is needed to enhance the model by incorporating swelling caused by lithium plating, degradation of the solid electrolyte interphase (SEI) layer, and gas generation. These factors have a significant impact on the cell's long-term response and require further investigation.

Keywords: Finite Element Analysis, Lithium-ion batteries, State of Charge, Swelling, Multiscale model, Multiphysics simulation.



## Acknowledgements

I would like to express my deepest gratitude to my supervisors, David Carlstedt and Peter Gustavsson, for their exceptional support and guidance throughout this thesis. Their deep expertise in battery technology and finite element modeling has been instrumental in shaping both the direction of my research and my growth as an engineer. I am sincerely thankful for their generous sharing of knowledge, thoughtful feedback, and continuous encouragement.

I am also profoundly grateful to Professor Fredrik Larsson, my supervisor and examiner, whose invaluable insights and unwavering support have significantly enriched this work. His patience, kindness, and mentorship have been both motivating and deeply appreciated.

My heartfelt thanks to Marie-Louise Holmer, my engineering manager at Volvo Cars, for granting me the opportunity to pursue this thesis within the company. I am equally thankful to the entire FEM team at Volvo Cars for technical advice, camaraderie, and day-to-day support that have meant a great deal throughout this journey.

To my parents, I owe immense thanks for their constant encouragement and belief in me. Their unwavering support has been a source of strength and motivation during the most challenging moments of the past six months.

Lastly, I would like to extend my sincere appreciation to my family and close friends for their patience, understanding, and emotional support. Your presence and positivity have helped me stay grounded and focused, and I am truly grateful for that.

Anush Rajesh Matty, Gothenburg, 05 2025



# List of Acronyms

Below is the list of acronyms that have been used throughout this thesis:

CAD	Computer aided design
EV	Electric vehicle
Li-ion	Lithium ion
SOC	State of charge
NMC	Lithium nickel manganese cobalt oxides
LFP	Lithium iron phosphate
PP	Polypropylene
PE	Polyethylene
DFT	Density functional theory
DFN	Doyle-Fuller-Newman
RVE	Representative volume element
PBC	Periodic boundary condition
SEI	Solid-electrolyte interface
OCP	Open circuit potential
NCA	Lithium nickel cobalt aluminium oxides
ECM	Equivalent Circuit Models
PDE	Partial differential equations
BMS	Battery management systems
P2D	Pseudo 2 dimension
P4D	Pseudo 4 dimension
BFGS	Broyden–Fletcher–Goldfarb–Shanno



# Contents

<b>List of Acronyms</b>	<b>viii</b>
<b>1 Introduction</b>	<b>1</b>
1.1 Background . . . . .	1
1.2 Aim and approach . . . . .	2
1.3 Scope and limitations . . . . .	2
<b>2 Theory</b>	<b>3</b>
2.1 Battery overview . . . . .	3
2.1.1 Components present in Li-ion batteries . . . . .	3
2.1.2 Working principle of Li-ion battery . . . . .	4
2.1.3 State of charge induced effects . . . . .	5
2.1.4 Quantification of state of charge induced effects . . . . .	7
2.2 Fully coupled electrochemical mechanical problem . . . . .	11
2.2.1 Electrochemical model . . . . .	11
2.2.2 Doyle-Fuller-Newman model . . . . .	11
2.2.2.1 Movement of the Li-ions between the electrode and electrolyte phase. . . . .	13
2.2.2.2 Li-ion diffusion in electrolyte phase . . . . .	14
2.2.2.3 Electron conduction in the electrode phase . . . . .	15
2.2.2.4 Diffusion of lithium in the microscale . . . . .	16
2.2.2.5 Coupling between the microscale and continuum scale. . . . .	17
2.2.2.6 Swelling of the active particles . . . . .	17
2.2.3 Mechanical model . . . . .	19
2.2.4 Thermal Model . . . . .	20
2.3 Mechanical material modeling of battery components . . . . .	21
2.3.1 Constitutive models . . . . .	22
2.3.1.1 Elastic-plastic with isotropic hardening material model	23
2.3.1.2 Crushable foam material model . . . . .	26
2.3.2 Material calibration . . . . .	28
2.3.2.1 Optimization algorithms and error measures . . . . .	29
2.3.3 Multiscale modelling and homogenization . . . . .	30
2.3.3.1 Periodic boundary conditions . . . . .	31
<b>3 Methodology</b>	<b>34</b>
3.1 Modeling framework overview . . . . .	34

---

3.2	Microscale modeling: particle level response . . . . .	35
3.2.1	Geometry and finite element model . . . . .	35
3.2.2	Constitutive model . . . . .	37
3.2.2.1	Linear material model . . . . .	37
3.2.2.2	Non-linear material model . . . . .	38
3.2.3	Boundary condition . . . . .	39
3.2.4	Load cases . . . . .	39
3.2.4.1	Load case 1: To characterize a homogenized response of the RVE . . . . .	40
3.2.4.2	Load case 2: To characterize effective response of the RVE due to the swelling of the inclusion . . . . .	40
3.3	Up-scaling to mesoscale: Effective swelling coefficient determination .	42
3.3.0.1	Case 1: Linear elastic constitutive model . . . . .	42
3.3.0.2	Case 2: Non-linear constitutive model . . . . .	43
3.4	Mesoscale modeling: Electrode-level response . . . . .	44
3.4.1	Geometry and finite element model setup . . . . .	44
3.4.2	Constitutive model . . . . .	46
3.4.2.1	Material characterization: Experimental test setup .	46
3.4.2.2	Material calibration . . . . .	47
3.4.3	Electrochemical material description . . . . .	50
3.4.3.1	Electrolyte properties . . . . .	51
3.4.3.2	Electrode properties . . . . .	52
3.4.3.3	Separator properties . . . . .	54
3.4.4	Mechanical boundary condition . . . . .	55
3.4.4.1	Periodic boundary conditions . . . . .	55
3.4.4.2	Symmetry boundary conditions . . . . .	55
3.4.5	Initial condition . . . . .	57
3.4.6	Loading condition and simulation setup . . . . .	58
3.4.7	Upscaling to macroscale: Effective volume change determination	59
3.5	Macroscale modeling: Cell level response . . . . .	59
3.5.1	Geometry and model setup . . . . .	60
3.5.2	Constitutive model . . . . .	61
3.5.3	Boundary condition and loads . . . . .	62
<b>4</b>	<b>Results and discussion</b>	<b>64</b>
4.1	Microscale model . . . . .	64
4.1.1	Case 1: Linear elastic constitutive model . . . . .	64
4.1.1.1	Load case 1: Homogenized material response . . . . .	64
4.1.1.2	Load case 2: Effective response due to lithiation . . . . .	69
4.1.2	Case 2: Non-linear constitutive model . . . . .	74
4.1.2.1	Load case 1: Homogenized material response . . . . .	74
4.1.2.2	Load case 2: Effective response due to lithiation . . . . .	81
4.1.3	Comparison between effective swelling coefficients computed from linear elastic and non-linear constitutive models . . . . .	86
4.2	Mesoscale model . . . . .	87
4.2.1	Material characterization: Tested response . . . . .	87

4.2.2	Material calibration . . . . .	90
4.2.3	Coupled Electrochemical-mechanical simulation . . . . .	93
4.2.3.1	Mechanical response under periodic boundary condition . . . . .	93
4.2.3.2	Mechanical response under symmetry boundary condition . . . . .	98
4.2.3.3	Swelling effects comparison between periodic and symmetry boundary condition . . . . .	102
4.3	Macroscale model . . . . .	104
4.3.1	Homogenized material model characterization . . . . .	104
4.3.2	Cell level swelling response . . . . .	105
<b>5</b>	<b>Conclusion</b>	<b>108</b>
<b>6</b>	<b>Future scope</b>	<b>110</b>
<b>A</b>	<b>Appendix A: Electrochemical definitions</b>	<b>113</b>
<b>B</b>	<b>Appendix B: Calibrated material properties of electrodes and separator</b>	<b>115</b>
<b>References</b>		<b>119</b>

# 1

## Introduction

### 1.1 Background

The rise of electric vehicles (EVs) has profoundly transformed the automotive industry, reshaping consumer expectations and market dynamics. As demand for EVs continues to increase, the necessity for efficient, safe, and sustainable energy storage solutions has become increasingly important. Among various energy storage technologies, lithium-ion batteries have emerged as the leading choice, due to their (i) high energy density, which facilitates longer driving ranges, (ii) extended cycle life for improved longevity and reliability, and (iii) low self-discharge rate, which helps minimize energy loss when the vehicle is inactive. However, the widespread adoption of lithium-ion batteries has brought new challenges, particularly in ensuring their safety and mechanical integrity under both operational and abuse conditions.

Several advanced modelling techniques and previous research has provided valuable insights into simulating and predicting the behavior of lithium-ion batteries under conditions of mechanical, thermal and electrical abuse. For instance, investigations conducted by Sahraei et al. [1] have examined the deformation patterns and failure sequences of the microstructural components within battery cells subjected to diverse mechanical loading conditions. Spotnitz et al. [2] have simulated the impact of thermal abuse showing how the overcharge conditions and localized heating can cause internal short circuits and potentially trigger thermal runaway. Zhang et al. [3] investigated the consequences of high C-rate charging, highlighting how lithium plating and instability of the solid electrolyte interphase (SEI) layer contribute to performance degradation and heightened safety risks .Various such works in literature are available that focus on analyzing the responses of batteries under diverse conditions.

Nevertheless, it is essential to acknowledge that the response of the batteries to external loads evolves over time due to the state of charge (SOC) induced material property changes and aging. In addition to this, electrode swelling due to intercalation, lithium plating, SEI layer degradation, and gas generation can significantly affect the structural integrity of the cell. Electrode swelling is particularly challenging as it impacts pack-level integration, thermal management, and overall cell design. Therefore, to accurately predict battery behavior under operational or abuse conditions, it is essential to incorporate these evolving material properties and swelling effects into modeling frameworks. This report focuses on developing a methodology

for predicting the mechanical response of the battery at the cell level, considering the swelling effects induced by change in the SOC.

## 1.2 Aim and approach

The main objective of this thesis project is to develop a methodology to predict the mechanical response of the batteries at cell level by incorporating the state of charge induced swelling. The developed model can then be used to understand the effect of the cell level swelling on the module and battery pack level. The aim of this thesis mainly includes the following:

- To investigate available computational models to predict the mechanical response of the cell and calibrate the material model parameters for the quasi-static case.
- To explore finite element representations for different battery cell designs and configuration.
- To study the electro-chemical model to simulate the change in SOC and analyze the effect of SOC on the mechanical response of the cell.
- To perform sensitivity analysis of model parameters through available cell/-material data.
- Validate the simulation result with available experimental data.

## 1.3 Scope and limitations

The scope and limitations of this thesis work are listed below without any specific order:

- This thesis work builds upon the previous related work [4], [5] and [6] conducted in the department.
- The developed methodology in this work only considers the swelling induced by lithium intercalation and deintercalation. Other effects that causes swelling like lithium plating, SEI layer degradation, gas generation and temperature are neglected.
- Change in the stiffness of the electrodes due to the lithium intercalation has not been considered.
- The electrochemical-mechanical simulation in *3DEXPERIENCE* uses two way coupling. But in this work, the effect of swelling on the electrochemical response is not studied.
- Failure of the components due to swelling effects is not considered in the study.
- The thermal effects induced during lithiation and delithiation and their effect on the swelling is not studied.
- Characterizing the mechanical response of the microstructure of the electrodes were limited to a homogenized matrix and active particles. Porosity, conductive additives and electrolyte are not explicitly modelled.
- Only the galvanostatic charging case is considered throughout the work. Galvanostatic discharge or potentiostatic cases are not considered.

# 2

## Theory

### 2.1 Battery overview

Batteries are electrochemical devices that generate electrical energy through redox reactions. Certain types of batteries can reverse this process, converting electrical energy back into chemical energy; these are known as secondary cells, while non-rechargeable batteries are referred to as primary cells. The ability to recharge secondary cells offers numerous advantages, extending their use in commercial applications such as electric vehicles. The rechargeability of a battery primarily depends on its cell chemistry, which plays a crucial role in determining the energy density, safety, and reliability of the cell. Among the various available chemistry options, lithium-ion (Li-ion) batteries are the most viable due to their high energy density, long cycle life, and reliability. Commercially available batteries come in various sizes and form factors, as shown in Figure 2.1. For electric vehicle applications, form factors are carefully selected based on required energy density and packaging constraints. To achieve the necessary power and voltage, cells are typically arranged in series and parallel within a module, and multiple modules are combined to form a battery pack.

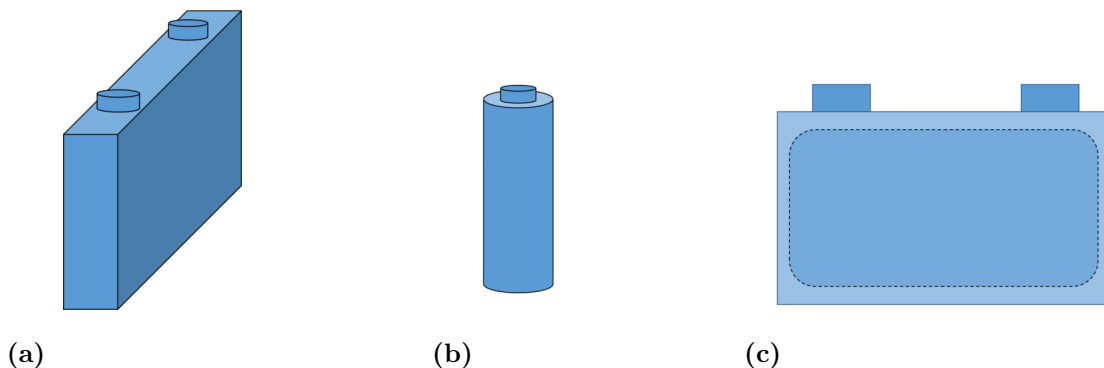


**Figure 2.1:** Schematic illustration showing different battery form factors (a) prismatic cell (b) cylindrical cell (c) pouch cell, reprint from [6].

#### 2.1.1 Components present in Li-ion batteries

Li-ion batteries typically contain two electrodes: a positive electrode (cathode) and a negative electrode (anode). These electrodes are composed of active particles coated onto current collectors. Various binders are used to ensure that the active particles

adhere properly to the current collectors, while additives are included to enhance electrical conductivity. To prevent physical contact between the two electrodes, which can lead to an internal short circuit, separators are commonly employed to maintain their distance from each other [4]. The electrodes are immersed in an electrolytic solution, which facilitates the flow of Li-ions between them. The thickness of the positive and negative electrodes is typically in the range of 100-200  $\mu m$ , with metal foils contributing up to 10-15  $\mu m$ , and the separator is about 10-25  $\mu m$  [7]. Currently, lithium iron phosphate (LFP) and lithium nickel manganese cobalt oxides (NMC) are widely used as positive electrode active materials, with aluminum serving as the positive current collector. Graphite is commonly used for the negative electrode active material, with copper as the negative current collector, and polypropylene (PP) and polyethylene (PE) are used for the separator.

Typically, battery cells contain multiple layers of electrodes and separator stacked on top of each other, a configuration often referred to as "jelly-rolls". These layers can be arranged in various ways, as shown in Figure 2.2.

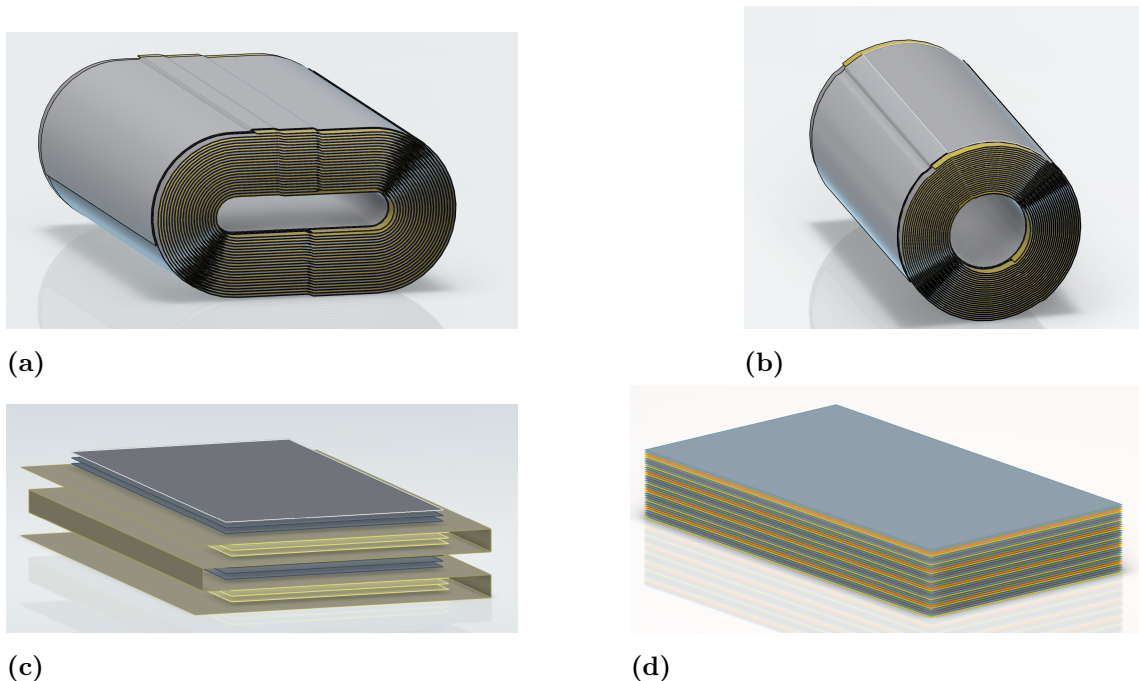
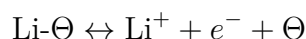


**Figure 2.2:** Figures illustrating various jelly-roll configuration (a) prismatic winding (b) cylindrical winding (c) Z-stacking (d) Single sheet stacking created using *Layered Product Design* app in *3DEXPERIENCE*.

### 2.1.2 Working principle of Li-ion battery

Figure 2.3 depicts the charging phase of the Li-ion batteries. During charging, the Li-ions are extracted from the positive electrode (cathode) and enter into the electrolyte through a reaction process that can be written as



Where,  $\text{Li}-\Theta$  represents lithium in the positive electrode. Due to the applied current, the reaction takes place leaving behind the Li-ions in the electrolyte  $\text{Li}^+$ , electron  $e^-$  and vacancy in the positive electrode  $\Theta$  [8]. These Li-ions in the electrolyte pass through the separator and intercalate at the negative electrode (anode). It is important to note that the separator is ionically conductive but electrically insulated [4]. Consequently, electrons migrate via the current collectors. During the discharge phase, the flow of of Li-ions is reversed i.e. Li-ions migrate from the negative electrode to the positive electrode. It should be noted that the Li-ions in the battery domain can exist in both the solid electrode phase and in the electrolyte phase.

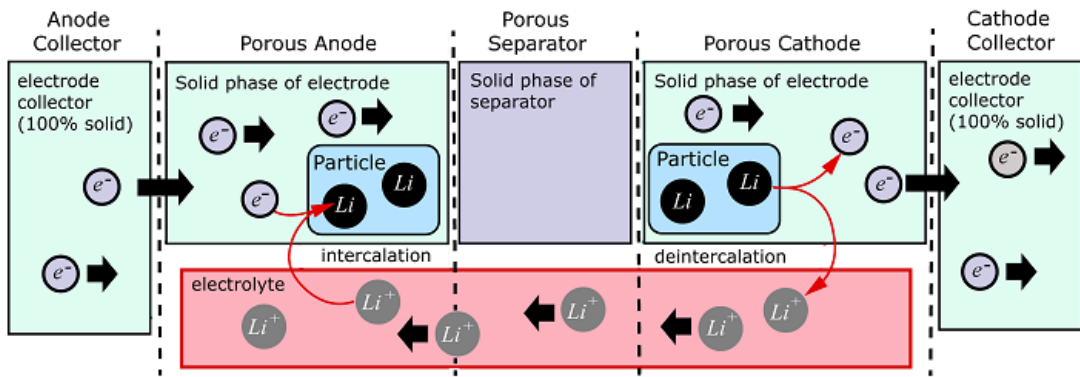


**Figure 2.3:** Schematic diagram depicting the charging process in Li-ion batteries, reprint from [8].

### 2.1.3 State of charge induced effects

The fundamental working mechanism of Li-ion batteries is based on the intercalation and deintercalation of Li-ions into and out of the active electrode materials. The amount of intercalated Li-ions is commonly quantified using a parameter known as the SOC. The SOC is a critical indicator that reflects the amount of usable energy remaining in the battery, typically expressed as a percentage of the cell's total capacity. An increase in SOC corresponds to a higher degree of lithiation at the negative electrode, whereas a decrease indicates delithiation.

This cyclic lithiation and delithiation process causes volumetric changes in the active materials, commonly referred to as intercalation-induced swelling. While this swelling is generally reversible during normal charge-discharge cycles, repeated cycling over time can lead to mechanical degradation, including particle cracking, electrode delamination, and structural fracture [1]. These mechanical changes can compromise both the performance and safety of the cell. Due to the cyclic swelling, the response of the battery to the external load is not linear in nature but has the cyclic behavior as depicted in Figure 2.4.

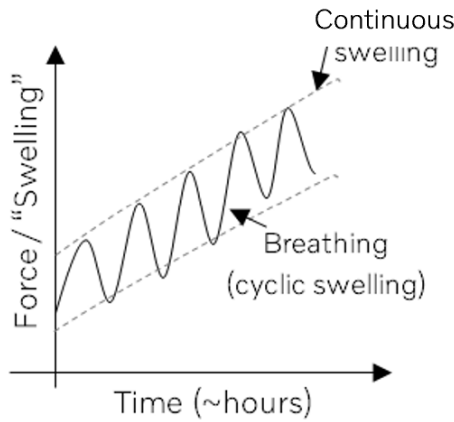


**Figure 2.4:** Evolution of swelling force with respect to time.

The swelling mechanisms in lithium-ion batteries can be broadly classified into reversible and irreversible swelling [6]. Reversible swelling is directly associated with lithium intercalation into the electrode matrix and typically contracts back upon discharge. In contrast, irreversible swelling arises from side reactions such as the growth of the SEI layer, gas evolution, and electrolyte decomposition, which are especially prominent under high-temperature conditions, overcharging, or aging [2]. These irreversible phenomena can lead to a progressive increase in internal pressure, potentially deforming the battery casing and leading to pack-level complications such as mechanical interference, loss of contact, and decreased safety margins.

Apart from the swelling of the active particles, the intercalation process also influences the material properties of the electrodes such as strength and stiffness. Particularly, these effects are observed for the negative electrode materials. The Figure 2.5 depicts the change in the stiffness of various electrode material as a function of Li-ion concentration as reported by Qi et al. [9].

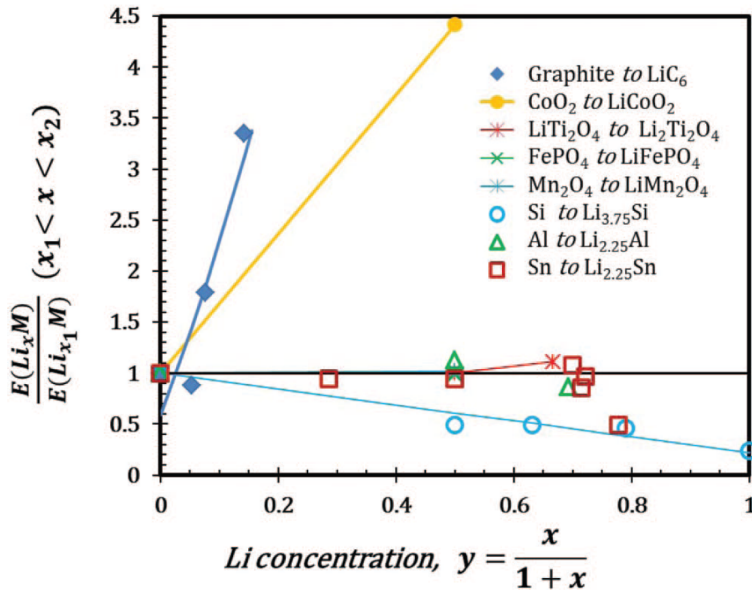


**Figure 2.5:** Evolution of the normalized elastic modulus as a function of lithium concentration for various electrode materials. The x-axis represents the lithium concentration, defined as  $y = \frac{x}{1+x}$ , where  $x$  is the stoichiometric coefficient in  $\text{Li}_x\text{M}$  and M denotes the host material. The y-axis shows the averaged elastic modulus at a given lithium concentration  $x$ , normalized by the modulus of the fully delithiated phase ( $\text{Li}_{x_1}\text{M}$ ). This captures the elastic property evolution of the material as it undergoes lithiation from  $x_1$  to  $x_2$ , which may involve phase transformations. Reprinted from [9].

As illustrated in Figure 2.5, lithium insertion does not universally lead to material stiffening; in some cases, it actually causes softening. Additionally, many electrode materials exhibit a ductile-to-brittle transition as a result of lithium intercalation. This behavior can be predicted using the Pugh criterion, which states that a material is likely to behave in a brittle manner if the ratio of its bulk modulus to shear modulus (B/G) is less than 1.75, and in a ductile manner if the ratio exceeds 1.75 [9]. The changes in mechanical properties associated with lithium insertion can be effectively calculated through density functional theory (DFT) methods, as demonstrated in [9].

#### 2.1.4 Quantification of state of charge induced effects

To measure and quantify the swelling of lithium-ion batteries, tests like free-swelling, ball-indenter constrained swelling, and plate-constrained swelling are commonly used. The typical setups for these tests are shown in Figure 2.6.

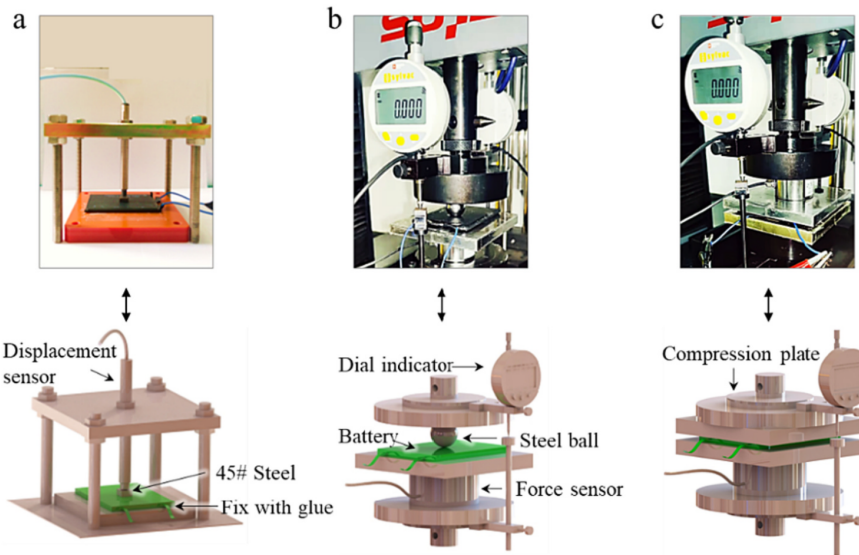


**Figure 2.6:** Swelling test rigs for (a) free swelling, (b) ball constrained swelling, (c) plate constrained swelling, reprint from [10].

In a free-swelling test, the battery is charged and discharged without any external mechanical constraints while placed on the test rig. A sensor placed on the rig tracks the thickness change. This gives a clear view of how the battery naturally expands during cycling.

However, in real application, batteries are usually housed in packs where components like compression pads and support structures (e.g, battery modules or pack trays) apply mechanical constraints. To simulate these effects, constrained swelling tests such as the ball-indenter and plate-constrained setups are used. The ball-indenter test focuses on how localized pressure affects swelling, while the plate-constrained test applies a more uniform constraint, similar to what batteries experience inside a tightly packed module. Through swelling experiments Cao et al. [10] analyzed how lithium-ion battery deformation and internal stress evolve during charging, under both free and constrained conditions. One of their key findings was that the negative electrode's swelling behavior is highly dependent on the SOC, especially around SOC 0.29, which marks a phase transition in the graphite structure. They also found that mechanical boundary conditions such as preload force, fixture stiffness, and surface contact area strongly influence the measured swelling force and internal stress distribution. Their results highlight that swelling is not only a material driven phenomenon but is also highly sensitive to how the battery is mounted and constrained.

In addition to mechanical tests, techniques such as Scanning Electron Microscopy (SEM) and X-ray Computed Tomography (CT) are widely used to measure swelling and structural changes at the electrode level.

Beyond experimental approaches, Finite Element (FE) modeling has become a valuable tool for simulating and predicting battery swelling behavior. Various modeling strategies have been proposed in the literature, with the choice of method typi-

cally governed by a trade-off between modeling accuracy, computational cost, and the availability of experimental data. A common and computationally efficient approach involves approximating swelling behavior as an equivalent thermal expansion phenomenon. For instance, the study conducted by Gilaki and Sahraei [11] incorporated volumetric changes by measuring the electrode expansion through physical testing, such as CT scans, and modeling this expansion using a thermal analogy. Although the actual expansion is driven by changes in the state of charge (SOC), it was represented in the model as a pseudo thermal expansion. In this analogy, a fictitious temperature rise corresponding to an increase in SOC was adopted, and the expansion is governed by a thermal like coefficient  $\alpha$ . The thermal coefficient  $\alpha$  was defined as:

$$\alpha = \frac{1}{h} \cdot \frac{\Delta h}{\Delta \text{SOC}} \quad (2.1)$$

Where,  $h$  is the initial thickness of the electrode stack,  $\Delta h$  is the measured thickness change during charging, and  $\Delta \text{SOC}$  is the change in state of charge.

This pseudo-thermal expansion is applied in the FE model to induce volume change of the electrodes. While thermal analogy models offer a convenient and computationally efficient method for simulating battery swelling, their primary limitation lies in the lack of physical fidelity. These models simplify swelling as a thermally induced expansion, which does not fully capture the SOC dependent and electro-chemically coupled nature of real intercalation induced strain.

To account for the electrochemical influences in simulating swelling phenomena, recent research has increasingly focused on physics-based modeling approaches, where swelling is directly linked to the lithium-ion concentration distribution within the electrodes. These models incorporate the coupling between Li-ion concentration and mechanical deformation, allowing for a more accurate representation of intercalation-induced swelling. For instance Wang et al. [12] developed an electrochemical-mechanical coupled multi-scale modeling method to predict the full-field stress distribution in commercial lithium-ion pouch cells during operation. By combining a mesoscale electrochemical model for a single battery unit with a macroscale mechanical model for the entire cell, and applying a real-time data mapping technique, the method was validated against experimental surface pressure measurements. Various such literature are available that have focused on modelling swelling behavior using physics based modeling approach.

However, a gap in the existing literature is the lack of a comprehensive methodology that accounts for the influence of binders on active particle swelling and the subsequent upscaling of this effect to predict cell-level volume changes. The primary focus of this work is to address and bridge this research gap.

Unlike swelling tests, which are typically non-destructive, quantifying the effect of SOC on the mechanical properties of battery materials requires destructive testing, such as uniaxial or sometimes biaxial loading experiments. These tests are essential for characterizing how electrode materials respond to mechanical stress at different

levels of lithium insertion. However, due to safety risks especially at high SOC, where fully lithiated electrodes can be chemically unstable and prone to thermal or mechanical failure, testing at or near 100% SOC is often not feasible.

Several studies have therefore focused on characterizing the mechanical response of electrode materials at lower SOC levels. For example, Wang et al. [13] investigated the mechanical behavior of both negative and positive electrodes extracted from commercial 18650 NCA/graphite lithium-ion cells, with a particular emphasis on the influence of SOC. The experimental characterization was conducted along both the axial direction of the jellyroll and the rolling direction of the electrode layers. Their results showed that the negative electrode's stiffness and strength increased significantly with SOC, as illustrated in Figure 2.7, while the positive electrode exhibited almost no noticeable SOC dependency. At low SOC, the negative electrode displayed typical elastic-plastic behavior, but as SOC increased, the material became stiffer and more brittle, with a clear transition to elastic-brittle behavior observed beyond SOC 0.3. Due to safety concerns, the authors limited their mechanical testing to SOC values below 0.3.

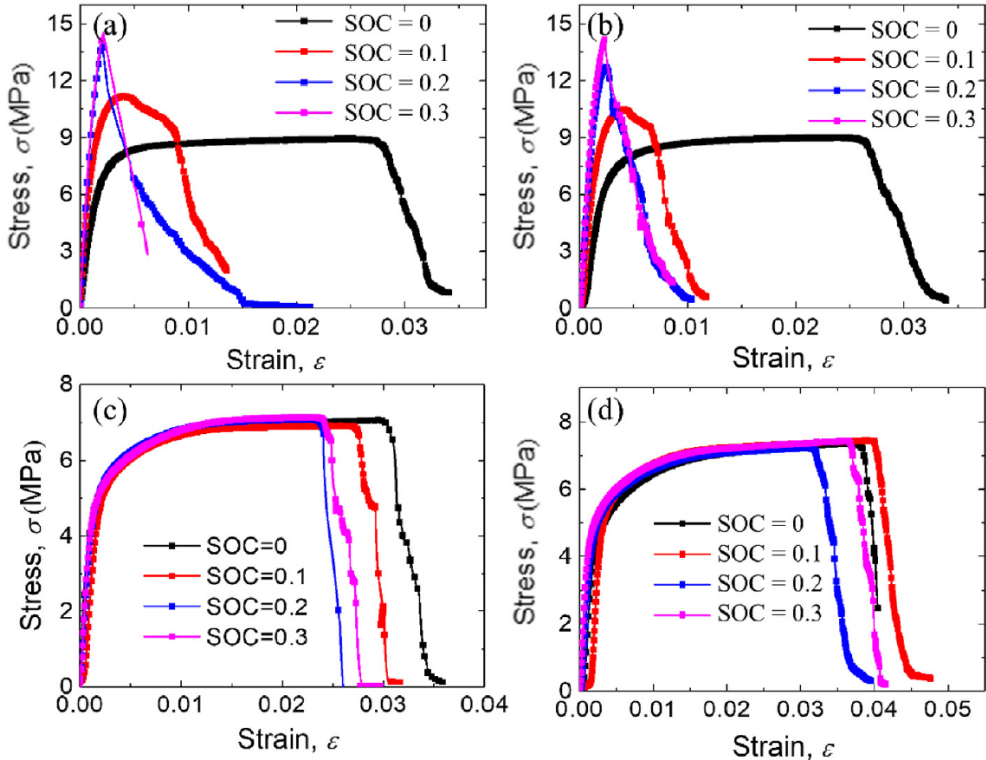


**Figure 2.7:** Tensile stress strain curve at various SOC for a) Negative electrode along the axial direction of the jellyroll, b) Negative electrode along the rolling direction of the jellyroll, c) Positive electrode along the axial direction of the jellyroll and d) Positive electrode along the rolling direction of the jellyroll, reprinted from [13].

## 2.2 Fully coupled electrochemical mechanical problem

As depicted above, the lithiation and delithiation processes are governed by electrochemical reactions that, in turn, induce significant mechanical and structural changes within the battery electrodes. This results in a strong coupling between electrochemical behavior and mechanical responses. For instance, the intercalation of lithium into the graphite negative electrode causes volume expansion, leading to stress generation, microcracking, and particle isolation. These mechanical changes can further influence ionic transport, electronic conductivity, and reaction kinetics, creating a two-way feedback loop between the mechanical and electrochemical fields [14].

In addition to electrochemical and mechanical coupling, temperature also plays a critical role in battery behavior. Elevated temperatures can accelerate reaction rates, diffusion processes, and side reactions such as SEI formation. Conversely, mechanical degradation, such as particle cracking, can increase internal resistance, leading to localized heating. This introduces thermal field, a third coupling field. Fully coupled electro-chemo-thermo-mechanical models provide a comprehensive framework to capture these interactions. However, in the present work, thermal effects are neglected to reduce complexity and focus is solely on the coupled electrochemical and mechanical interactions.

### 2.2.1 Electrochemical model

To model the electrochemical behavior itself, several approaches exist depending on the desired fidelity and computational cost:

- **Empirical models:** Based on fitting experimental data, these are computationally efficient but lack predictive power outside calibrated conditions. For example Equivalent Circuit Models (ECMs).
- **Physics-based models:** Such as the Doyle-Fuller-Newman (DFN) model, which describe lithium-ion transport, reaction kinetics, and potential distribution across electrodes and electrolyte using partial differential equations (PDEs).
- **Reduced-order models:** These simplify the DFN model using approximations (e.g., Single Particle Model (SPM)) to maintain computational efficiency while retaining physical interpretability.

### 2.2.2 Doyle-Fuller-Newman model

The Doyle-Fuller-Newman (DFN) model is an electrochemical modeling framework rooted in porous electrode theory [15]. This model effectively captures the working

mechanism of lithium-ion batteries through a set of PDEs.

The DFN model incorporates mass and charge conservation laws, which are solved across two primary phases: the electrode phase and the electrolyte phase. One of the key features of the DFN model is its multiscale formulation. At the macroscopic level, the equations are solved separately for positive and negative electrodes by assuming a homogenized porous medium, while at the microscale, additional equations account for lithium-ion diffusion within individual active material particles in each electrodes.

There are several versions of the DFN model, with the Pseudo-2D (P2D) model being one of the most commonly used due to its relatively low computational cost. The P2D model simplifies the more complex DFN framework by reducing the problem's dimensionality. Specifically, it assumes the electrodes can be modeled in one dimension (1D), typically along the thickness direction (out-of-plane), while neglecting variations in the in-plane direction (across the electrode surface). While this simplification reduces complexity, it introduces limitations, particularly when accounting for spatial variations and non-uniformities within the electrode, which can affect the battery's performance.

Recently, a study by Kulathu et al. [16] expanded the P2D model to address this limitation by incorporating the in-plane variations of the electrochemical processes. Their work accounts for the complex geometric details of the electrode previously neglected in the original P2D formulation. By including these in-plane variations, their extended model offers a more accurate representation of the electrochemical behavior within the electrodes, capturing the non-uniform distribution of lithium-ion concentration, current density, and other key factors across the electrode surface. This modified version of the P2D model, referred to as the Pseudo-4D (P4D) model, provides improved simulations of battery performance, especially in cases where in-plane effects are significant.

The core principles and governing equations of the DFN model can be divided into the following five components:

1. Movement of the Li-ions between the electrode and electrolyte phase.
2. Lithium-ion transport (diffusion and migration) within the electrolyte phase.
3. Electron conduction through the electrode phase.
4. Lithium-ion diffusion inside the microscale active material particles.
5. Coupling between the microscale and macroscale (continuum) domains.

A detailed description of the terms used in these equations along with the units is provided in the Appendix A. The governing equations described in this section unless otherwise specified, all fields are assumed to be the functions of spatial location and time. The theoretical framework described in this section is based on the work by Kulathu et al. [16].

It has to be noted here that in the formulation proposed by Kulathu et al. [16], additional physics like pore-mechanics and surface interactions between the different battery components are also considered. But these physics are neglected in this thesis work. Therefore, mathematical treatment for these physics are not presented in this manuscript.

### 2.2.2.1 Movement of the Li-ions between the electrode and electrolyte phase.

During the charging and discharging processes of a battery, electrochemical reactions i.e. intercalation and de-intercalation processes take place at the electrode-electrolyte interface, where Li-ions transfer between the electrode and the electrolyte. This ion intercalation at the electrode-electrolyte interface is governed by the Butler-Volmer equation, which essentially describes the rate at which the ions are extracted or added during charging and discharging. The equation is divided into two parts, each representing the reactions at the negative and positive electrode. These reactions are mainly influenced by the overpotential ( $\eta$ ), which is the additional voltage required to drive the reaction beyond its equilibrium state. The Butler-Volmer current density is given by the equation,

$$I_{BV} = I_0 \left[ \exp\left(\frac{\alpha_a(F\eta - \sigma_m\Omega)}{RT}\right) - \exp\left(\frac{-\alpha_c(F\eta - \sigma_m\Omega)}{RT}\right) \right] \quad (2.2)$$

Where,  $I_0$  represents the exchange current density,  $\eta$  denotes the overpotential, and  $\alpha_a$  and  $\alpha_c$  are the anodic and cathodic charge transfer coefficients, respectively.  $F$  is Faraday's constant,  $R$  is the universal gas constant,  $T$  is the temperature,  $\sigma_m$  represents the hydrostatic stress, and  $\Omega$  is the partial molar volume.

For a coupled problem, electrochemical and mechanical models are formulated in such a way that certain variables evolve during the simulation. One such term in Equation 2.2 is  $\sigma_m\Omega$ , this term accounts for the mechanical stress that influences the electrochemical response. The mean stress  $\sigma_m$  can be calculated as,

$$\sigma_m = \frac{\sigma_{xx} + \sigma_{yy} + \sigma_{zz}}{3} \quad (2.3)$$

Where,  $\sigma_{xx}$ ,  $\sigma_{yy}$  and  $\sigma_{zz}$  are the stresses in the principal directions.

The overpotential  $\eta$  can be computed using the equation,

$$\eta = \phi_s - \phi_e - E_{ocp} - R_{SEI}I_{BV} \quad (2.4)$$

Where,  $\phi_s$  and  $\phi_e$  represent the solid and electrolyte potentials, respectively, and  $E_{ocp}$  is the open-circuit potential. Additionally,  $R_{SEI}$  refers to the resistance of the solid-electrolyte interface (SEI). In this work,  $R_{SEI}$  is ignored by treating  $R_{SEI} = 0$  for simplicity.

The exchange current density  $I_0$  represents the baseline reactivity when there is no overpotential. It can be written as,

$$I_0 = kF c_e^{\alpha_a} c_s^{\alpha_c} (c_{s,max} - c_s)^{\alpha_a} \quad (2.5)$$

Where,  $k$  is the rate constant for anode and cathode materials given as  $k = k_c k_a$ ,  $c_e$  is the Li-ion concentration in the electrolyte phase,  $c_s$  is the Li-ion concentration in the particle surface and  $c_{s,max}$  is the maximum Li-ion concentration in the solid.

### 2.2.2.2 Li-ion diffusion in electrolyte phase

The Li-ions mainly transport via the electrolyte phase. The evolution of the Li-ions over the time in the electrolyte has to be balanced by the net ion flux and reactions occurring at electrode-electrolyte interface. This is ensured by the mass balanced equation, whose strong form is represented as,

$$\frac{\partial(\nu_e c_e)}{\partial t} = -\mathbf{J}_e \cdot \nabla + \frac{a_s I_{BV}}{F} \quad (2.6)$$

Where,  $c_e$  is the Li-ion concentration in the electrolyte phase,  $\nu_e$  is the electrolyte volume fraction,  $a_s$  is the active surface area,  $\mathbf{J}_e$  is the Li-ion flux and  $I_{BV}$  is the Butler-Volmer current density.

The movement of the ions in the electrolyte phase is governed by the Nernst-Plank equation, that accounts for both the diffusion and migration caused by the concentration gradients and electric fields respectively. Due to the microstructure complexity of the electrodes, flow of the Li-ions are hindered. Therefore, the Bruggeman's corrections are also applied on the Nernst-plank equation to modify the bulk diffusivity into an effective diffusivity. The Nernst-Plank equation acts as a constitutive law to the equation 2.6.

The Nernst-Plank equation accounting for the Bruggeman's corrections is given as,

$$\mathbf{J}_e = -D_e^{\text{eff}} \cdot \nabla c_e + \frac{t_+}{F} \mathbf{I}_e + \nu_e c_e \mathbf{V}_e \quad (2.7)$$

Where,  $D_e^{\text{eff}}$  is the effective ion diffusivity,  $t_+$  is transference number,  $\mathbf{V}_e$  is the flow velocity of the electrolyte.

The effective diffusivity  $D_e^{\text{eff}}$  is computed as,

$$D_e^{\text{eff}} = \nu_e^{(1+\alpha)} D_e \quad (2.8)$$

Where,  $\alpha$  is the Bruggeman's coefficient,  $D_e$  is the ionic diffusivity of the electrolyte. The above equation describes the isotropic effective diffusivity. The formulation can also be extended to anisotropic diffusivity case.

As the Li-ions migrate through the electrolyte, they generate the ionic current, therefore, in addition to the conservation of the mass, the charge conservation has to be applied. The conservation of the charge in the strong form is given by,

$$\mathbf{I}_e \cdot \nabla = a_s I_{BV} \quad (2.9)$$

Where,  $\mathbf{I}_e$  is the ionic current density. It has to be noted again here that the active surface area evolves for the coupled problem due to the intercalation related volumetric changes.

The ionic current density in the electrolyte is governed by the modified form of Ohm's law. To account for the microstructural complexities, the Bruggeman's corrections are also used in the modified Ohm's law and equation is given as,

$$\mathbf{I}_e = -\kappa_e^{\text{eff}} \nabla \phi_e + 2\kappa_e^{\text{eff}} \frac{RT}{F} \left( 1 + \frac{d \ln f_{\pm}}{d \ln c_e} \right) (1 - t_+) \nabla \ln c_e \quad (2.10)$$

Where,  $\kappa_e^{\text{eff}}$  is the effective ionic conductivity and  $\frac{d \ln f_{\pm}}{d \ln c_e}$  is the molar activity coefficient. The above equation acts as a constitutive relation to equation 2.9.

The effective ionic conductivity can be computed as,

$$\kappa_e^{\text{eff}} = \nu_e^{(1+\alpha)} \kappa_e \quad (2.11)$$

Where,  $\kappa_e$  is the ionic conductivity in the electrolyte phase and  $\alpha$  is the Bruggeman's exponent. The above equation describes the case of isotropic conductivity.

### 2.2.2.3 Electron conduction in the electrode phase

During the charging and discharging cycles of a Li-ion battery, electrochemical reactions take place at the electrode–electrolyte interface. While Li-ions move through the electrolyte phase to facilitate these reactions, the corresponding electrons are required to flow through the external circuit via electrode to complete the redox reactions. Overall, there has to be a conservation of electrons in the solid phase. The solid phase can be categorized into the active material phase and the metallic current collector phase. The conservation of the electrons in the active material phase is given in the strong form as,

$$\mathbf{I}_s \cdot \nabla = -a_s I_{BV} \quad (2.12)$$

Where,  $\mathbf{I}_s$  represents the current density in the solid phase.

The transport of the electrons within the solid phase of the electrode is described by Ohm's law, which establishes a linear relationship between the current density and the electric potential gradient. In porous battery electrodes, however, the transport of electrons is affected by the microstructural characteristics of the material, particularly the porosity and tortuosity. These structural features hinder direct electron paths, effectively reducing the bulk electrical conductivity of the solid material. To account for these effects, the Bruggeman correction is applied, which modifies the bulk conductivity to yield an effective electrical conductivity.

Ohm's law in porous electrodes, incorporating the Bruggeman correction, serves as a constitutive relation to equation 2.12 and is expressed as,

$$\mathbf{I}_s = -\kappa_s^{\text{eff}} \nabla \phi_s \quad (2.13)$$

Here,  $\mathbf{I}_s$  is the solid-phase current density,  $\phi_s$  is the solid-phase electric potential, and  $\kappa_s^{\text{eff}}$  is the effective electrical conductivity. The effective conductivity is computed using the Bruggeman relation as:

$$\kappa_s^{\text{eff}} = \nu_s^{(1+\alpha)} \kappa_s \quad (2.14)$$

In the above equation,  $\kappa_s$  represents the intrinsic (bulk) electrical conductivity of the solid material,  $\nu_s$  is the volume fraction of the solid phase, and  $\alpha$  is the Bruggeman exponent. This formulation can also be extended to incorporate anisotropic conductivity.

The conservation of the electrons in the metallic current collector is given in the strong form as,

$$\mathbf{I}_s \cdot \nabla = 0 \quad (2.15)$$

And the movement of the electrons is given by the Ohm's law as,

$$\mathbf{I}_s = -\kappa_s \nabla \phi_s \quad (2.16)$$

Where,  $\kappa_s$  is the electrical conductivity of the metallic current collector. This equation serves as a constitutive law for the equation 2.15.

#### 2.2.2.4 Diffusion of lithium in the microscale

One of the fundamental assumptions of the Doyle-Fuller-Newman (DFN) model is that the active particles within the battery are spherical in shape. This assumption simplifies the mathematical modeling of the electrode's behavior. Additionally, it is assumed that all these particles maintain electrical contact with each other, ensuring efficient electron transport. Importantly, the model assumes there is no inter-particle diffusion, meaning Li-ions do not move between particles but only within each particle.

The ion balance within these spherical particles is governed by Fick's second law of diffusion. This law describes how Li-ions diffuse through the particle over time. In the context of the DFN model, this can be expressed in spherical coordinates, where  $r$  represents the radial coordinate from the center of the particle, and  $c_s$  denotes the Li-ion concentration within the particle. The strong form of Fick's second law in spherical coordinates is given by,

$$\frac{\partial c_s}{\partial t} + \frac{1}{r^2} \frac{\partial}{\partial r} (r^2 j_s) = 0 \quad (2.17)$$

Where  $j_s$  depicts the constitutive relation which can be expressed as,

$$j_s = -D_p(c_s) \frac{\partial c_s}{\partial r} \quad (2.18)$$

Here,  $D_p$  is the diffusion coefficient of Li-ions in the solid phase. The strong form in Equation 2.17 is solved with the constitutive relation in Equation 2.18 using the following boundary conditions,

$$\frac{\partial c_s}{\partial r} = 0 \quad \text{at} \quad r = 0 \quad (2.19)$$

$$j_s = \frac{I_{BV}}{F} \quad \text{at} \quad r = R_p \quad (2.20)$$

At the boundary  $r = R_p$ , each particle interacts with macroscopic fields through the Butler-Volmer lithiation current density. This essentially represents the variation in the Li-ion concentration in the particle is governed by the Butler-Volmer current density ( $I_{BV}$ ).

#### 2.2.2.5 Coupling between the microscale and continuum scale.

As depicted before, the DFN model solves the variables  $\phi_s$ ,  $\phi_e$  and  $c_e$  at the macroscale level and  $c_s$  at microscale level and coupling between these two scales are done via reaction kinetics i.e. through the Butler-Volmer current density  $I_{BV}$  as depicted in equation 2.20.

#### 2.2.2.6 Swelling of the active particles

The intercalation of Li-ions into the active particles of an electrode leads to an increase in the particle volume, a phenomenon commonly known as particle swelling. This expansion of the particles not only influences the overall geometry of the electrode but also significantly alters its mechanical and electrochemical properties. As the active particles swell, the internal stresses within the electrode material change, which can lead to mechanical degradation, reduced structural integrity, or even failure over time. The swelling of the particles also impacts the electrochemical behavior of the electrode, including reaction rates, ion transport, and electrolyte distribution. The changes in particle volume lead to alterations in the porosity of the material, which in turn affects the available pathways for ion migration, potentially limiting ion transport and influencing the efficiency of the electrochemical reactions.

In the modeling framework proposed by Kulathu et al.[16], the swelling behavior is captured by defining a reference configuration for the active material, corresponding to the fully deintercalated state of the negative electrode, where the lithium concentration is zero and fully lithiated state for the positive electrode. This reference state serves as a baseline for the geometry and material properties of the electrode. As the intercalation or deintercalation process progresses, the geometry of the electrode evolves accordingly. The properties of the material are updated in real time to reflect the changes in particle volume, and these updates are mapped from the reference configuration.

Several key geometric and material quantities are defined relative to this reference configuration. These quantities include the solid volume fraction, binder volume fraction, electrolyte volume fraction, and particle volume fractions. The initial state of these quantities in the reference configuration are expressed as follows:

$$\nu_s^0 = \frac{V_p^0}{V_{\text{el}}} \quad (2.21)$$

Where  $\nu_s^0$  is the solid reference volume fraction,  $V_p^0$  represents the reference volume of the active particles, and  $V_{\text{el}}$  is the total volume of the element (or unit cell) in the model. Similarly, for the binder,

$$\nu_b^0 = \frac{V_b^0}{V_{\text{el}}} \quad (2.22)$$

Here,  $\nu_b^0$  is the binder reference volume fraction, and  $V_b^0$  represents the reference volume of the binder material within the electrode. The sum of these volume fractions should add up as follows,

$$\nu_e^0 = 1 - \nu_s^0 - \nu_b^0 \quad (2.23)$$

In the equation 2.23,  $\nu_e^0$  denotes the electrolyte volume fraction, assuming the electrode is fully saturated. The electrolyte volume fraction is calculated by subtracting the solid and binder volume fractions from 1.

The particle volume ratio can be computed by using the reference volume of the active particles and the total volume of the element as,

$$\nu_p^0 = \frac{V_p^0}{\nu_s^0 V_{\text{el}}} \quad (2.24)$$

Here,  $\nu_p^0$  represents the particle volume ratio.

The above equation can be rearranged to relate the reference volume of the active particles to the total volume of the element as,

$$V_p^0 = \nu_p^0 \nu_s^0 V_{\text{el}} \quad (2.25)$$

The particle swelling is tracked relative to the initial (deintercalated) state by introducing a swelling factor  $\theta_p$  for the particle, defined as the ratio of the particle volume at any given time to the initial particle volume:

$$\theta_p = \frac{V_p}{V_p^0} = \Omega \Delta c_{s,p}^{\text{avg}} \quad (2.26)$$

Where,  $\Omega$  is the swelling coefficient and  $c_{s,p}^{\text{avg}}$  is the average Li-ion concentration in the solid particle.

The surface area of the active particles are also affected due to swelling. This is given as,

$$\Delta a_s = \frac{2}{3} a_s \Omega \Delta c_{s,p}^{\text{avg}} \quad (2.27)$$

Now considering the combined effect of the active particle and the binder as one homogenized phase, the total volume change will be

$$J_g = \frac{\theta_p \nu_p + \nu_b^0}{1 + \nu_b^0} \quad (2.28)$$

The average stretch of the particle and the binder mixture often referred to as the "skeleton" can be represented as

$$\bar{\lambda}_r^p = (J_g)^{\frac{1}{3}} \quad (2.29)$$

Now the skeleton stretch can be related to the radial swelling stretch of the particle through power law as

$$\lambda_i = (\bar{\lambda}_r^p)^{s_i} \quad (2.30)$$

Where,  $\lambda_i$  is skeleton stretches, where, i corresponds to the three principal directions i.e. i=1,2 and 3.  $s_i$  is the power law coefficient that can be calibrated for a given particle-binder system.

With the principle radial stretch, the eigen strain due to the swelling can be computed in each principal direction as

$$\varepsilon_i^{\text{eig}} = \log \lambda_i \quad (2.31)$$

The total volumetric strain due to swelling can be computed by adding the eigen strains in directions as

$$\varepsilon_v^{\text{ch}} = \sum_{i=1}^3 \varepsilon_i^{\text{eig}} \quad (2.32)$$

It's important to note that the stiffness properties of the binders are not taken into account when calculating the eigenstrains in the formulations mentioned above. The stiffness of the binder plays a crucial role in determining the effective swelling, as a stiff binder can suppress the swelling of the active particles, which affects the overall effective swelling behavior.

### 2.2.3 Mechanical model

The mechanical response of each electrode in the battery is governed by the momentum balance equation.

$$-\boldsymbol{\sigma} \cdot \nabla = 0 \quad (2.33)$$

To govern the mechanical response, it is essential to establish a constitutive law that captures the relationship between stress and strain. For simplicity, we will assume a linear elastic response, mathematically, this relationship can be expressed as:

$$\boldsymbol{\sigma} = \mathbf{E} : \boldsymbol{\varepsilon}^{\text{el}} \quad (2.34)$$

where  $\boldsymbol{\sigma}$  represents the stress,  $\mathbf{E}$  is the fourth order elastic stiffness tensor, and  $\boldsymbol{\varepsilon}^{\text{el}}$  denotes the elastic strain. The total strain components can be decomposed into the elastic strain caused by the mechanical constraints and the volumetric strain induced by the lithiation induced swelling as

$$\boldsymbol{\varepsilon} = \boldsymbol{\varepsilon}^{\text{el}} + \boldsymbol{\varepsilon}_v^{\text{ch}} \quad (2.35)$$

Now substituting the above equation into the equation 2.34 and rearranging for  $\boldsymbol{\varepsilon}^{\text{el}}$ , the equation can be written as

$$\boldsymbol{\sigma} = \mathbf{E} : (\boldsymbol{\varepsilon} - \boldsymbol{\varepsilon}_v^{\text{ch}}) \quad (2.36)$$

The volumetric strain induced due to lithiation  $\boldsymbol{\varepsilon}_v^{\text{ch}}$  is computed using the equation 2.32.

## 2.2.4 Thermal Model

Although thermal effects are not considered in this study, the governing equations are presented here for the sake of completeness. The formulations provided are based on the work by Kulathu et al. [16].

The temperature distribution within the battery is governed by the transient heat equation, which ensures the conservation of internal thermal energy across the system. This equation accounts for the contributions from both the solid and electrolyte phases. The strong form of the thermal balance equation is expressed as:

$$\rho_s \nu_s \frac{dU_s}{dt} + \rho_e \nu_e \frac{dU_e}{dt} + \rho_e \nu_e \mathbf{V}_e \cdot \nabla U_e = -\nabla \cdot \mathbf{f} + Q \quad (2.37)$$

Where,  $\rho_s$  denotes the mass density in the solid phase,  $\rho_e$  denotes the mass density in the electrolyte phase,  $U_s$  is the internal energy in the solid phase, and  $U_e$  is the internal energy in the electrolyte phase. The term  $Q$  represents a volumetric heat source or sink, accounting for heat generation or absorption within the battery.

The heat flux  $\mathbf{f}$  is defined by Fourier's law and acts as a constitutive law for the equation 2.37, which is given as :

$$\mathbf{f} = -K_{\text{eff}} \nabla T \quad (2.38)$$

Here,  $K_{\text{eff}}$  is the effective thermal conductivity and is calculated using the rule of mixtures as:

$$K_{\text{eff}} = \nu_s K_s + \nu_e K_e \quad (2.39)$$

Where,  $K_s$  is the thermal conductivity in the solid phase and  $K_e$  is the thermal conductivity in the electrolyte phase.

In this formulation, the thermal contribution of the binder phase is neglected. Additionally, it is assumed that both the electrolyte velocity and the temperature gradient within the electrolyte are sufficiently small, allowing the convective term to be considered negligible. The model also assumes local thermal equilibrium, meaning the solid and electrolyte phases are at the same temperature, and thus no inter-phase heat exchange is considered during lithiation or delithiation.

## 2.3 Mechanical material modeling of battery components

Batteries are complex, heterogeneous, and anisotropic materials. The microstructural intricacies of lithium-ion batteries are illustrated in Figure 2.8, highlighting the geometric and material diversity present at the cell level.

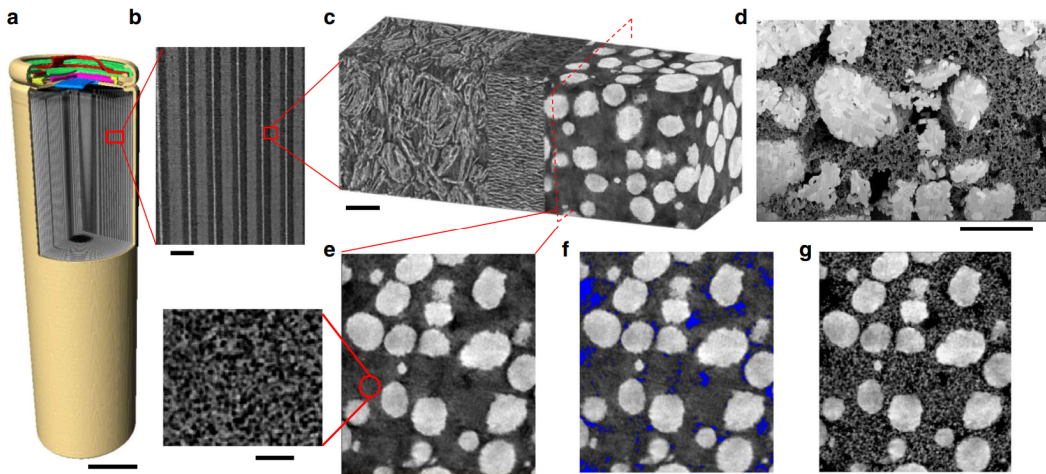


**Figure 2.8:** Microstructural complexities in lithium-ion batteries, reprinted from [17]

Given this inherent complexity, a simple linear elastic constitutive model is insufficient to accurately represent the mechanical response of battery components under operational or accidental loading conditions. Previous studies have shown that when individual battery layers are modeled explicitly, material models such as hyperelastic, mat-modified honeycomb, and crushable foam are well suited for electrodes and separators. For current collectors, linear elastic or elastic-plastic models with isotropic hardening are typically employed. Alternatively, if the battery is represented as a homogenized medium, suitable models include crushable foam, mat-modified honeycomb, orthotropic linear elastic, or elastic piecewise-linear plastic formulations [18].

Explicitly modeling each layer enables the identification of localized failure points and damage mechanisms, but this approach demands significant computational resources and extensive experimental data for material calibration. On the other

hand, using a homogenized representation greatly reduces computational effort, but it may not capture the onset or progression of failure at the layer level. The decision between these two approaches depends largely on the objectives of the study and the level of accuracy required. A promising alternative is to apply multiscale modeling techniques, which strike a balance between computational efficiency and predictive accuracy by bridging detailed microstructural behavior with the macroscopic response.

In this study, a multiscale modeling approach is adopted, incorporating micro-, meso-, and macro-scale levels. The framework is described in more detail in subsection 2.3.3. At the mesoscale level, the individual layers within the battery structure are modeled explicitly. The material models for these layers are selected based on their characteristic behavior; the electrodes and separators are represented using a crushable foam material model, while the current collectors are modeled using an elastic-plastic with isotropic hardening model.

### 2.3.1 Constitutive models

Constitutive models are mathematical descriptions that characterize how materials respond to external loads. Their primary purpose is to define the relationship between stress and strain. Various types of constitutive models exist to represent different material characteristics. For example, elastic models describe materials that return to their original shape after deformation, plastic models capture permanent deformation beyond the elastic limit, and viscoelastic or viscoplastic models account for time-dependent or rate-dependent behaviors.

For materials exhibiting a linear elastic response, the relationship between stress and strain is governed by Hooke's law, which can be expressed as:

$$\boldsymbol{\sigma} = \mathbf{E} : \boldsymbol{\epsilon} \quad (2.40)$$

where  $\boldsymbol{\sigma}$  is the stress tensor,  $\boldsymbol{\epsilon}$  is the strain tensor, and  $\mathbf{E}$  is the fourth-order elasticity tensor. This linear relationship assumes that the material behavior is reversible and that the stress is proportional to strain within the elastic limit.

### 2.3.1.1 Elastic-plastic with isotropic hardening material model

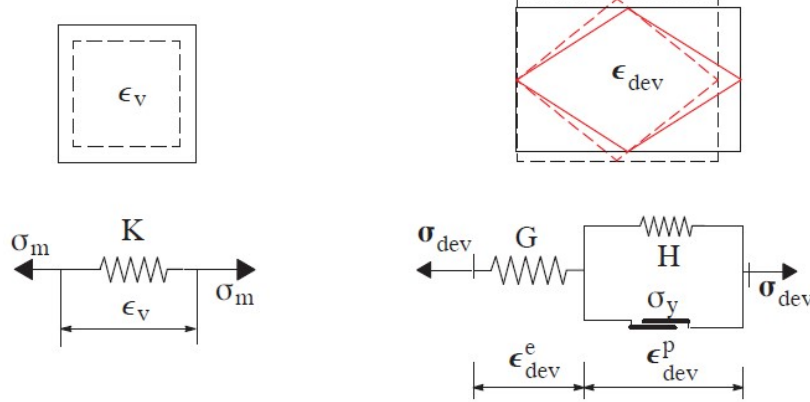


**Figure 2.9:** Prototype model for elastic-hardening-plastic model, reprint from [19].

The current collectors can be modelled with an elastic-plastic material model with isotropic hardening. A prototype model, as depicted in Figure 2.9, can be used to better understand the mean stress-independent metallic materials. When the material is subjected to an external stress  $\sigma_{\text{dev}}$ , it begins to deform. Initially, this deformation is elastic and reversible until the applied stress reaches the initial yield stress. This elastic behavior is represented by a spring with stiffness  $G$  in the prototype model. Once the applied stress exceeds the yield point  $\sigma_y$ , the deformation becomes inelastic and irreversible. This plastic behavior is depicted by the slider in the prototype model. Due to the hardening effect, additional stress is required to further deform the material beyond the yield point. In the prototype model, this is shown as an additional spring with stiffness  $H$  attached in parallel to the slider. The inelastic deformation is considered shear-dominated. When the stress  $\sigma_{\text{dev}}$  is released, unloading occurs, and the energy released corresponds to the stored elastic energy, which is represented by the free energy density. The stored free energy is written as:

$$\psi = \psi_{\text{dev}}[i_{\text{dev}}^e] + \psi_v[\boldsymbol{\epsilon}_v] + \psi_{\text{mic}}[k] \quad (2.41)$$

Where,

$$\psi_v = \frac{1}{2}K\epsilon_v^2, \quad \psi_{\text{dev}} = \frac{1}{2}2G(i_{\text{dev}}^e)^2, \quad \psi_{\text{mic}} = \frac{1}{2}Hk^2$$

Here,  $K$  is the elastic bulk modulus,  $G$  is the elastic shear modulus,  $k$  is the hardening variable,  $H$  is the hardening modulus, and  $i_{\text{dev}}^e$  is the strain invariant defined as:

$$(i_{\text{dev}}^e)^2 = \boldsymbol{\epsilon}_{\text{dev}}^e : \boldsymbol{\epsilon}_{\text{dev}}^e$$

The elastic deviatoric strain is:

$$\boldsymbol{\epsilon}_{\text{dev}}^e = \boldsymbol{\epsilon}_{\text{dev}} - \boldsymbol{\epsilon}_{\text{dev}}^p$$

The volumetric strain is:

$$\varepsilon_v = \mathbf{1} : \boldsymbol{\varepsilon}$$

Differentiating Eq. (2.41) with respect to  $\boldsymbol{\varepsilon}_{\text{dev}}^e$ ,  $\varepsilon_v$ , and  $k$ , we get:

$$\boldsymbol{\sigma}_{\text{dev}} = \frac{\partial \psi_{\text{dev}}}{\partial \boldsymbol{\varepsilon}_{\text{dev}}^e} = 2G \boldsymbol{\varepsilon}_{\text{dev}}^e$$

$$\sigma_m = \frac{\partial \psi_v}{\partial \varepsilon_v} = K \varepsilon_v$$

$$\kappa = \frac{\partial \psi_{\text{mic}}}{\partial k} = -Hk$$

The total stress tensor is:

$$\boldsymbol{\sigma} = \boldsymbol{\sigma}_{\text{dev}} + \sigma_m \mathbf{I} \quad (2.42)$$

Where  $\mathbf{I}$  is the identity tensor.

The dissipation rate  $D$  is:

$$D = \boldsymbol{\sigma} : \dot{\boldsymbol{\varepsilon}} - \dot{\psi} = \boldsymbol{\sigma}_{\text{dev}} : \dot{\boldsymbol{\varepsilon}}_{\text{dev}}^p + \kappa \dot{k} \geq 0 \quad (2.43)$$

The yield function is defined as:

$$\Phi = \sigma_e - (\sigma_y + \kappa) \quad (2.44)$$

Where the effective Von-Mises stress  $\sigma_e$  is:

$$\sigma_e = \sqrt{\frac{3}{2}} |\boldsymbol{\sigma}_{\text{dev}}| = \sqrt{3} \sqrt{J_2}$$

And the second invariant  $J_2$  of the deviatoric stress is:

$$J_2 = \frac{1}{2} |\boldsymbol{\sigma}_{\text{dev}}|^2$$

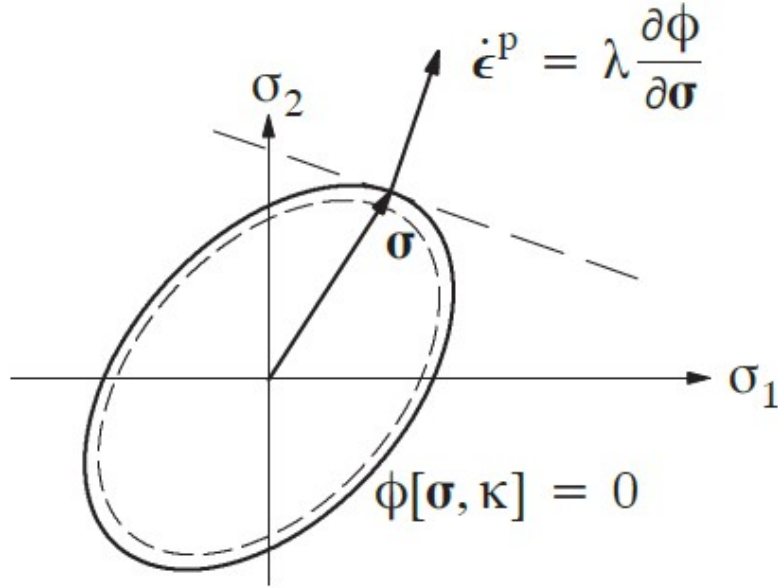


**Figure 2.10:** Flow and hardening rules for hardening plasticity models, reprint from [19].

As shown in the Figure 2.10, the plastic flow direction is normal to the yield surface. The evolution equations for the internal variables are:

$$\dot{\epsilon}_{\text{dev}}^p = \lambda \frac{\partial \Phi}{\partial \sigma_{\text{dev}}} = \lambda \mathbf{f} \quad (2.45)$$

$$\dot{k} = \lambda \frac{\partial \Phi}{\partial \kappa} = -\lambda \quad (2.46)$$

Where  $\lambda$  is the plastic multiplier, subject to the Kuhn-Tucker conditions:

$$\Phi = 0, \quad \lambda \geq 0, \quad \Phi \lambda = 0$$

The gradient of the yield function is:

$$\mathbf{f} = \frac{\partial \Phi}{\partial \sigma_{\text{dev}}} = \frac{3\sigma_{\text{dev}}}{2\sigma_e} \quad (2.47)$$

The constitutive equations are:

$$\dot{\sigma} = \mathbf{E} : \dot{\epsilon} - \lambda \mathbf{E} : \mathbf{f} \quad (2.48)$$

$$\dot{\kappa} = H\lambda \quad (2.49)$$

To determine the plastic multiplier  $\lambda$ , use the consistency condition  $\dot{\Phi} = 0$ :

$$\dot{\Phi} = \frac{\partial \Phi}{\partial \sigma} \cdot \dot{\sigma} + \frac{\partial \Phi}{\partial \kappa} \cdot \dot{\kappa} = 0$$

Substituting the expressions gives:

$$\mathbf{f} : \mathbf{E} : \dot{\boldsymbol{\epsilon}} - (\mathbf{f} : \mathbf{E} : \mathbf{f} + \mathbf{H})\lambda = 0$$

Solving for  $\lambda$ :

$$\lambda = \frac{1}{h} \mathbf{f} : \mathbf{E} : \dot{\boldsymbol{\epsilon}} > 0 \quad (2.50)$$

Where  $h = \mathbf{f} : \mathbf{E} : \mathbf{f} + \mathbf{H} > 0$

### 2.3.1.2 Crushable foam material model

The material response of electrodes and separators can be modeled using a crushable foam material model. There are two types of hardening models available with this approach: volumetric hardening and isotropic hardening. The isotropic hardening model assumes that the material exhibits the same behavior under both tensile and compressive loading conditions. In contrast, the volumetric hardening model considers different responses for tension and compression. For the crushable foam, the tensile loading capacity is small compared to the compressive loading capacity.

For battery electrodes and separators, the tensile strength is lower compared to their compressive strength. Therefore, a volumetric hardening model is appropriate for simulating these materials. The typical stress-strain response of the crushable foam material model is illustrated in Figure 2.11.

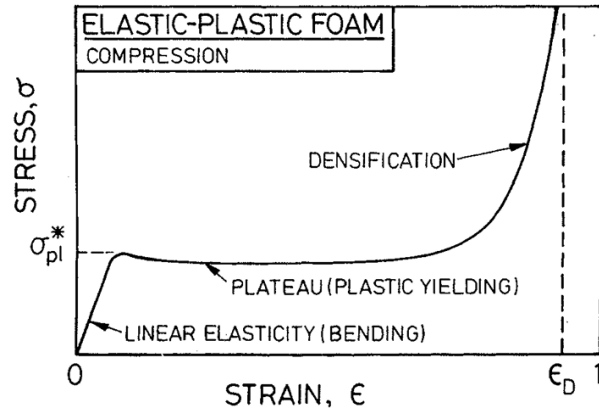


**Figure 2.11:** Typical stress-strain response of crushable foam material model reprint from [20].

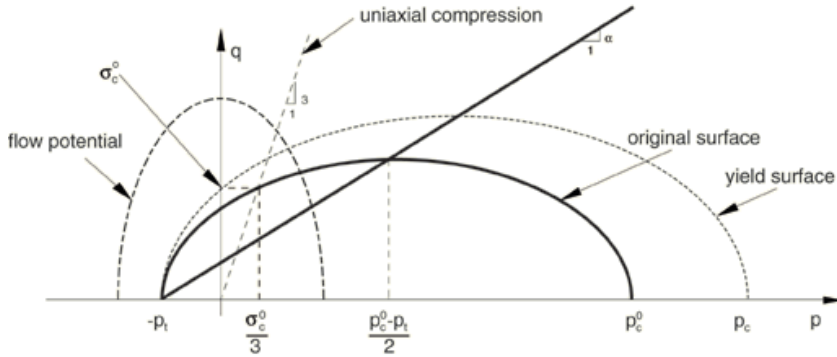


**Figure 2.12:** Flow and hardening rule of crushable foam material model[8].

The behaviour in the elastic regime can be modelled with linear elasticity. Which is given as

$$\boldsymbol{\sigma} = \mathbf{E} : \boldsymbol{\varepsilon}^{\text{el}} \quad (2.51)$$

Where  $\mathbf{E}$  is the fourth order stiffness tensor and  $\boldsymbol{\varepsilon}^{\text{el}}$  is the second order elastic strain tensor.

The movement from the elastic regime to the plastic regime is governed by yield surface. Unlike the metals where the evolution of the yield surface is only governed by the deviatoric stress, for crushable foam material, the mean stress also controls the yield surface. Figure 2.12 depicts the yield surface on a p-q plane where p axis represents the mean stress (hydrostatic pressure) and q represents the deviatoric stress (Von-mises equivalent stress). That is

$$p = -\frac{1}{3}\boldsymbol{\sigma} : \mathbf{I} \quad (2.52)$$

Where  $\boldsymbol{\sigma}$  is the second order stress tensor,  $\mathbf{I}$  is the identity tensor.

$$q = \sqrt{\frac{3}{2}\boldsymbol{\sigma}_{\text{dev}} : \boldsymbol{\sigma}_{\text{dev}}} \quad (2.53)$$

Where  $\boldsymbol{\sigma}_{\text{dev}}$  is the deviatoric stress tensor.

The shape of the yield surface is controlled by a shape factor  $\alpha$ . Which can be computed as

$$\alpha = \frac{3k}{\sqrt{(3k_t + k)(3 - k)}} \quad (2.54)$$

$$k = \frac{\sigma_c^0}{p_c^0} \quad (2.55)$$

$$k_t = \frac{p_t}{p_c^0} \quad (2.56)$$

Where,  $\sigma_c^o$  is the initial yield stress in uniaxial compression,  $p_c^o$  is the initial yield strength in hydrostatic compression and  $p_t$  is the yield strength in hydrostatic tension. The magnitude of the hydrostatic tension strength  $p_t$  remains constant through the plastic deformation, whereas hydrostatic compression strength  $p_c$  evolves due to the compaction induced increase in the density. The yield surface for the volumetric hardening model is given as

$$\phi = \sqrt{q^2 + \alpha^2 \left( p - \frac{p_c - p_t}{2} \right)^2} - \alpha \frac{p_c + p_t}{2} = 0 \quad (2.57)$$

The yield surface is the Mises circle in the deviatoric stress plane.

The hardening rule governs the evolution of the yield surface during plastic deformation. For crushable foam materials, the yield surface evolves with compaction, which results in an increase in density and changes the strength in hydrostatic compression  $p_c$ . The evolution of the yield surface can be described by the following equation, which relates the change in  $p_c$  to the volumetric compacting plastic strain  $\varepsilon_{vol}^{pl}$ :

$$p_c(\varepsilon_{vol}^{pl}) = \frac{\sigma_c(\varepsilon_{axial}^{pl}) \left[ \sigma_c(\varepsilon_{axial}^{pl}) \left( \frac{1}{\alpha^2} + \frac{1}{9} \right) \right]}{p_t + \frac{\sigma_c(\varepsilon_{axial}^{pl})}{3}}$$

In this equation,  $\varepsilon_{axial}^{pl}$  is equal to  $\varepsilon_{vol}^{pl}$  under uniaxial compression, assuming a zero plastic Poisson's ratio. The equation describes how the hydrostatic compression strength  $p_c$  evolves as a function of the axial plastic strain and the compaction-induced changes in density.

The evolution of plastic strain is determined by the flow rule, which is given by:

$$\dot{\varepsilon}^{pl} = \frac{\boldsymbol{\sigma} : \dot{\boldsymbol{\varepsilon}}^{pl}}{G} \frac{\partial G}{\partial \boldsymbol{\sigma}}$$

where  $G$  is the flow potential, which is defined as:

$$G = \sqrt{q^2 + \frac{9}{2} p^2}$$

This expression defines the direction of the plastic flow. The evolution of the flow potential in the p-q plane is shown in Figure 2.12.

### 2.3.2 Material calibration

Material models are mathematical equations that describe the relationship between stress and strain in a material. To implement the material model in simulations, several parameters are required, including Young's modulus, Poisson's ratio, yield stress, and plastic strains. These parameters are typically calibrated using experimental test curves. In other words, the typical stress-strain response from the material model is compared to the stress-strain response obtained from experiments.

Using either a manual approach or optimization methods, the error between the two curves is minimized as much as possible. A typical workflow involved in calibrating a material model is depicted in Figure 2.13.

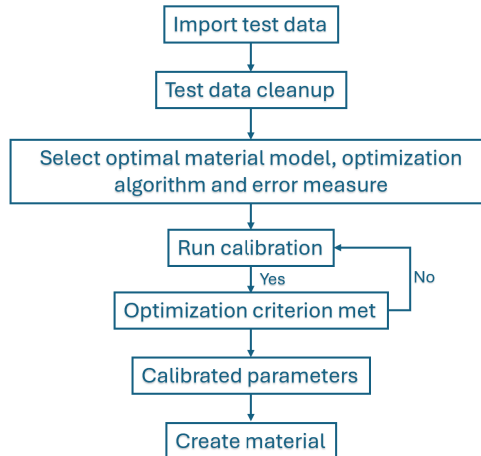


**Figure 2.13:** Flow chart illustrating the typical workflow used in the material calibration.

### 2.3.2.1 Optimization algorithms and error measures

The core idea of the optimization algorithm is to minimize the objective function which is expressed as the difference between the simulated and experimental values. For simplicity considering the objective function as the least square type, the objective function can be mathematically be expresses as,

$$F(\pi) = \min\left(\frac{1}{2} \sum_{i=1}^N [s_i(\pi, u(\pi)) - \bar{s}_i]^2\right) \quad (2.58)$$

Where,  $s_i$  is the simulated response,  $\bar{s}_i$  is the test response,  $N$  is the number of test data sets to be matched,  $u$  is the state variable that contains all the variables needed to describe the state in the test sample and  $\pi$  contains the design parameter that is to be tuned.

If we introduce a parameter domain  $P$  where,

$$P = \pi \in R^m, \pi_{i,min} \leq \pi_i \leq \pi_{i,max}, i = 1, 2, 3..., m$$

Then,  $\pi$  is the solution to the minimization problem

$$\pi = \arg[\min F(\pi^*)] \quad (2.59)$$

If we assume the function  $F$  is smooth, the necessary condition for the solution is

$$\frac{dF}{d\pi_i} \geq 0 \text{ if } \pi_i = \pi_{i,min}$$

$$\frac{dF}{d\pi_i} = 0 \text{ if } \pi_{i,min} < \pi_i < \pi_{i,max}$$

$$\frac{dF}{d\pi_i} \leq 0 \text{ if } \pi_i = \pi_{i,max}$$

If the above conditions are satisfied, then the solution of  $\pi$  corresponds to the local minimum of F.

The optimization methods in general can be broadly classified into the Non-gradient based methods and gradient based methods.

Non-gradient based algorithms find the optimal solution by exploring the solution space using heuristic or probabilistic methods, rather than relying on gradient information. These methods are simple to implement however they suffer from convergence issues. These methods are used when the objective function F is not smooth and is noisy. Gradient based methods uses the derivative of the objective function to find the optimal solution. These methods are effective when the objective function is smooth and continuous.

To measure the difference between the test data and the response curves, the error measures are used. There are many types of error measures that are available and in the broad sense can be classified into the normalized and unnormalized error measures. The selected error measure is used to construct the objective function which will be minimized using the optimization algorithm mentioned above.

The normalized error measures utilize the mean values from the data set. Common examples of these measures include the Coefficient of Determination ( $R^2$ ), Mean Absolute Error, and Root Mean Square Error. In contrast, unnormalized errors rely on individual test values to assess the error, with Relative Square Error being an example of this category. Unnormalized error estimators are useful when the test curve being matched exhibits significant variations in magnitude, and when it is important to achieve a good match for the low-magnitude part of the response.

### 2.3.3 Multiscale modelling and homogenization

The complexity of the battery's microstructure is illustrated in Figure 2.8. In simulations, it is often necessary to consider these microstructures to derive the overall response at the cell level, particularly when deriving the effective material properties of the jelly-roll. However, modeling the microstructural details at cell level can be computationally expensive and cumbersome. To address this, multiscale modeling approaches can be employed. Instead of modeling the entire microstructural details throughout the model, a Representative Volume Element (RVE), a small section of the continuum model is analyzed in detail. The effective response of this RVE, incorporating the microstructure, is then upscaled to the macroscale level using ho-

mogenization techniques.

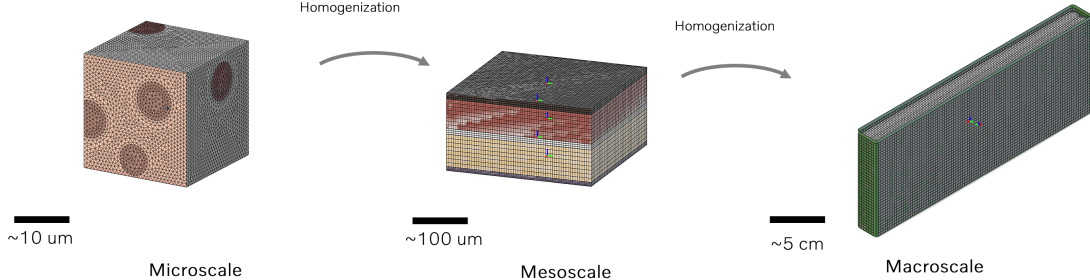


**Figure 2.14:** Multiscale modelling of Li-ion batteries.

Figure 2.14 illustrates a multiscale modeling strategy that involves three different levels. At the microscale level, the microstructural details are explicitly modelled which, including porosity, binders, active particles, and conducting additives. At the mesoscale level, the stack is modelled that includes the positive current collector, the positive electrode active material, the separator, the negative electrode current collector, and the negative electrode active material, all of which are modeled as individual layers. Finally, at the macroscale level, the model is represented as a homogenized entity. The transition between these scales is achieved using homogenization techniques. The lower two scales are modelled via RVE's. Since RVE is a part of the continuum domain, their response should represent the overall response of the continuum domain. To model that response without introducing artificial stresses, the boundary conditions are to be chosen wisely. It has been shown in various literature that when RVE is modelled, to avoid artificial stresses, periodic boundary conditions are often a viable option.

### 2.3.3.1 Periodic boundary conditions

To maintain the periodicity of the RVE, Periodic boundary conditions (PBC) are essential. The main idea in using PBC is to constrain the nodes on the opposite faces to move identically when deformed using kinematic constraints.

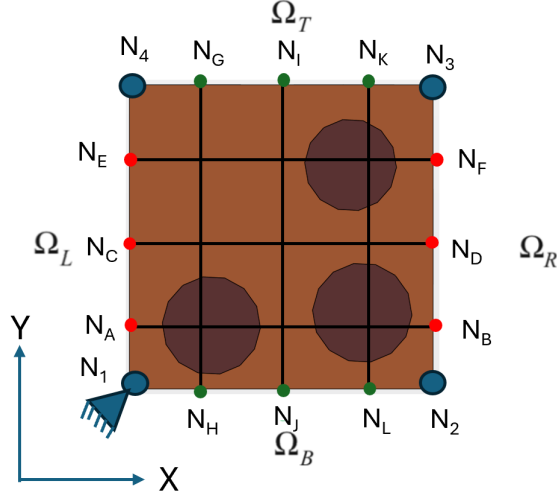


**Figure 2.15:** 2D Representative Volume Element.

Consider the 2D Representative Volume Element (RVE) illustrated in Figure 2.15. The RVE domain, denoted by  $\Omega$ , is divided into four boundaries: left  $\Omega_L$ , right  $\Omega_R$ , top  $\Omega_T$ , and bottom  $\Omega_B$ . Each boundary contains two types of nodes: vertex nodes at the corners and edge nodes along the sides.

For the left boundary  $\Omega_L$ , nodes  $N_1$  and  $N_4$  are vertex nodes, while  $N_A$ ,  $N_C$ , and  $N_E$  are edge nodes. The corresponding nodes on the right boundary  $\Omega_R$  are  $N_2$  and  $N_3$  as vertex nodes, and  $N_B$ ,  $N_D$ , and  $N_F$  as edge nodes. Similar node classifications apply to the top  $\Omega_T$  and bottom  $\Omega_B$  boundaries.

Let  $\bar{\varepsilon}$  be the macroscopic strain applied to the RVE, with  $\bar{\varepsilon}_{xx}$  and  $\bar{\varepsilon}_{yy}$  denoting its components along the principal  $X$  and  $Y$  axes, respectively.

To enforce periodic boundary conditions (PBCs), opposite boundaries are constrained kinematically. For the boundaries  $\Omega_L$  and  $\Omega_R$ , the strain-controlled PBCs in the  $x$ -direction are expressed as follows:

**Vertex nodes:**

$$\mathbf{U}_{N2} - \mathbf{U}_{N1} = \bar{\varepsilon}_{xx} \cdot (X_{N2} - X_{N1}) \quad (2.60)$$

$$\mathbf{U}_{N3} - \mathbf{U}_{N4} = \bar{\varepsilon}_{xx} \cdot (X_{N3} - X_{N4}) \quad (2.61)$$

**Edge nodes:**

$$\mathbf{U}_{NB} - \mathbf{U}_{NA} = \bar{\varepsilon}_{xx} \cdot (X_{NB} - X_{NA}) \quad (2.62)$$

$$\mathbf{U}_{ND} - \mathbf{U}_{NC} = \bar{\varepsilon}_{xx} \cdot (X_{ND} - X_{NC}) \quad (2.63)$$

$$\mathbf{U}_{NF} - \mathbf{U}_{NE} = \bar{\varepsilon}_{xx} \cdot (X_{NF} - X_{NE}) \quad (2.64)$$

Here,  $\mathbf{U}_i$  denotes the displacement vector of node  $i$ , and  $X_i$  is the coordinate of node  $i$  along the  $x$ -axis.

Similar equations are used to apply the constraints in the  $y$ -direction:

**Vertex nodes:**

$$\mathbf{U}_{N2} - \mathbf{U}_{N1} = \bar{\boldsymbol{\varepsilon}}_{yy} \cdot (Y_{N2} - Y_{N1}) \quad (2.65)$$

$$\mathbf{U}_{N3} - \mathbf{U}_{N4} = \bar{\boldsymbol{\varepsilon}}_{yy} \cdot (Y_{N3} - Y_{N4}) \quad (2.66)$$

**Edge nodes:**

$$\mathbf{U}_{NB} - \mathbf{U}_{NA} = \bar{\boldsymbol{\varepsilon}}_{yy} \cdot (Y_{NB} - Y_{NA}) \quad (2.67)$$

$$\mathbf{U}_{ND} - \mathbf{U}_{NC} = \bar{\boldsymbol{\varepsilon}}_{yy} \cdot (Y_{ND} - Y_{NC}) \quad (2.68)$$

$$\mathbf{U}_{NF} - \mathbf{U}_{NE} = \bar{\boldsymbol{\varepsilon}}_{yy} \cdot (Y_{NF} - Y_{NE}) \quad (2.69)$$

Where,  $Y_i$  is the coordinate of node  $i$  along the  $y$ -axis.

Periodic boundary conditions are also enforced on the top  $\Omega_T$  and bottom  $\Omega_B$  boundaries. The constraints along the  $x$ -axis are given by:

$$\mathbf{U}_{NH} - \mathbf{U}_{NG} = \bar{\boldsymbol{\varepsilon}}_{xx} \cdot (X_{NH} - X_{NG}) \quad (2.70)$$

$$\mathbf{U}_{NJ} - \mathbf{U}_{NI} = \bar{\boldsymbol{\varepsilon}}_{xx} \cdot (X_{NJ} - X_{NI}) \quad (2.71)$$

$$\mathbf{U}_{NL} - \mathbf{U}_{NK} = \bar{\boldsymbol{\varepsilon}}_{xx} \cdot (X_{NL} - X_{NK}) \quad (2.72)$$

And the constraints along the  $y$ -axis are:

$$\mathbf{U}_{NH} - \mathbf{U}_{NG} = \bar{\boldsymbol{\varepsilon}}_{yy} \cdot (Y_{NH} - Y_{NG}) \quad (2.73)$$

$$\mathbf{U}_{NJ} - \mathbf{U}_{NI} = \bar{\boldsymbol{\varepsilon}}_{yy} \cdot (Y_{NJ} - Y_{NI}) \quad (2.74)$$

$$\mathbf{U}_{NL} - \mathbf{U}_{NK} = \bar{\boldsymbol{\varepsilon}}_{yy} \cdot (Y_{NL} - Y_{NK}) \quad (2.75)$$

The PBC can also be enforced through a dummy node placed outside the RVE domain. This dummy node can enter the kinematic equations, allowing the external strain to be applied indirectly through this node rather than directly to nodes within the RVE.

For a 3D RVE, PBC enforcement requires creating nodesets for face, edge, and vertex nodes. Constraints must be applied between corresponding nodes on opposite faces, edges, and vertices. Careful attention must be given to edge and vertex constraints to avoid over-constraining the RVE.

# 3

## Methodology

### 3.1 Modeling framework overview

The methodology followed in this work includes a multi-scale approach. Figure 3.1 shows the incorporated methodology framework.

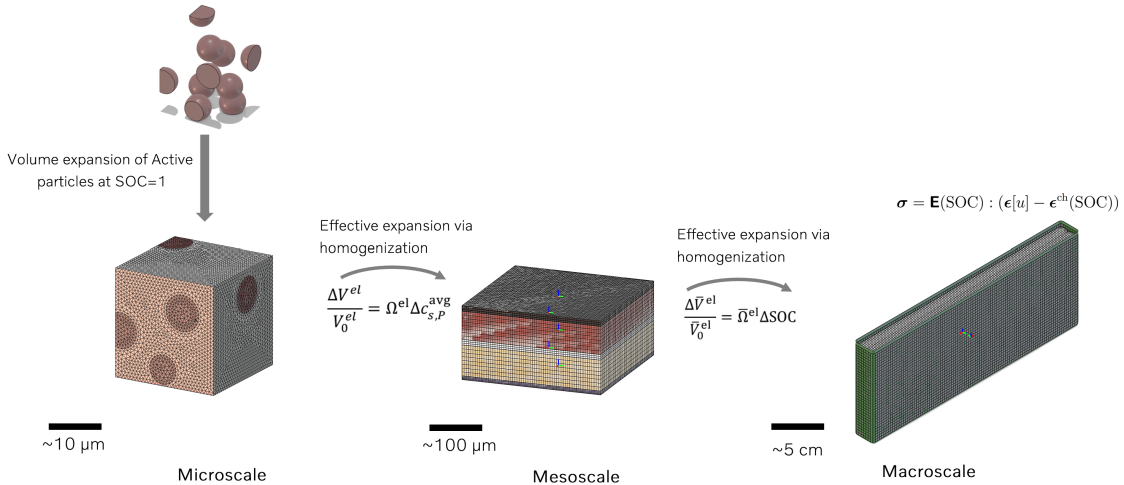


**Figure 3.1:** Incorporated methodology framework.

The core objective of this work is to upscale active particle-level volume changes in order to simulate cell-level expansion. This is achieved through a multiscale modeling approach that begins at the microscale, where the effective swelling coefficient of each electrode is computed. At this scale, the influence of the surrounding matrix on overall swelling behaviour of the electrode is considered.

The computed effective swelling coefficient is then upscaled to the mesoscale. Here, it is incorporated into the material card of the electrodes by tabulating it as a function of the average lithium-ion concentration. To capture the volume changes induced by lithium-ion intercalation, a coupled electrochemical-mechanical simulation is performed at the mesoscale.

The resulting effective volume change is subsequently upscaled to the macroscale using a finite element homogenization technique. This hierarchical approach enables the integration of microstructural effects on the active particle swelling into the continuum-scale model without incurring significant computational cost. A detailed

description of the modeling framework and implementation at each scale is provided in the following sections.

## 3.2 Microscale modeling: particle level response

Figure 2.8 illustrates the complex microstructure of battery electrodes. Due to these inherent complexities, the volumetric expansion of active material inclusions is constrained by the surrounding microstructural components, such as binder, conductive additives, and electrolyte. This constraint leads to the development of internal stresses and strains, and as a result, the effective expansion of the electrode differs from the intrinsic expansion of the active particles. To accurately characterize this behavior, it is essential to determine the effective swelling coefficients of the electrodes while accounting for these microstructural features. However, directly modeling the full microstructure is computationally expensive. To address this, a RVE is employed to capture the essential features of the microstructure in a computationally efficient manner.

### 3.2.1 Geometry and finite element model

The microscale RVEs are constructed using the *Part Design Essentials* app in Dassault 3DEXPERIENCE. Each RVE consists of two distinct phases: a homogenized matrix and multiple inclusions. Two separate RVEs are created—one for the positive electrode and one for the negative electrode. Both model follows a similar modeling approach. The matrix phase is modeled as a homogenized medium consisting of binders, conducting additives and electrolytes. The inclusions represent active material particles and are modeled as spherical particles with uniform diameter to facilitate easier computer aided design (CAD) generation and meshing.

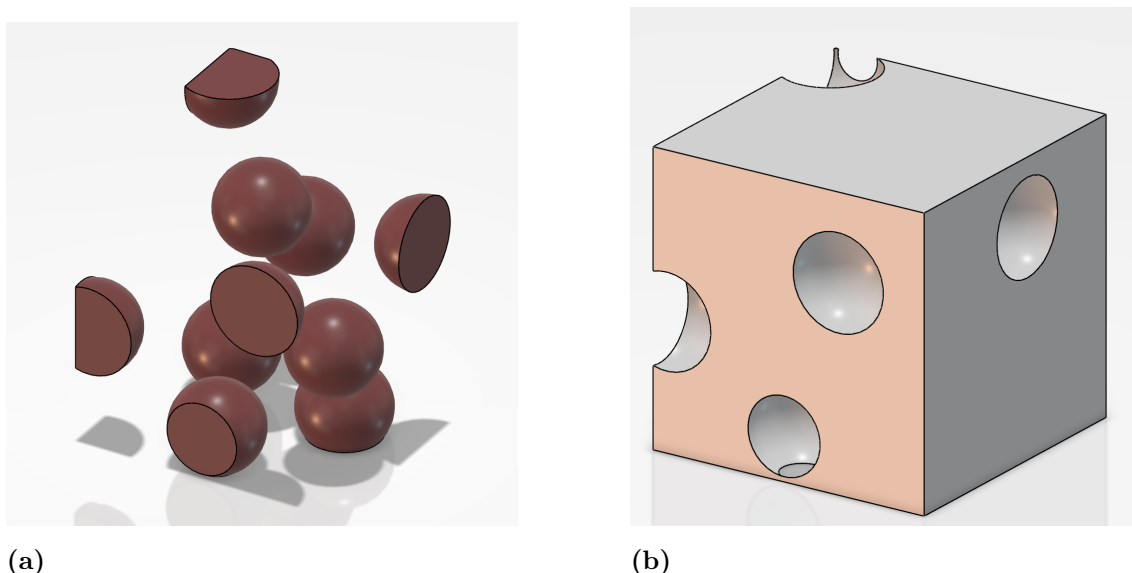


**Figure 3.2:** Figures illustrating the CAD model of (a) inclusions (b) matrix.

Figures 3.2a and 3.2b illustrate the CAD representations of the generated inclusions and the matrix, respectively. It is important to note that, to achieve higher volume fractions of inclusions, spherical particles of varying diameters must be introduced rather than using uniform sizes. This approach enables more efficient packing and better represents the actual microstructural heterogeneity.

The achieved volume fraction of the inclusions,  $\nu_p$ , can be computed using the following formula:

$$\nu_p = \frac{N \times V_s}{V_c} \quad (3.1)$$

Where,  $\nu_p$  is the volume fraction of the inclusions, N is the number of inclusions,  $V_s$  is the volume of the inclusions and  $V_c$  is the volume of the composite.

The spatial distribution of the inclusions within the RVE is generated using the Random Sequential Addition (RSA) algorithm. This algorithm allows for the random placement of spherical particles within the matrix domain while ensuring that they do not overlap. The RSA method iteratively inserts one particle at a time into the RVE domain by randomly selecting coordinates and checking for overlaps with previously placed particles. If an overlap is detected, the insertion is rejected and a new random position is tried. This process continues until the desired number of inclusions is successfully placed, resulting in a non-overlapping, randomized microstructure that closely mimics the stochastic nature of particle distributions in real electrode materials.

Both the inclusions and the matrix are discretized using C3D4 tetrahedral elements. The meshing process is carried out sequentially to ensure compatibility at the interface between the two phases. First, the matrix is meshed independently. Then, the inclusions are meshed using the matrix mesh as a reference, allowing for the generation of condensed nodes at the matrix–inclusion interface. This approach ensures node-to-node connectivity between the two phases, effectively eliminating the need to define an explicit contact modelling. Figure 3.3 illustrates the resulting finite element mesh of the microscale RVE model.

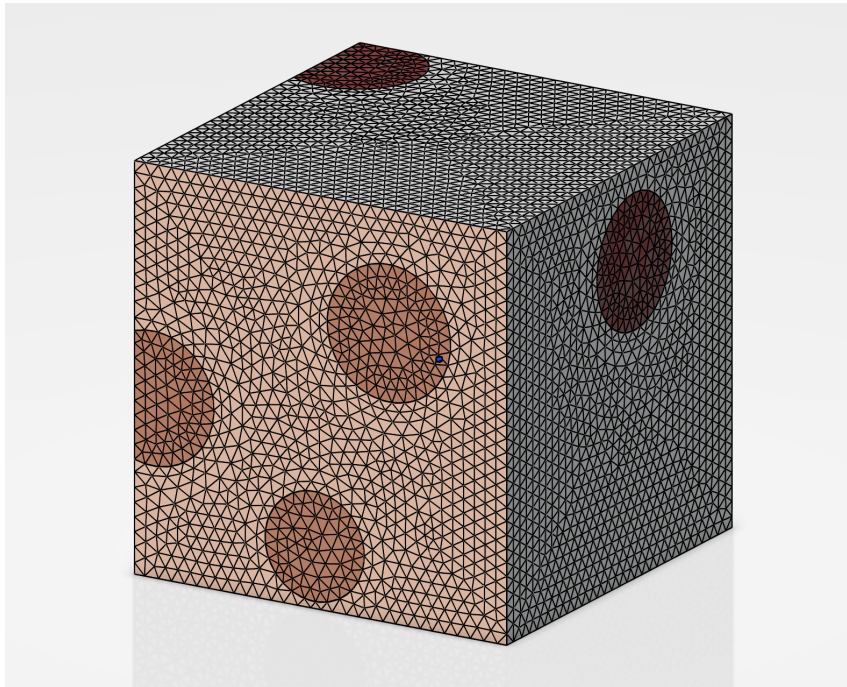


**Figure 3.3:** Finite element model of the microscale RVE.

### 3.2.2 Constitutive model

Two types of constitutive models are considered at the microscale. Initially, a linear elastic material model is employed for simplicity. This formulation is then extended to incorporate a nonlinear material model, allowing for a more realistic representation of the mechanical behavior.

#### 3.2.2.1 Linear material model

A linear elastic material model is chosen for both the matrix and inclusions of positive and negative electrodes. The matrix material is porous in nature and is relatively soft compared to that of the inclusions. Although a linear elastic material does not capture the response of the matrix, to simplify the study, the linear elastic material model is chosen. In the negative electrode, graphite is chosen as the active material, thus the inclusions are modelled using graphite material properties. Table 3.1 summarizes the elastic properties of the graphite.

Property	Magnitude
Young's modulus	32 GPA
Poisson's ratio	0.32

**Table 3.1:** Graphite material properties from [9].

For the positive electrode, the inclusions are modeled using  $\text{LiMn}_2\text{O}_4$ , a commonly used positive electrode active material. The material properties of  $\text{LiMn}_2\text{O}_4$ , used to define the linear elastic behavior of the inclusions, are summarized in Table 3.2.

Property	Magnitude
Young's modulus	190 GPa
Poisson's ratio	0.22

**Table 3.2:** LiMn<sub>2</sub>O<sub>4</sub> material properties from [9].

For both positive and negative electrodes, the same matrix material properties are assumed. Table 3.3 shows the assumed linear elastic properties for the matrix.

Parameters	Magnitude
Young's modulus (GPa)	0.72
Poisson's ratio	0.01

**Table 3.3:** Assumed elastic properties of the matrix.

### 3.2.2.2 Non-linear material model

In both the negative and positive electrodes, the active material particles are represented as linear elastic inclusions, using the material properties listed in Tables 3.1 and 3.2, respectively. These inclusions capture the relatively stiff mechanical behavior of the active materials. In contrast, the surrounding matrix is modeled using a crushable foam material model. This material model captures the nonlinear and highly compressible behavior of the matrix.

The key material properties assigned to the matrix phase in the simulations are presented in Table 3.4. Additionally, the hardening behavior, which dictates the material's plastic response under compressive loading, is depicted in Figure 3.4.

Property	Magnitude
Young's modulus	0.72 GPa
Poisson's ratio	0.01
Compression stress ratio	2.99
Yield stress ratio	0.1

**Table 3.4:** Assumed matrix material properties.

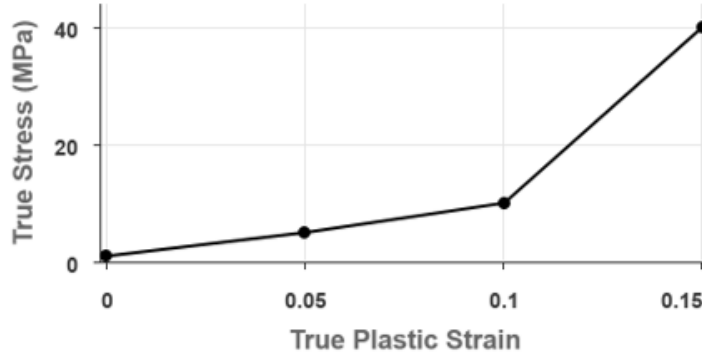


**Figure 3.4:** Matrix hardening curve.

### 3.2.3 Boundary condition

Since the RVE is part of a continuum model, its response must accurately reflect the macroscopic behavior without introducing artificial stresses. PBCs are the most commonly used method to achieve this.

#### Implementation in *3DEXPERIENCE*:

In *3DEXPERIENCE*, PBCs can be implemented in two steps.

In the first step, a Representative Volume Element abstraction shape must be created using the *Structural Model Creation* app. This process involves selecting opposing faces of the RVE, defining the master and slave faces, and specifying the overall RVE volume. This abstraction allows for the enforcement of surface-based periodic boundary constraints.

In the second step, strain-controlled PBCs are applied using the Far Field Condition feature within the Boundary Condition Toolbox in the *Mechanical Scenario Creation* app. In this step, uniform strains are specified along the Cartesian coordinate directions to simulate the macroscopic deformation modes. To prevent rigid body motion when the macroscopic strain is applied, a node intersecting the three master faces must be pinned.

### 3.2.4 Load cases

The primary objective at the microscale level is to characterize the effective swelling coefficient of the electrode. In other words, the aim is to capture the effective swelling and shrinking behavior of the electrode resulting from the volumetric changes of the active material particles. To achieve this, two load cases are analyzed. The first load case is used to characterize the homogenized mechanical response of the microscale RVE. The second load case focuses on extracting the effective response of the RVE due to the swelling of the inclusions. Using these load cases, mathematical formulations for characterizing the effective swelling coefficients are developed and

analyzed for both linear and non-linear material response scenarios. More details on the Load cases and strategy for computing the effective swelling coefficient is presented in the following Subsections.

#### 3.2.4.1 Load case 1: To characterize a homogenized response of the RVE

To characterize a effective response of both positive and negative electrode RVE, a strain controlled PBC is applied with a macroscopic strain of 10% along the six loading directions i.e three principal and three shear directions as shown in the Figure 3.5 and 3.6. Where, the black arrows depicts the applied macroscopic strain direction. It should be noted that for the sake of brevity, only the tensile loading cases are represented in the Figures. The obtained response from the virtual testings are utilized to calibrate the homogenized material model.

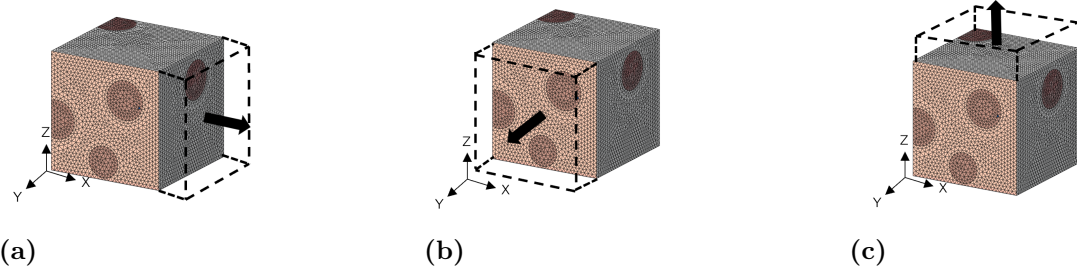


**Figure 3.5:** Figures illustrating the applied strain controlled PBC to characterize the response in a) X principal direction, b) Y principal direction, c) Z principal direction.

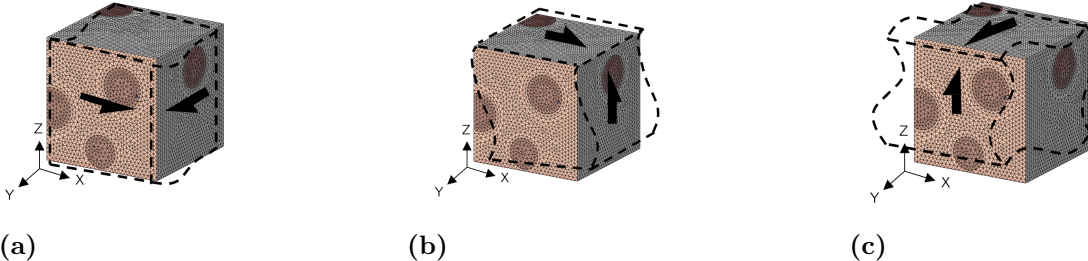


**Figure 3.6:** Figures illustrating the applied strain controlled PBC to characterize the response in a) XY shear direction, b) XZ shear direction, c) YZ shear direction.

#### 3.2.4.2 Load case 2: To characterize effective response of the RVE due to the swelling of the inclusion

In the second load case, a battery charging scenario is assumed, wherein, lithium ions are extracted from the positive electrode and intercalated into the negative electrode. This intercalation and deintercalation process induces volumetric changes in the active material inclusions. However, since these inclusions are embedded within a surrounding matrix, their free expansion or contraction is mechanically constrained. This constraint leads to the development of internal stresses within the

RVE. To capture the effective mechanical response of the RVE due to the volumetric changes of the inclusions, periodic boundary conditions are applied without imposing any macroscopic strain. Instead, a strain field corresponding to the swelling and shrinking of the inclusions arising from lithiation and delithiation is introduced. The resulting effective response of the RVE, assuming a linear elastic material behavior can also be represented by Equation

$$\bar{\sigma}_o = \bar{\mathbf{E}} : (\bar{\boldsymbol{\varepsilon}} - \bar{\boldsymbol{\varepsilon}}_v^{ch}) \quad (3.2)$$

Where,  $\bar{\boldsymbol{\varepsilon}}_v^{ch}$  represent the effective volumetric strain in the inclusions due to lithiation and delithiation,  $\bar{\boldsymbol{\varepsilon}}$  represents the response due to the imposed macroscopic strain,  $\bar{\mathbf{E}}$  represents the effective stiffness of the microscale RVE and  $\bar{\sigma}_o$  represents the effective stress response due to the mechanical constraints and the volumetric change due to lithiation and delithiation.

Since, no macroscopic strain is applied in this case i.e.  $\bar{\boldsymbol{\varepsilon}} = 0$ , the equation simplifies to:

$$\bar{\sigma}_o = \bar{\mathbf{E}} : (-\bar{\boldsymbol{\varepsilon}}_v^{ch}) \quad (3.3)$$

#### Implementation strategy used in *3DEXPERIENCE*:

Since *3DEXPERIENCE* does not allow direct implementation of strain fields as loads, an alternative approach is adopted. In this method, the swelling coefficient of the inclusions is determined using the imposed volumetric strain and the change in lithium-ion concentration within the inclusions, as given by:

$$\Omega = \frac{\bar{\boldsymbol{\varepsilon}}_{v_i}^{ch}}{\Delta c_{s,p}^{avg}} \quad (3.4)$$

where  $\bar{\boldsymbol{\varepsilon}}_{v_i}^{ch}$  is the imposed volumetric strain in the inclusions without considering the effect of the surrounding matrix,  $\Omega$  is the swelling coefficient of the inclusions, and  $\Delta c_{s,p}^{avg}$  is the change in the average lithium-ion concentration in the solid particles.

It is important to note that the swelling coefficient,  $\Omega$ , as defined in Equation 3.4, serves as a deformation scale factor for the inclusions, capturing the stress-free volumetric changes induced by variations in lithium-ion concentration. However, this formulation does not consider the constraints exerted by the surrounding matrix on the swelling of the inclusions.

Using the formulation shown in the equation 3.4, for the negative electrode, using the initial lithium ion concentration of  $0 \text{ mol}/m^3$  and the maximum lithium ion concentration of  $31,920 \text{ mol}/m^3$  from [16], the swelling coefficient  $\Omega$  can be calculated by considering a 10% volumetric expansion of the graphite, which is reported in [9]. This results in the swelling coefficient of  $3.1 \times 10^{-6} \text{ m}^3/\text{mol}$ . In the *3DEXPERIENCE* platform, this coefficient is implemented by defining it as the thermal

expansion coefficient in the material card of the inclusions, using the *Material Definition* app. The lithium-ion concentration profile over time is specified as a tabulated dataset and applied through the Predefined field to drive the swelling behavior.

A similar approach is taken for the positive electrode inclusions. The initial lithium ion concentration is taken as  $0 \text{ mol}/\text{m}^3$  and the maximum lithium ion concentration is taken as  $48,580 \text{ mol}/\text{m}^3$  from [16]. It has to be noted that for the charging cycle, the positive electrode starts with the maximum lithium ions and due to the delithiation, loses the ions and reaches a minimum value at the end of the charging cycle. In this case, the initial lithium ion concentration is assumed to be the minimum value. A volume contraction of 6.8% as reported in [9] for  $\text{LiMn}_2\text{O}_4$  is adopted. The volume change of 6.8% corresponds to the swelling coefficient of  $1.4 \times 10^{-6} \text{ m}^3/\text{mol}$ .

### 3.3 Up-scaling to mesoscale: Effective swelling coefficient determination

#### 3.3.0.1 Case 1: Linear elastic constitutive model

With the boundary conditions and the first load case, the effective material response of the RVE to an applied macroscopic strain can be computed. Under the assumption of linear elasticity, the effective response in strong form is given by:

$$\bar{\sigma} = \bar{\mathbf{E}} : \bar{\epsilon} \quad (3.5)$$

Where,  $\bar{\sigma}$  is the overall stress tensor resulting from the applied macroscopic strain  $\bar{\epsilon}$ , and  $\bar{\mathbf{E}}$  is the effective stiffness tensor of the RVE, capturing contributions from both the matrix and inclusions.

This formulation can be extended to incorporate the swelling of the inclusions due to lithiation. The swelling induces a volumetric strain proportional to the change in lithium concentration, thus the relation can be expressed as:

$$\bar{\sigma} = \bar{\mathbf{E}} : (\bar{\epsilon} - \Omega^{\text{el}} \Delta c_{s,p}^{\text{avg}}) \quad (3.6)$$

Here,  $\Omega^{\text{el}}$  is the effective swelling coefficient of the RVE due to the swelling of the inclusions and  $\Delta c_{s,p}^{\text{avg}}$  is the average change in Li-ion concentration within the inclusions.

Next, considering the second load case, where the effective response of the RVE due to swelling of the inclusions is computed without having any macroscopic strains ( $\bar{\epsilon} = \mathbf{0}$ ). This in the strong form can be represented as:

$$\bar{\sigma} = \bar{\sigma}_o (\Delta c_{s,p}^{\text{avg}}) \quad (3.7)$$

Where,  $\bar{\sigma}_o (\Delta c_{s,p}^{\text{avg}})$  represent the overall stress response due to change in the average Li-ion concentration  $\Delta c_{s,p}^{\text{avg}}$ .

By combining Eqs. (3.6) and (3.7), and assuming no applied macroscopic strain, the effective swelling coefficient can be expressed at a fully lithiated or delithiated state, where the lithium-ion concentration change is normalized ( $\Delta c_{s,p}^{\text{avg}} = 1$ ) using the respective maximum and minimum values as:

$$\Omega^{\text{el}} = -\bar{\mathbf{E}}^{-1} : \bar{\boldsymbol{\sigma}}_o(1) \quad (3.8)$$

It should be noted that in the above equation ( $\Delta c_{s,p}^{\text{avg}} = 1$ ) corresponds to both the fully lithiated and fully delithiated states, as the concentration change has been normalized with respect to the maximum and minimum values for each case, respectively.

The solution to equation 3.8 represent the effective swelling coefficient of the electrodes for a charging scenario. This method of computing effective swelling coefficient considers the effect of stiffness of the matrix material in deriving the overall volume change of the inclusions and thus the overall volume change of the electrode.

### 3.3.0.2 Case 2: Non-linear constitutive model

Similar to the linear elastic case, the first loading condition is used to characterize the effective mechanical response of the RVE. However, in this case, the stress-strain relationship is nonlinear. The effective response of the RVE to an applied macroscopic strain can be expressed as:

$$\bar{\boldsymbol{\sigma}} = \hat{\boldsymbol{\sigma}}(\bar{\boldsymbol{\varepsilon}}) \quad (3.9)$$

Here,  $\hat{\boldsymbol{\sigma}}(\bar{\boldsymbol{\varepsilon}})$  denotes the overall stress as a nonlinear function of the applied macroscopic strain.

To account for the swelling of inclusions due to changes in the average lithium-ion concentration, the formulation is extended accordingly as:

$$\bar{\boldsymbol{\sigma}} = \hat{\boldsymbol{\sigma}}\left(\bar{\boldsymbol{\varepsilon}} - \Omega^{\text{el}}\Delta c_{s,p}^{\text{avg}}\right) \quad (3.10)$$

In the absence of any externally applied macroscopic strain, this equation simplifies to:

$$\bar{\boldsymbol{\sigma}} = \hat{\boldsymbol{\sigma}}\left(-\Omega^{\text{el}}\Delta c_{s,p}^{\text{avg}}\right) \quad (3.11)$$

This implies that if the macroscopic strain were equal in magnitude to  $\Omega^{\text{el}}\Delta c_{s,p}^{\text{avg}}$ , the resulting stress would correspond to the effective response of the RVE due to swelling alone.

In Load Case 2, the actual mechanical response of the RVE resulting from the swelling of the inclusions is directly evaluated and is expressed in its strong form as:

$$\bar{\boldsymbol{\sigma}} = \hat{\boldsymbol{\sigma}}_o\left(\Delta c_{s,p}^{\text{avg}}\right) \quad (3.12)$$

Where,  $\hat{\sigma}_o(\Delta c_{s,p}^{\text{avg}})$  represent the overall stress response due to change in the average Li-ion concentration  $\Delta c_{s,p}^{\text{avg}}$ .

By comparing this actual response with the effective response predicted by equation (3.11), the value of the effective swelling coefficient  $\Omega^{\text{el}}$  can be iteratively adjusted until the two responses closely match. This modeling strategy allows us to bypass the mathematical complexities associated with calculating the effective swelling coefficient for the nonlinear material response directly.

### 3.4 Mesoscale modeling: Electrode-level response

The mesoscale model represents a section of the jellyroll stack and is formulated as a RVE. At this scale, both the positive and negative electrodes are explicitly included, thus a coupled electrochemical-mechanical simulation is setup to capture the lithiation induced swelling and delithiation induced shrinkage of the electrodes. The extent of electrode expansion and contraction is characterized using the effective swelling coefficients computed from the microscale model. The primary objective at this scale is to compute the effective volume change of the stack resulting from the lithiation and delithiation processes.

#### 3.4.1 Geometry and finite element model setup

The mesoscale model of the RVE consists of five distinct layers arranged in sequence: a negative current collector, a negative active material, a separator, a positive active material, and a positive current collector. These layers were designed using the *Part Design Essentials* app in Dassault 3DEXPERIENCE. In the model, the negative current collector is positioned at the bottom, while the positive current collector sits at the top. To determine the thickness of each layer, electrode and separator samples were measured using a micrometer. Because the electrodes consist of a metal foil substrate with an active material coating, it was challenging to measure the thickness of the active material alone. To address this, the thickness of the metal foil was subtracted from the total electrode thickness, yielding the thickness of the active layer. The measured values for each component are summarized in Table 3.5.

Component	Thickness ( $\mu\text{m}$ )
Negative current collector	11
Negative active material	88
Separator	16
Positive active material	80
Positive current collector	16

**Table 3.5:** Thickness of the layers in the mesoscale RVE stack.

The in-plane dimensions were set to 0.5 mm  $\times$  0.5 mm. The resulting CAD model, constructed with these specifications, is illustrated in Figure 3.7.

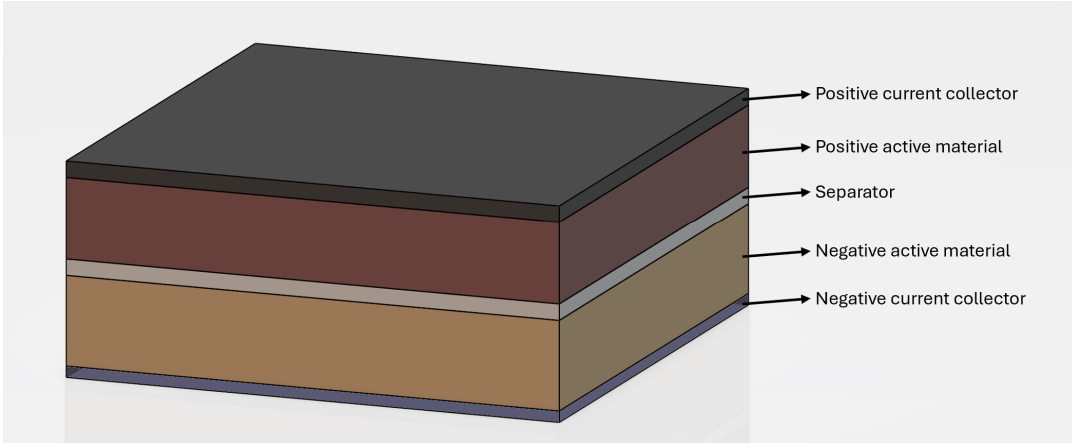


**Figure 3.7:** CAD model of mesoscale RVE.

The generated CAD model was subsequently meshed using QEC3D8 linear brick elements. The meshing was done using sweep mesh technique. The negative current collector is meshed first. From there, the mesh was progressively propagated through each successive layer and finally to the positive current collector. This propagation technique follows a condensed node approach, ensuring that the nodes at the interface of adjacent layers are shared. By enforcing nodal continuity across interfaces, the need to explicitly model contact interactions between layers is eliminated. According to guidelines outlined in the Dassault *3DEXPERIENCE* manual [8], a minimum of three elements are required along the thickness of each layer to adequately capture out-of-plane stress and strain variations. For the in-plane directions, the number of elements was determined based on the results of a mesh convergence study. Figure 3.8 illustrates the finite element model, which was generated using a refined mesh size of 0.008 mm.

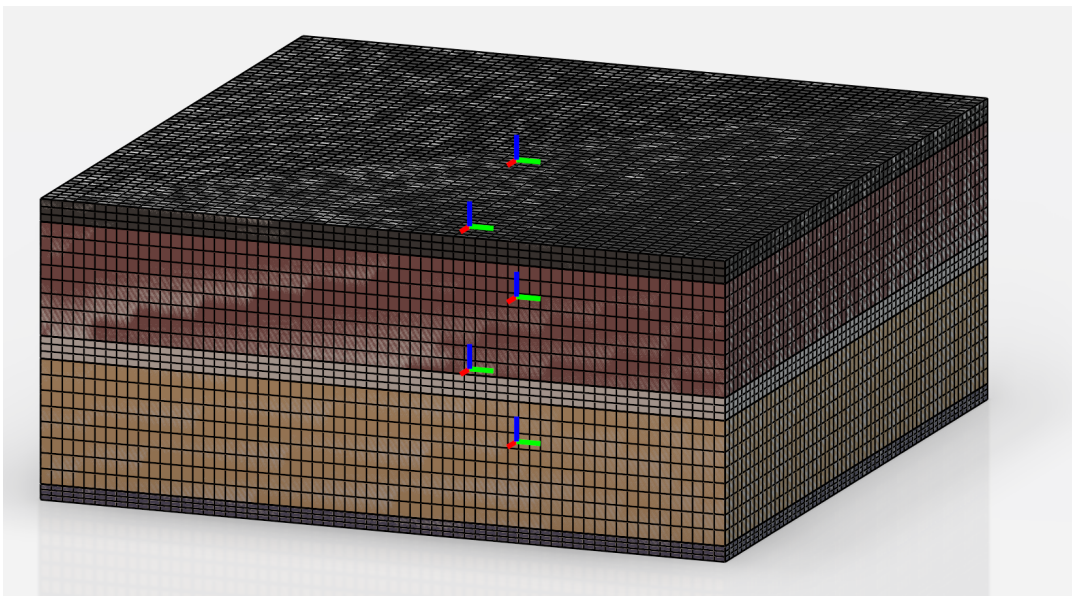


**Figure 3.8:** Finite element model of mesoscale RVE.

### 3.4.2 Constitutive model

#### 3.4.2.1 Material characterization: Experimental test setup

To accurately characterize the mechanical response of each component layer of the jelly roll, a series of uniaxial tensile and compression experiments were conducted. As mentioned, the electrodes consist of active material coatings applied onto the thin metallic current collectors. The response of these electrodes reflects both constituents. To isolate the mechanical response of the active material, uniaxial tests were performed on the full electrode, followed by separate testing of the bare current collector foils. The stress strain data from the current collector was subtracted from the complete electrode response, yielding the effective mechanical behavior of the active material layer. For these tests, the electrodes were assumed to behave as transversely isotropic materials, meaning their mechanical properties are consistent in the in-plane directions. As such, uniaxial tests conducted in any of their in-plane direction is sufficient for characterization. The current collectors, composed of metallic foils, were also treated as isotropic materials and tested in a single in-plane direction. The separator required a slightly different approach due to its anisotropic nature. The uniaxial tensile tests were performed in multiple in-plane directions to fully capture its directional mechanical properties.

The preparation of specimens for uniaxial testing must be carried out with great care to avoid introducing edge effects, cracks, or any form of damage that could compromise the accuracy of the results. For tensile testing, the electrodes, separators, and current collectors are cut into strip-shaped specimens with a width of 2 mm and the height of 15 mm, as illustrated in Figure 3.9a. For compression testing, the specimens are prepared in a circular shape with the diameter 2.5 mm as shown in Figure 3.9b. The diameter of these circular specimens must be carefully selected to ensure proper alignment and to prevent slippage between layers during testing.

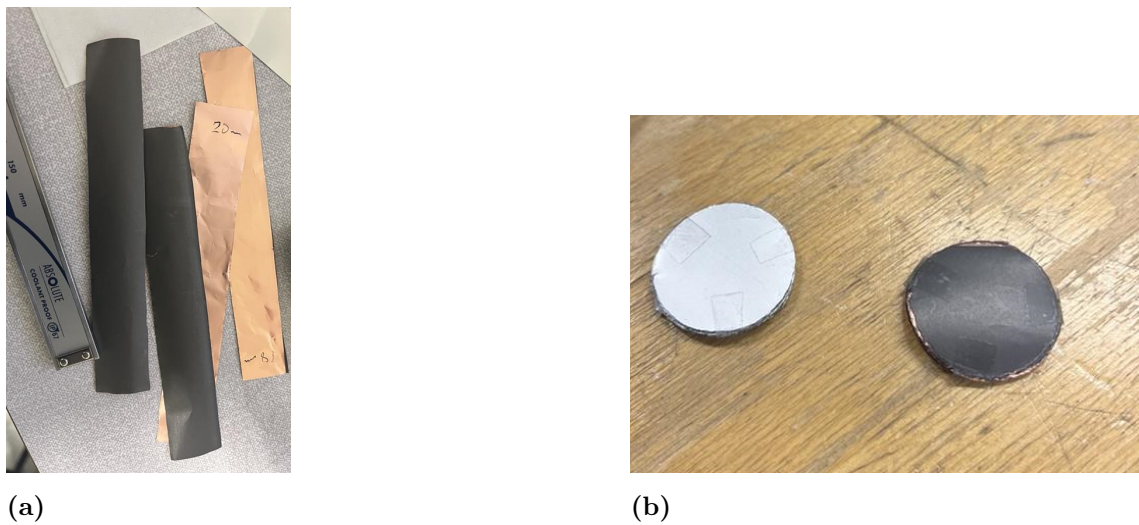


**Figure 3.9:** Figure showing the prepared test specimens (a) for tensile test and (b) for compression test.

The test setup for the tensile experiment is shown in Figure 3.10a, where a Zwick Roell Z2.5 tensile testing machine was used to perform the uniaxial tensile tests. A displacement controlled loading method was adopted due to the thin and delicate nature of the specimens. Loading rates of 20 mm/min and 5 mm/min were applied. The setup for the compression test is shown in Figure 3.10b. This experiment was carried out using an MTS universal testing machine, also employing a displacement controlled approach. The loading rate of 2 mm/min was used to characterize the response.

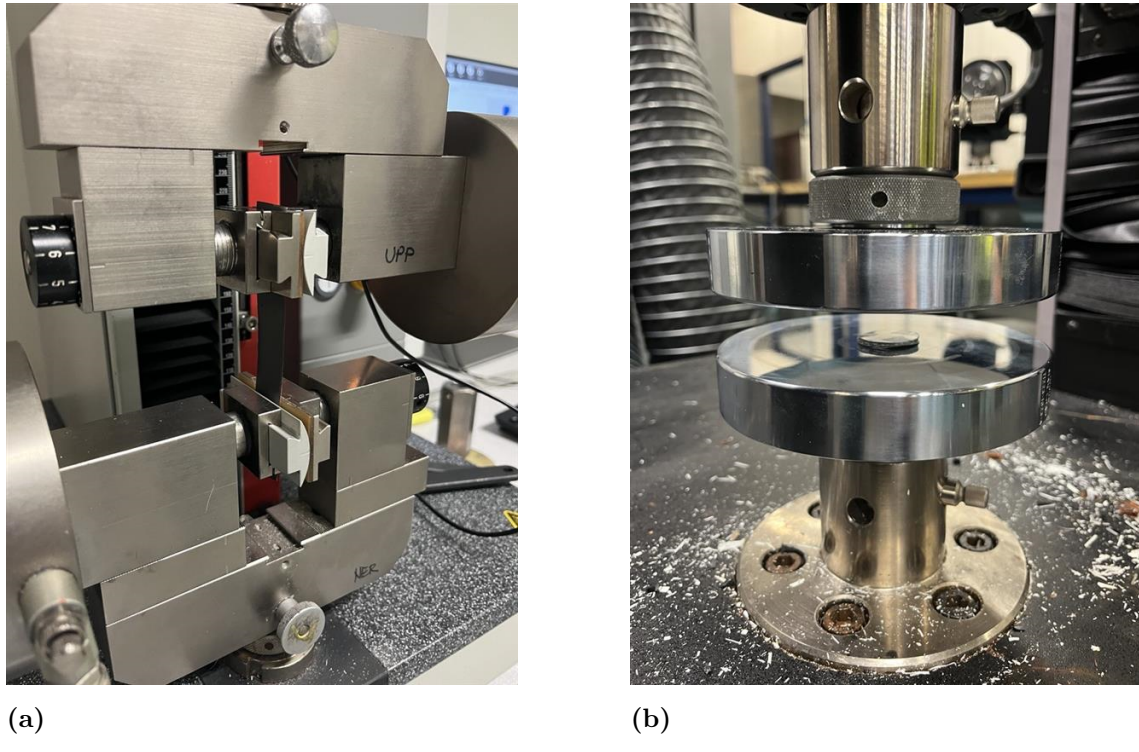


**Figure 3.10:** Figure showing the test setup (a) for tensile test and (b) for compression test.

Due to safety restrictions, the positive electrodes could not be tested under either tensile or compressive loading. Additionally, due to time constraints, the separator was not tested in compression. As a result, stress-strain curves from literature were adopted for use in the simulations conducted in this study. The test curves used for the material calibration are taken from the literature [21].

### 3.4.2.2 Material calibration

The stress strain curves from the literature [21] were used to calibrate the material models for each layer. Specifically, the stress strain curves generated from the tests served as input for fitting and adjusting the parameters of the selected constitutive models, ensuring that the numerical simulations accurately reflect the observed mechanical behavior.

**Material calibration procedure followed in *3DEXPERIENCE*:**

Material calibration was carried out using the *Material Calibration* app available in Dassault *3DEXPERIENCE*. The calibration was performed in numerical mode, which internally applies Newton iterations to minimize residuals and align the simulated material response with the experimental data. This iterative approach ensures that the material parameters are optimized to reproduce the observed mechanical behavior as accurately as possible. For both the positive and negative current collectors, an elasto-plastic material model was adopted to capture their metallic behavior under loading. In contrast, the positive and negative active materials, along with the separator, were modeled using a crushable foam material model to account for their porous and nonlinear mechanical characteristics. In total, two distinct material models were employed to represent the components of the jelly roll.

**Material calibration: Elasto-plastic material model**

In this material model, the calibration setup consists of two parts: the elastic region and the plastic region. The elastic behavior is chosen as isotropic. Since only uniaxial test data is available, Poisson's ratio could not be calibrated directly. Therefore, standard Poisson's ratio values for aluminium and copper were used for the positive and negative current collectors, respectively. The Young's modulus was calculated from the slope of the elastic portion of the experimental stress strain curve and was provided as an initial input for further optimization.

For the plastic region, the plasticity type was defined as isotropic tabular, which allows direct input of yield stress and plastic strain data points from the experiment. The number of stress strain pairs was set equal to the number of available data points beyond the yield point in the test curve. The linear extrapolation option was enabled, which estimates the material response beyond the defined range based on the slope at the last data point. All plastic strain and stress data points were included in the further optimization process.

The calibration app offers both gradient and non gradient based optimization algorithms. In this study, a gradient based Broyden–Fletcher–Goldfarb–Shanno (BFGS) algorithm was selected to minimize the error between the experimental and simulated response curves. The cost function used for calibration was the relative square error, which evaluates the difference between the curves at each data point. The solver settings were kept at their default configuration. The optimization control settings used is depicted in the Figure 3.11. A comparison was also made using another gradient based method, the conjugate gradient algorithm. No significant differences were observed in the calibrated response between the two optimization approaches.

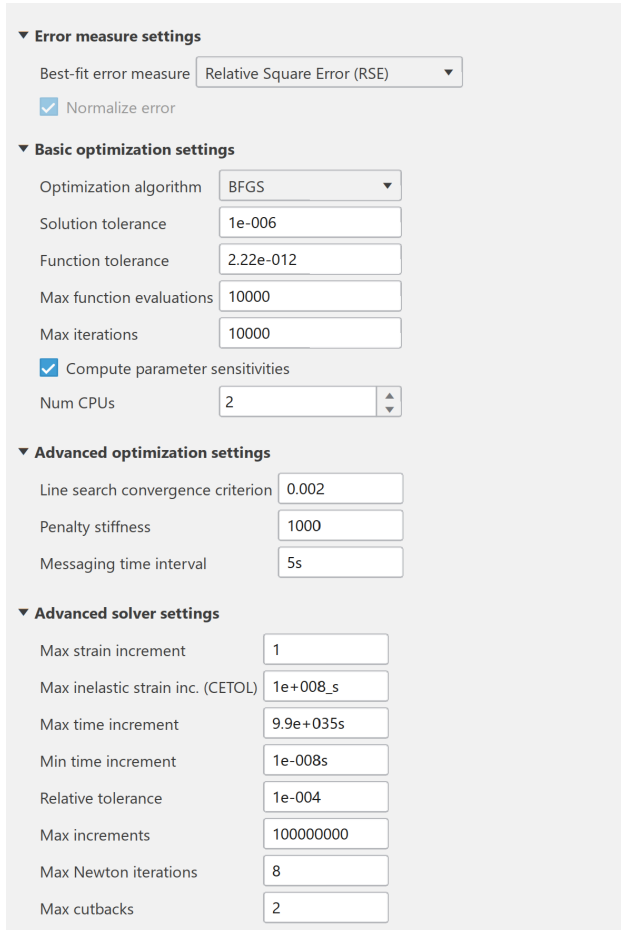


**Figure 3.11:** Optimization setting used for material calibration.

### Material calibration: Crushable foam material model

The calibration of the crushable foam model also consists of two parts: the elastic region and the plastic (crushable) region. For the elastic portion, a similar approach was followed as in the elasto-plastic model. The Young's modulus was obtained from the slope of the initial linear region of the experimental stress-strain curve. Poisson's ratio, which could not be directly calibrated from uniaxial tests, was assumed to be very low, reflecting the behavior typically observed in foam-like materials.

For the plastic region, a volumetric crushable foam model was selected to capture the nonlinear compressive behavior of the active materials and separator. As in the elasto plastic model, the number of stress strain pairs was set equal to the number of data points beyond the yield point in the experimental curve. The initial value of the compression stress ratio was kept unchanged, while the hydrostatic stress ratio was incrementally increased until the simulated tensile response approached the tensile cutoff observed in the experimental data.

The yield stresses, plastic strains, and both the compressive and hydrostatic yield ratios were selected as parameters for optimization. As with the previous model, a gradient based BFGS optimization algorithm was used, with the relative square

error serving as the cost function. This method enabled the calibrated model to closely fit the experimental response by minimizing the error across all data points.

### 3.4.3 Electrochemical material description

Electrochemical material parameters are specified only for the active material and the separator, as these components are directly involved in ion transport and electrochemical reactions.

#### Electrochemical material definitions in *3DEXPERIENCE*:

In *3DEXPERIENCE*, these properties are defined using the *Material Definition* app. For coupled electrochemical mechanical simulations, both electrochemical and mechanical properties must be provided in the material card. The mechanical properties are specified by updating the calibrated parameters into the material card. The electrochemical parameters includes defining the properties of the electrode materials, electrolyte and the separator. Figure 3.12 depicts the required material parameters for each of the definitions. It is important to note that although thermal coupling is not considered in this study, thermal parameters such as thermal conductivity and specific heat must still be defined. This is because the simulation framework in *3DEXPERIENCE* inherently includes thermal coupling in its formulation. Failure to specify these properties will result in errors during the simulation process. The used thermal parameters for the electrodes are tabulated in the Table 3.6.

Parameter	Positive electrode	Negative electrode
Thermal conductivity (W/(mK))	5	5
Specific heat (J/K/Kg)	900	1437

**Table 3.6:** Thermal material parameters, adopted from [16].

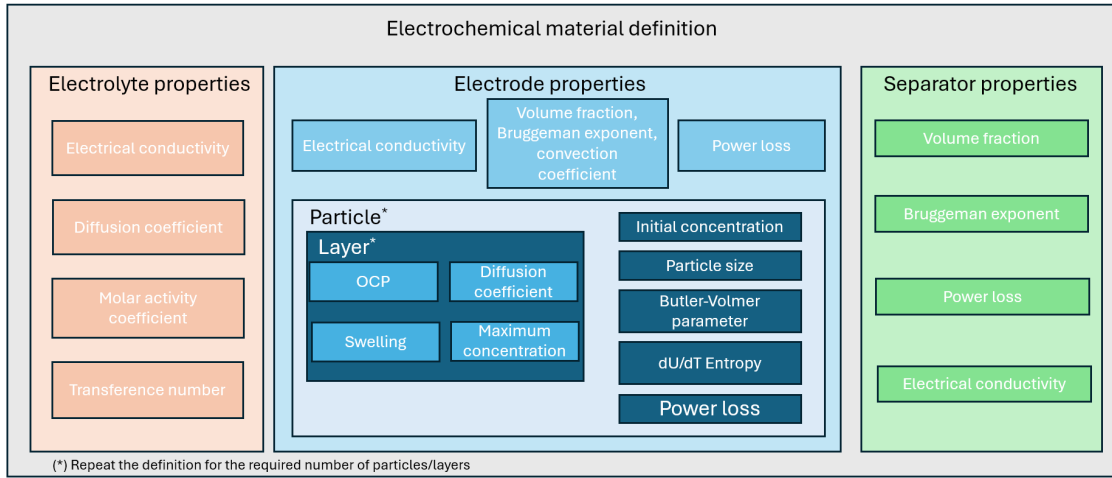


**Figure 3.12:** Flowchart depicting the required electrochemical material definitions.

#### 3.4.3.1 Electrolyte properties

The electrolyte properties are assumed to be uniform across the entire battery domain. In other words, the same electrolyte parameters are used for the negative and positive electrodes, as well as for the separator. In the material card, the electrolyte properties such as conductivity, diffusivity, molar activity and transference number are to be defined as a function of the lithium ion concentration. The electrolyte conductivity of lithium hexafluorophosphate ( $LiPF_6$ ) electrolyte can be approximated using the equation 3.13 [22].

$$\kappa(c, T) = p_1 (1 + (T - p_2)) \cdot c \cdot \frac{(1 + p_3 \cdot \sqrt{c} + p_4 \cdot (1 + p_5 \cdot \exp\left(\frac{1000}{T}\right)) \cdot c)}{(1 + c^4 \cdot p_6 \cdot \exp\left(\frac{1000}{T}\right)))} \quad (3.13)$$

Where,  $\kappa$  is the electrolyte conductivity in the unit ms/cm.  $P_1$  to  $P_6$  are the fitting parameters and are given in the Table 3.7.

Constants	Value
$p_1$ (mS cm <sup>-1</sup> )	0.521
$p_2$ (K)	228
$p_3$ ((mol/L) <sup>-1/2</sup> )	-1.06
$p_4$ (-)	0.353
$p_5$ (-)	-0.00359
$p_6$ ((mol/L) <sup>-4</sup> )	0.00148

**Table 3.7:** Fitting parameters for the equation 3.13, adapted from [22].

The diffusivity property of the electrolyte can be approximated using the equation 3.14 [22].

$$D_{\pm}(c, T) = p_1 \cdot \exp(p_2 \cdot c) \cdot \exp\left(\frac{p_3}{T}\right) \cdot \exp\left(\frac{p_4 \cdot c}{T}\right) \cdot 10^{-6} \quad (3.14)$$

Where, D is the diffusion expressed in  $\text{cm}^2/\text{s}$ . The fitting parameters  $p_1$  to  $P_4$  are given in the Table 3.8.

Constants	Value
$p_1 (\text{cm}^2 \text{s}^{-1})$	1010
$p_2 ((\text{mol/L})^{-1})$	1.01
$p_3 (\text{K})$	-1560
$p_4 ((\text{mol/L})\text{K}^{-1})$	-487

**Table 3.8:** Fitting parameters for the equation 3.14, adapted from [22].

The transference number can be approximated using the equation

$$t_+(c, T) = p_1 + p_2 \cdot c + p_3 \cdot T + p_4 \cdot c^2 + p_5 \cdot c \cdot T + p_6 \cdot T^2 + p_7 \cdot c^3 + p_8 \cdot c^2 \cdot T + p_9 \cdot c \cdot T^2 \quad (3.15)$$

Where,  $t_+$  is the transference number and is dimensionless.  $P_1$  to  $P_9$  are the fitting parameters and the optimal values are appended in the Table 3.9.

Constants	Value
$p_1 (-)$	-12.8
$p_2 (\text{L mol}^{-1})$	-6.12
$p_3 (\text{K}^{-1})$	0.0821
$p_4 ((\text{L/mol})^2)$	0.904
$p_5 ((\text{L/mol})\text{K}^{-1})$	0.0318
$p_6 (\text{K}^{-2})$	$-1.27 \times 10^{-4}$
$p_7 ((\text{L/mol})^3)$	0.0175
$p_8 ((\text{L/mol})^2\text{K}^{-1})$	-0.00312
$p_9 ((\text{L/mol})\text{K}^{-2})$	$-3.96 \times 10^{-5}$

**Table 3.9:** Fitting parameters for the equation 3.15, adapted from [22].

The molar activity coefficient employed in this study is adopted from the Dassault workshop example, "Thermal-Electrochemical-Stress Simulation of Li-ion Batteries". Due to the proprietary nature and sensitivity of the underlying data, the specific model parameters are not disclosed in this manuscript.

### 3.4.3.2 Electrode properties

The electrochemical material definitions for the electrodes have to be defined separately for both macroscale model and microscale particle. Table 3.10 depicts the adopted macroscopic properties for the electrodes.

Parameter	Positive electrode	Negative electrode
Particle volume fraction (%)	70.4	67.1
Electrolyte volume fraction (%)	29.6	32.9
Inactive volume fraction (%)	42	44.5
Bruggeman exponent	0.54	0.64
Electrical conductivity (S/m)	68	14

**Table 3.10:** Macroscopic electrode properties of the negative electrode from [16].

Defining the microscopic properties involves specifying the particle and layer definitions as depicted in the chart in Figure 3.12.

Table 3.11 shows the adopted microscopic particle properties. It has to be noted again here that the battery aging parameters are neglected. Only one particle type is considered for simplicity.

Parameter	Positive electrode	Negative electrode
Particle radius (m)	$6.49 \times 10^{-5}$	$1.37 \times 10^{-5}$
Initial concentration (mol/m <sup>3</sup> )	44,694	670
Cathodic rate constant (m/s)	$2.50 \times 10^{-11}$	$1.19 \times 10^{-10}$
Anodic rate constant (m/s)	$2.50 \times 10^{-11}$	$1.19 \times 10^{-10}$
Cathodic transfer coefficient	0.5	0.5
Anodic transfer coefficient	0.5	0.5
Activation energy in Arrhenius for Butler-Volmer (J/mol)	43,600	54,300
Reference temperature in Arrhenius for Butler-Volmer (K)	298.15	298.15

**Table 3.11:** Microscopic particle properties of the negative electrode from [16].

In the DFN model, the microscopic particles are represented at each macroscopic integration point using the 1D mesh. These mesh parameters are also defined in the layer definition tab. As per the discussion with the representative from the Dassault *3DEXPERIENCE*, a mesh of 30 elements with equivolumetric type element distribution is efficient. The open circuit potential (OCP) of the electrodes are adopted from [23] and are shown in Figure 3.13. The diffusivity properties are taken from [16] and are listed in Table 3.12. The magnitude of the diffusion as a function of normalized concentration is taken from the Dassault "Thermal-Electrochemical-Stress Simulation of Li-ion Batteries" workshop example.

Parameter	Positive electrode	Negative electrode
Maximum particle concentration (mol/m <sup>3</sup> )	48,500	31,920
Activation energy in Arrhenius for diffusivity (J/mol)	80,600	30,300
Reference temperature in Arrhenius for diffusivity (K)	298.15	298.15

**Table 3.12:** Diffusion parameters for the microscale particle, adopted from [16].

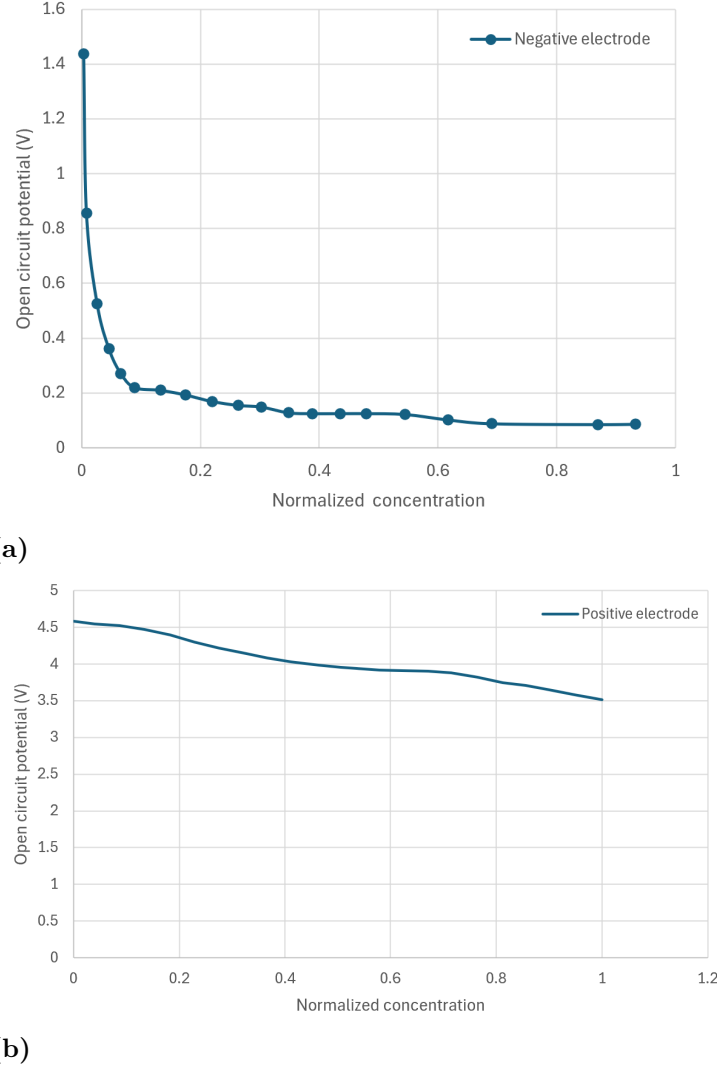


**Figure 3.13:** Open circuit potential vs normalized concentration (a) for negative electrode and (b) for positive electrode adopted from [23].

The swelling coefficient of the electrodes are also defined in layer tab. The computed effective swelling coefficient from the subsection 3.4.7 is used here. The computed effective swelling coefficient is tabulated as a function of normalized lithium-ion concentration and defined in the material card.

### 3.4.3.3 Separator properties

The separator properties such as volume fraction, Bruggeman exponent, power loss and electrical conductivity for the simulation are taken from the Dassault "Thermal-Electrochemical-Stress Simulation of Li-ion Batteries" workshop example. Due to the proprietary nature and sensitivity of the underlying data, the specific model parameters are not disclosed in this manuscript.

### 3.4.4 Mechanical boundary condition

The effective volume expansion of the stack is analyzed by considering two different boundary conditions i.e. a periodic and a symmetry boundary conditions. Periodic boundary condition allows the stack to freely deform without introducing any mechanical constraints whereas the symmetry boundary condition constrains the inplane deformation of the stack. More details on these boundary conditions and their implementation in *3DEXPERIENCE* is presented in the following Subsections.

#### 3.4.4.1 Periodic boundary conditions

Since the RVE is intended to represent a portion of a larger continuum, its mechanical response must accurately reflect the macroscopic behavior of the full system, without introducing artificial boundary effects. PBC are particularly well-suited for this purpose, as they maintain displacement continuity and traction equilibrium between opposite faces of adjacent RVEs.

#### Implementation in *3DEXPERIENCE*:

In the context of the *3DEXPERIENCE* platform, periodicity is implemented by first constructing an RVE abstraction shape using the *Structural Model Creation* app. The procedure involves selecting the opposing faces of the RVE, typically on the electrode geometry and designating them as master and slave surfaces. These surfaces are then linked in a way that enforces periodicity across the model. As a result, a surface-based PBC is established, allowing the RVE to deform consistently with its periodic neighbors under external loading conditions. Figure 3.14 depicts the periodic boundary constraints applied to the RVE.

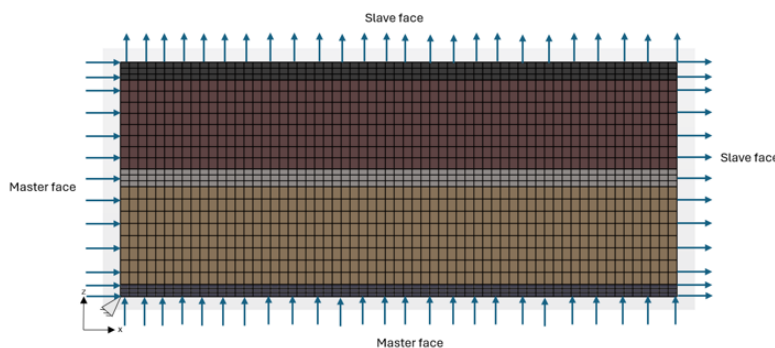


**Figure 3.14:** Periodic boundary condition applied on the mesoscale RVE.

#### 3.4.4.2 Symmetry boundary conditions

A symmetry boundary condition is applied, wherein the side faces are constrained such that the RVE can only deform in the thickness direction. Figure 3.15 depicts the applied symmetry constraint. The reason for choosing this boundary condition

stems from the fact that there is no surface irregularities considered in the plane of the electrodes and the considered RVE is small such that there are no in-plane variations of the key variables and the only variations occur in the out-of-plane direction. Based on this assumption, symmetry boundary conditions are applied to simplify the mechanical constraints while still capturing the essential out-of-plane behavior.

#### **Implementation in *3DEXPERIENCE*:**

In *3DEXPERIENCE*, symmetry boundary conditions are applied by selecting the side faces of the RVE within the *Mechanical Scenario Creation* app. The constraint is enforced using the Fixed Displacement option available in the Boundary Condition tab. Specifically, displacements along the in-plane directions i.e., the  $x$ - and  $y$ -axes are constrained. Figure 3.15 depicts the applied symmetry constraint.

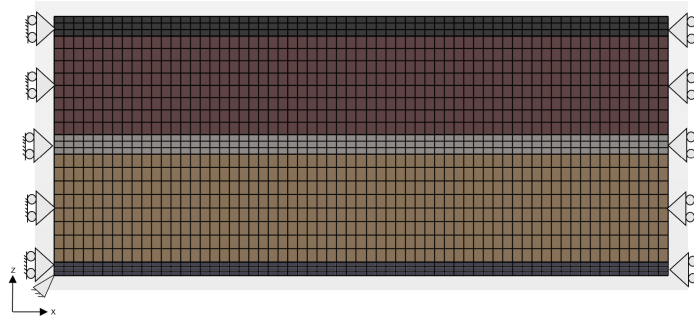


**Figure 3.15:** Symmetry boundary condition applied on the mesoscale RVE.

#### **Electrical boundary conditions:**

The electrical boundary condition is applied by considering a galvanostatic charging case, where in, the negative current collector is grounded and a constant current is applied to the positive current collector. It has to be noted here that the *3DEXPERIENCE* applies an insulated boundary condition when a boundary is left unconstrained. The applied electric boundary condition is depicted in the Figure 3.16.

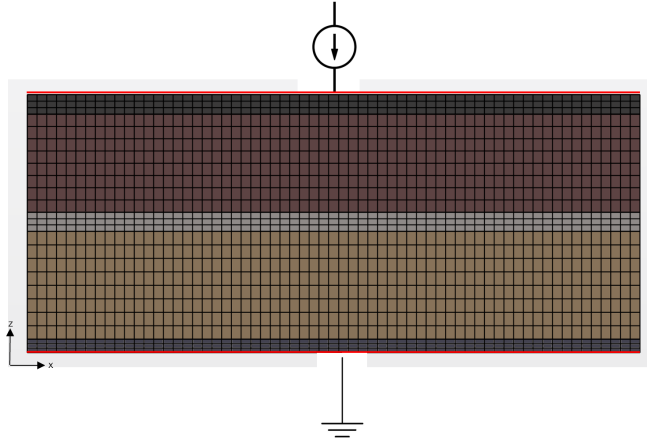


**Figure 3.16:** Electrical boundary condition applied on the mesoscale RVE.

### 3.4.5 Initial condition

For the coupled simulation, the following initial conditions are required to be specified:

- Temperature (T)
- Lithium ion concentration in the electrolyte ( $c_e^0$ )
- Solid electric potential ( $\phi_{sa}^0$  and  $\phi_{sc}^0$ )
- Electrolyte electric potential ( $\phi_e^0$ )

A room temperature of 298.15 K is assumed as the initial condition. Additionally, the initial concentration of lithium ions in the electrolyte is set to 1 mol/L, based on the reference [16].

As per the *3DEXPERIENCE* guidelines, the initial electric potential of the solid and the electrolyte is chosen such that the initial overpotential is zero. That is

$$\eta^0 = \phi_{sa}^0 + \phi_{sc}^0 - \phi_e^0 - E_{ocp}(c_s^0) \quad (3.16)$$

Where,  $\phi_{sa}^0$  is the initial solid electric potential of the negative electrode,  $\phi_{sc}^0$  is the initial solid electric potential of the positive electrode,  $E_{ocp}$  is the open circuit potential of the electrodes and  $c_s^0$  is the initial lithium ion concentration in the solid electrode.

Since, the negative current collector is grounded as mentioned in the previous subsection,  $\phi_{sa}^0$  will be zero. With this, equation 3.16 reduces to

$$\phi_e^0 = -E_{ocp}(c_s^0) \quad (3.17)$$

In the above equation, the magnitude  $E_{ocp}$  as a function of initial lithium ion concentration in the negative electrode is taken by referring the open circuit potential chart of the negative electrode. With this equation, the initial electric potential of the electrolyte can be determined. To calculate the initial electric potential of the

positive electrode, the solution from the equation 3.17 is substituted into the equation 3.16 keeping the initial overpotential as zero and taking the magnitude of  $E_{ocp}$  as a function of the initial concentration of the lithium ion in the positive electrode by referring to the open circuit potential chart of the positive electrode. Table 3.13 summarizes the applied initial conditions to the mesoscale RVE model.

Parameter	Initial value
$\theta$	298.15 K
$c_e^0$	1 mol/L
$\phi_e^0$	-0.675
$\phi_{sa}^0$	0
$\phi_{sc}^0$	3.08

**Table 3.13:** Initial conditions applied on the mesoscale RVE.

### 3.4.6 Loading condition and simulation setup

Using the defined boundary conditions, initial conditions, and calibrated material models, the simulation is set up in *3DEXPERIENCE* using the coupled thermal-electrochemical-stress procedure within the *Mechanical Scenario Creation* app. Two analysis steps are configured. In the first step, all boundary and initial conditions are applied. In the second step, a constant current of  $6 \times 10^{-6}$  A is applied to the positive current collector. The applied current magnitude is determined by scaling down the current density of the full battery cell to the surface area of the RVE. This ensures consistency in the electrochemical loading conditions between the RVE and the actual battery.

The current density of the full cell is given by:

$$J = \frac{I_{\text{cell}}}{A_{\text{cell}}} \quad (3.18)$$

Where, J is the current density,  $I_{\text{cell}}$  is the current required for the battery to fully charge,  $A_{\text{cell}}$  is the electrode surface area of the battery.

The corresponding current to be applied to the RVE is:

$$I_{\text{RVE}} = J \cdot A_{\text{RVE}} = \frac{I_{\text{cell}}}{A_{\text{cell}}} \cdot A_{\text{RVE}} \quad (3.19)$$

Where,  $I_{\text{RVE}}$  is the scaled current applied on the RVE and  $A_{\text{RVE}}$  is the surface area of the RVE where the current is applied.

The computed current corresponds to an approximate 1 C-rate. A step control condition is also implemented to terminate the simulation once the terminal voltage reaches 4.2 V, which represents 100% state of charge (SOC). It has to be noted here that only the constant current charging case is considered in this work.

In both analysis steps, an unsymmetric stiffness matrix storage scheme is activated to handle the nonlinearities and multiphysics coupling. Due to convergence challenges often associated with coupled simulations, small time increments are used to ensure numerical stability and convergence of the solution. Figure 3.17 illustrates the used time steps and increments for the two analysis steps.

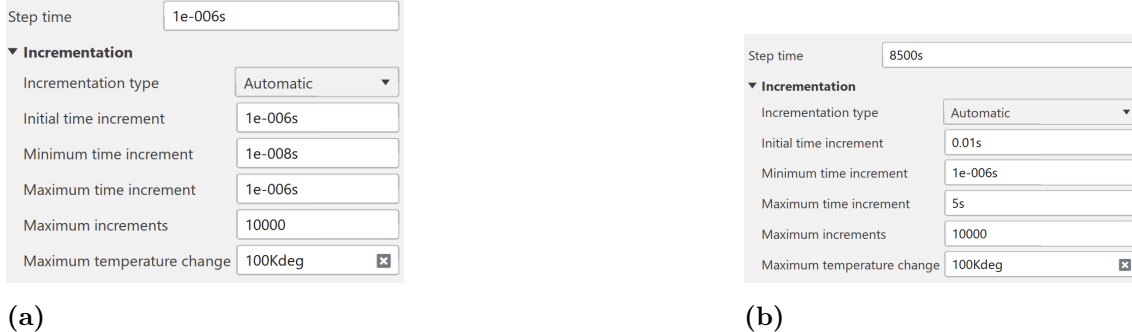


**Figure 3.17:** Time increments used for (a) first analysis step, (b) second analysis step.

### 3.4.7 Upscaling to macroscale: Effective volume change determination

To evaluate the average volumetric strain resulting from electrochemically induced mechanical deformation, a volume-averaged sum of the normal strain components at all Gauss integration points is computed. This gives a representative measure of the effective volume change in the RVE. The volume-averaged volumetric strain  $\bar{\epsilon}_v$  is calculated as:

$$\bar{\epsilon}_v = \frac{1}{V_{\text{total}}} \int_V \epsilon_v dV \approx \frac{\sum_{i=1}^n (\epsilon_{11}^{(i)} + \epsilon_{22}^{(i)} + \epsilon_{33}^{(i)}) V_i}{\sum_{i=1}^n V_i} \quad (3.20)$$

Here,  $\epsilon_{11}^{(i)}, \epsilon_{22}^{(i)}, \epsilon_{33}^{(i)}$  are the normal strain components in the three principal directions at Gauss point  $i$ , and  $V_i$  is the corresponding Gauss point volume.

This computed volume averaged strain is given as a prescribed load in the macroscale model. To compute the total volume change, the volume averaged strain is then multiplied with the initial volume of the RVE.

## 3.5 Macroscale modeling: Cell level response

The macroscale model represents the complete cell architecture. While the mesoscale model explicitly captures the layered structure of electrodes and separator, modeling the entire jellyroll at this resolution would be computationally expensive. Therefore, at the cell level, the jellyroll is modeled as a homogenized medium to reduce computational cost. The primary objective at this scale is to simulate the overall cell expansion resulting from change in the state of charge, by applying the effective

volumetric change obtained from the mesoscale model. This expansion is evaluated under the mechanical constraint imposed by the cell casing.

### 3.5.1 Geometry and model setup

The macroscale model of the battery cell consists of two jellyrolls, which are modeled as a homogenized medium, and a casing. The CAD model of the macroscale cell is shown in Figure 3.18.

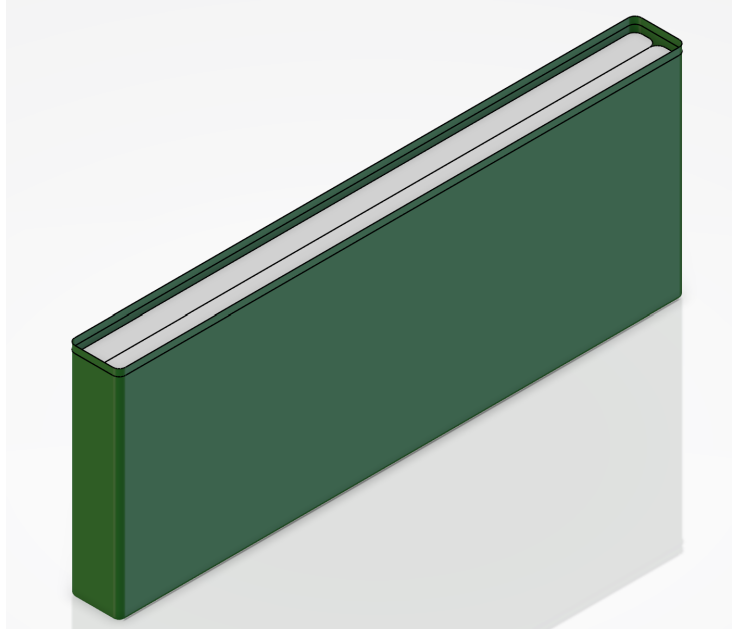


**Figure 3.18:** CAD model of the cell consisting of jellyroll and a casing.

The jellyrolls are inserted into the casing with a loose fit, maintaining a uniform gap between them throughout. The jellyroll is discretized using C3D8 brick elements, while the casing is modeled using S4 and S3 shell elements. The finite element model of the entire cell is shown in Figure 3.19.

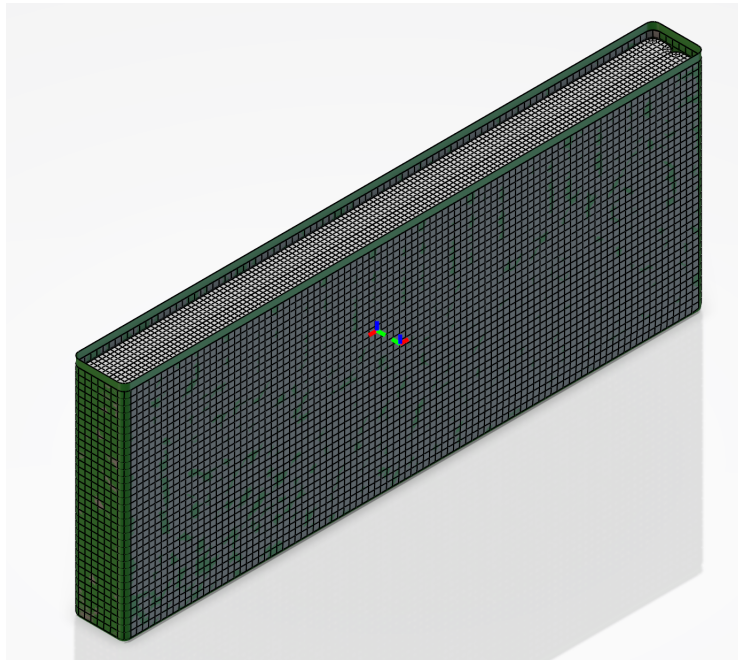


**Figure 3.19:** Finite element model of the cell consisting of jellyroll and a casing.

### 3.5.2 Constitutive model

The casing of the cell is modeled using a linear elastic material model. Typically, the cell casing is made of aluminum. The material properties of the casing are summarized in Table 3.14.

Parameter	Magnitude
Young's Modulus	70 GPa
Poisson's ratio	0.33

**Table 3.14:** Casing material properties, adopted from [4].

The jellyroll is modeled using a crushable foam material model to capture its nonlinear compressive behavior under mechanical loading. In reality, the jellyroll exhibits a transversely isotropic mechanical response due to the layered structure of electrode and separator sheets. However, the crushable foam material model available in *3DEXPERIENCE* supports only isotropic elastic behavior. As a result, the elastic response of the jellyroll is assumed to be isotropic for simulation purposes. To characterize the mechanical behavior of the homogenized jellyroll under this isotropic assumption, a virtual material characterization is performed using a mesoscale RVE. Since isotropy is assumed, it is sufficient to characterize the response in a single direction to represent the overall material behavior.

#### Virtual testing setup in *3DEXPERIENCE*:

The mesoscale RVE is imported into the *Mechanical Scenario Creation* app within *3DEXPERIENCE*. A static step procedure is employed for the analysis. To ensure a

uniform and representative deformation, strain-controlled PBC's are applied, which help avoid the introduction of artificial stress concentrations. A uniform strain of 1% is imposed along the out-of-plane (thickness) direction, as this is the primary direction in which the active material undergoes volumetric expansion due to lithium-ion intercalation. The stress-strain response of the model is computed by volume averaging the stress and the strain in the out of plane direction at each Gauss integration points. The characterized material response is then calibrated using the crushable foam material model using the *Material Calibration* app.

### 3.5.3 Boundary condition and loads

Due to the presence of the cell casing, the free expansion of the jellyroll is constrained, resulting in the development of internal stresses and strains within the battery. The effective mechanical response of the jellyroll arising from both the external constraints (such as the cell casing) and changes in the state of charge can be described using the strong form of the momentum balance equation. Assuming a linear elastic material response, this strong form can be written as:

$$\bar{\bar{\sigma}} = \bar{\bar{E}} : (\bar{\bar{\epsilon}} - \bar{\Omega}^{\text{eff}} \Delta \text{SOC}) \quad (3.21)$$

Where,  $\bar{\bar{\sigma}}$  represents the overall stress due to the applied mechanical constraints as well as the volumetric strains due to the change in the SOC,  $\bar{\bar{\epsilon}}$  represents the strain due to applied mechanical constraints and  $\bar{\Omega}^{\text{eff}}$  represents the swelling coefficient of the homogenized jellyroll.

It should be noted that the formulation presented in the equation 3.21 describes a linear elastic material response, whereas the material model used for the homogenized jellyroll is crushable foam which is a non-linear material model. The purpose of demonstrating the linear elastic swelling model is to show consistency with the formulation provided in Equation 3.6, which characterizes the effective microscale response to swelling under the assumption of linear elasticity. In this context, the term  $\Delta c_{s,p}^{\text{avg}}$  in Equation 3.6 represents the change in lithium-ion concentration within a single electrode (either positive or negative). In the corresponding macroscale formulation, shown in Equation 3.21, this term is replaced by  $\Delta \text{SOC}$ , which reflects the overall change in state of charge and accounts for concentration changes in both electrodes.

The effective response of the jellyroll considering the non-linear constitutive model can be represented in the strong form as:

$$\hat{\bar{\sigma}} = \hat{\bar{\sigma}}(\bar{\bar{\epsilon}} - \bar{\Omega}^{\text{eff}} \Delta \text{SOC}) \quad (3.22)$$

Where,  $\hat{\bar{\sigma}}(\bar{\bar{\epsilon}} - \bar{\Omega}^{\text{eff}} \Delta \text{SOC})$  represents the effective stress response is a function of the change in the SOC as well as the applied mechanical constraints.

The above formulation is consistent with the non-linear swelling model presented in the equation 3.10. In this context, the term  $\Delta c_{s,p}^{\text{avg}}$  in Equation 3.10 is replaced by the term  $\Delta \text{SOC}$  to account for the concentration changes in both electrodes.

### Implementation in *3DEXPERIENCE*:

In the *Mechanical Scenario Creation* app, a general static analysis procedure is employed at the macroscale level. The bottom face of the cell casing is fully constrained in all degrees of freedom to provide structural support. A frictionless, penalty-based general contact interaction is defined between the jellyroll and the casing to allow relative motion without resistance, simulating a loosely fitted interface. Between the two jellyrolls, a tied contact condition is applied to ensure they deform together as a single body.

The effective volumetric strain resulting from lithium-ion intercalation, as computed in subsection 3.4.7, is imposed on the jellyroll. Since *3DEXPERIENCE* does not provide a direct method to apply strain fields onto the model, an alternative approach is used to indirectly apply the strain. In this approach, swelling coefficient of the homogenized jellyroll is calculated based on the imposed volumetric strain and the change in the SOC as

$$\bar{\Omega}^{\text{eff}} = \frac{\bar{\varepsilon}_v^{\text{ch}}}{\Delta \text{SOC}} \quad (3.23)$$

Where,  $\bar{\varepsilon}_v^{\text{ch}}$  is the imposed effective volumetric strain on the jellyroll,  $\bar{\Omega}^{\text{eff}}$  is the effective swelling coefficient of the homogenized jellyroll,  $\Delta \text{SOC}$  is the change in the state of charge.

It is important to note that (i) the change in concentration,  $\Delta c_{s,p}^{\text{avg}}$ , presented in equation 3.4 for the microscale model represents the change in lithium ions within a single electrode, whether positive or negative. In the macroscale model, a similar formulation is applied, as seen in equation 3.23. However, in this case, the term  $\Delta c_{s,p}^{\text{avg}}$  is replaced with  $\Delta \text{SOC}$ . This adjustment is made to account the change in concentration in the homogenized jellyroll. (ii) In the formulation presented above, the term  $\bar{\Omega}^{\text{eff}}$  characterizes the effective swelling coefficient of the homogenized jellyroll without considering the effect of the cell casing on the stress-free volumetric expansion of the jellyroll.

When the battery is fully charged, SOC will be equal to 1 and in a fully discharged state SOC will be equal to 0. The volumetric strain will be equal to the effective volumetric strain computed in the subsection 3.4.7. Using the equation, 3.23, the effective swelling coefficient can be computed. This effective swelling coefficient is adopted as the coefficient of thermal expansion in the material card of the homogenized jellyroll. The SOC is implemented as a tabular data ranging from 0 to 1 using the Predefined Temperature option in the predefined field in *Mechanical Scenario Creation* app. The total number of time steps in the simulation is chosen to match the number of data points in the tabular input data, ensuring that each time increment corresponds to a specific data point in the charging profile.

# 4

## Results and discussion

### 4.1 Microscale model

#### 4.1.1 Case 1: Linear elastic constitutive model

##### 4.1.1.1 Load case 1: Homogenized material response

###### Negative electrode RVE:

The material response of the microscale model was characterized by virtually testing the Representative Volume Element (RVE) under six distinct loading conditions, as outlined in Subsection 3.2. The resulting behavior under both principal and shear loading directions is illustrated in Figures 4.1 and 4.2, respectively.

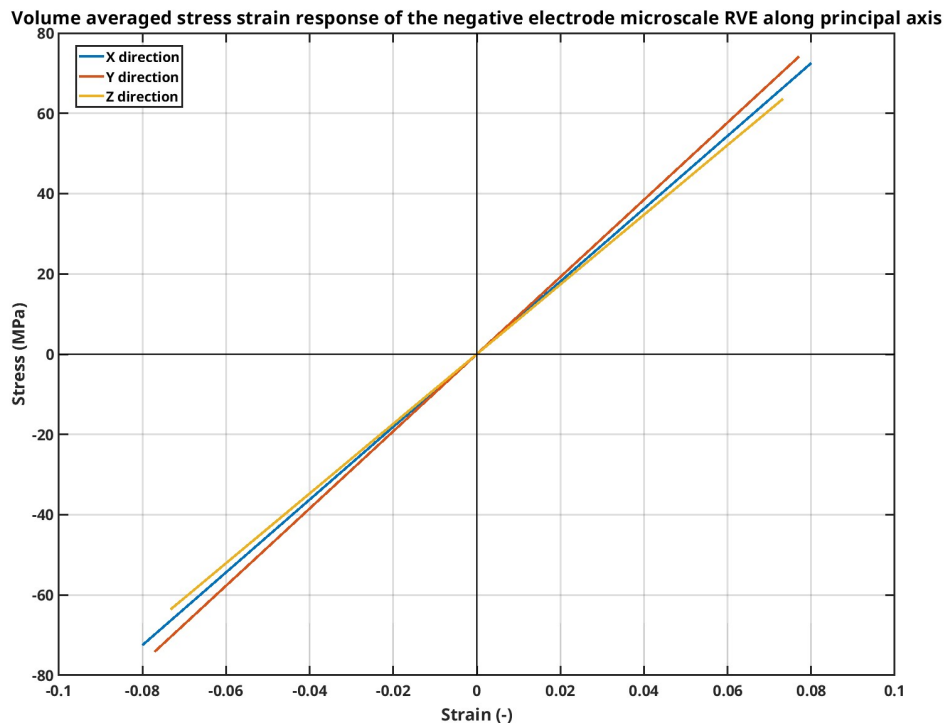


**Figure 4.1:** Response of the linear elastic RVE along normal directions.

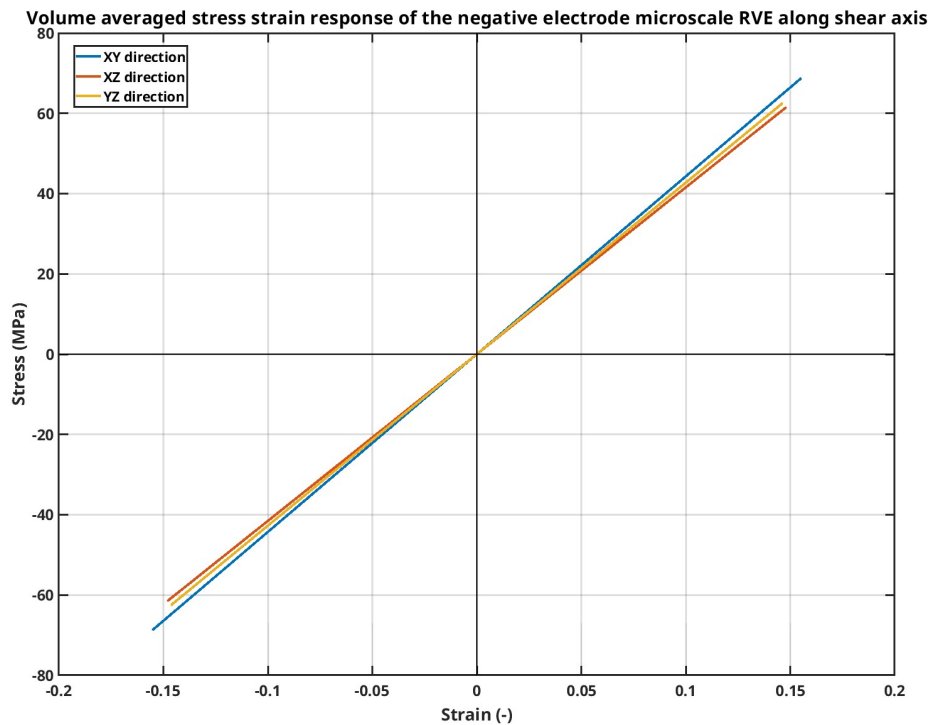


**Figure 4.2:** Response of the linear elastic RVE along shear directions.

Since a linear material model is assumed for both the matrix and the inclusions, the responses in compression and tension, as shown in Figures 4.1 and 4.2, are identical.

In a battery cell, the electrode response is transversely isotropic due to uniform material properties within the electrode plane and the presence of a layered structure along the thickness direction. As the microscale RVE is extracted from a region within this plane, it is reasonable to assume isotropy for the purpose of calibrating the material response at the microscale level. The results from the virtual tests were calibrated using the *Material Calibration* app in *3DEXPERIENCE* to determine the effective stiffness modulus of the RVE. Figure 4.3 shows the calibrated response curve alongside the corresponding test data points. To evaluate the accuracy of the calibration, the coefficient of determination ( $R^2$ ) was used as the error metric. The resulting error between the test data and the calibrated response is summarized in Table 4.2.

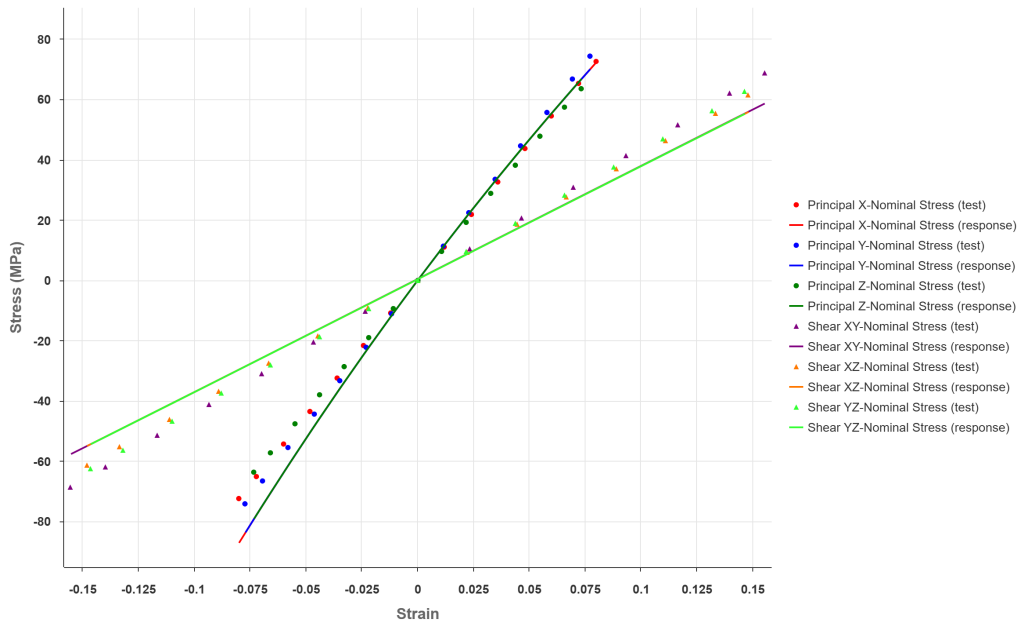


**Figure 4.3:** Calibrated curve and the test data points considering the isotropic elastic response.

Loading direction	Coefficient of determination of R2
X direction	0.983
Y direction	0.993
Z direction	0.972
XY direction	0.976
XZ direction	0.99
YZ direction	0.985

**Table 4.1:** Error between the test data point and the calibrated curve.

#### Positive electrode RVE:

Similar to the negative electrode, the virtual testing is done to characterize the response of the positive electrode considering linear elastic material model for both LiMn<sub>2</sub>O<sub>4</sub> inclusions and matrix. The obtained response for principal and shear loading cases are depicted in Figure 4.4 and 4.5.

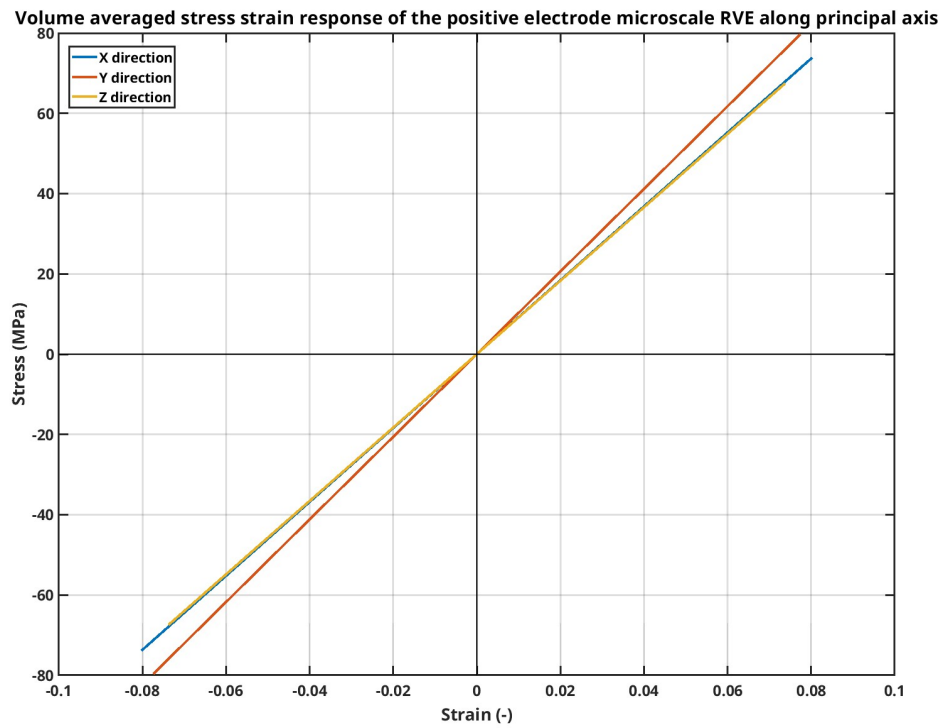


**Figure 4.4:** Response of the linear elastic RVE along normal directions.

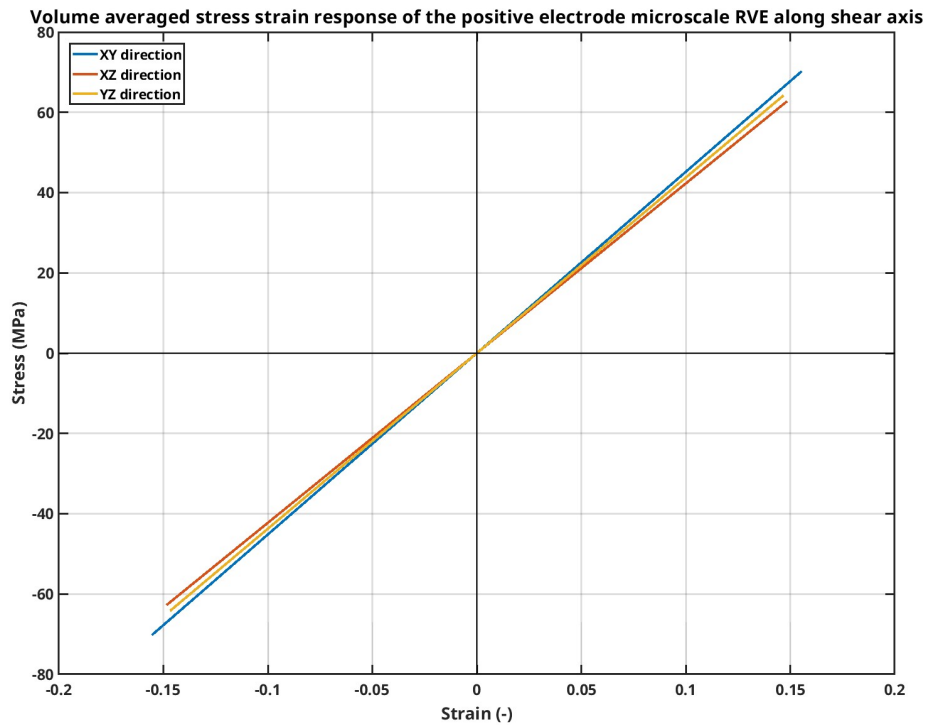


**Figure 4.5:** Response of the linear elastic RVE along shear directions.

Similar to the responses characterized from the negative electrode, a tension compression symmetry can be observed in this case as well. The material responses are further calibrated to extract the homogenized material parameters. Figure 4.6 shows the test data points and the calibrated response curve. Coefficient of determination of R<sup>2</sup> is also used in this case to compute the error between the fitted response and the actual response. Table 4.2 shows the error obtained in each loading directions.

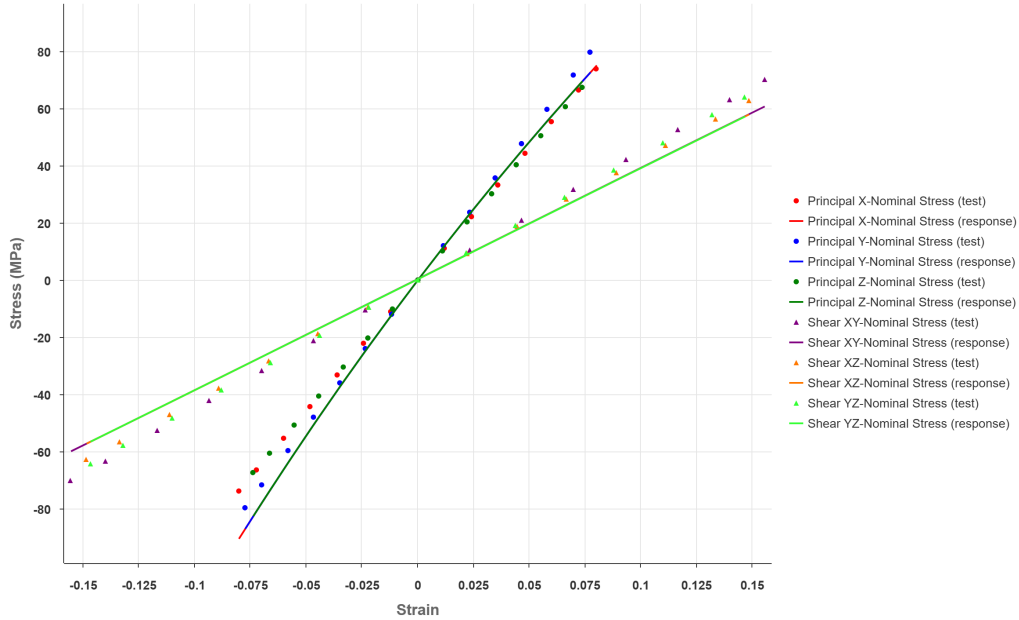


**Figure 4.6:** Calibrated curve and the test data points considering the isotropic elastic response.

Loading direction	Coefficient of determination of R2
X direction	0.974
Y direction	0.994
Z direction	0.978
XY direction	0.98
XZ direction	0.993
YZ direction	0.987

**Table 4.2:** Error between the test data point and the calibrated curve.

It should be noted that only uniaxial virtual tests were conducted in this study. Due to the unavailability of volumetric deformation data, the Poisson's ratio could not be calibrated. As a result, only the effective Young's modulus was extracted from the calibration process. Given that the volume fraction of the inclusions is relatively small compared to that of the matrix, the effective response of the RVE is primarily governed by the behavior of the matrix material. Therefore, the Poisson's ratio of the matrix is assumed to represent the effective Poisson's ratio of the RVE. The calibrated material properties obtained from the simulation are summarized in Table 4.3.

Parameter	Negative electrode	Positive electrode
Young's Modulus (GPa)	0.988	1.024
Poisson's ratio	0.01	0.01

**Table 4.3:** Calibrated homogenized response of the microscale RVE.

As a validation step for the calibrated parameters, the effective elastic modulus was also estimated analytically using the inverse rule of mixtures. Given the low volume fraction and random distribution of the inclusions, the inverse rule of mixtures provides a reasonably accurate approximation of the actual effective elastic response. Using the analytical expression shown in Equation 4.1, the computed effective elastic modulus is presented in Table 4.4.

$$\frac{1}{E_{eff}} = \frac{\nu_i}{E_i} + \frac{\nu_m}{E_m} \quad (4.1)$$

Where,  $E_{eff}$  is the effective Young's modulus of the microscale RVE,  $\nu_i$  is the volume fraction of the inclusions,  $\nu_m$  is the volume fraction of the matrix,  $E_i$  and  $E_m$  are the Young's modulus of the inclusions and matrix respectively.

Parameter	Negative electrode	Positive electrode
Young's Modulus (GPa)	1.01	1.03

**Table 4.4:** Analytically calculated homogenized response of the microscale RVE.

Comparing the Table 4.3 and Table 4.4, it can be concluded that the calibrated elastic modulus closely matches with the analytical calculation.

#### 4.1.1.2 Load case 2: Effective response due to lithiation

##### Swelling of negative electrode:

As discussed in Subsection 3.2, the graphite inclusions undergo volumetric expansion while being constrained by the surrounding binder matrix. Figures 4.7a and 4.7b present contour plots illustrating the distribution of maximum principal strain and Von-mises stress, respectively, within the RVE as a result of the swelling of the graphite inclusions.

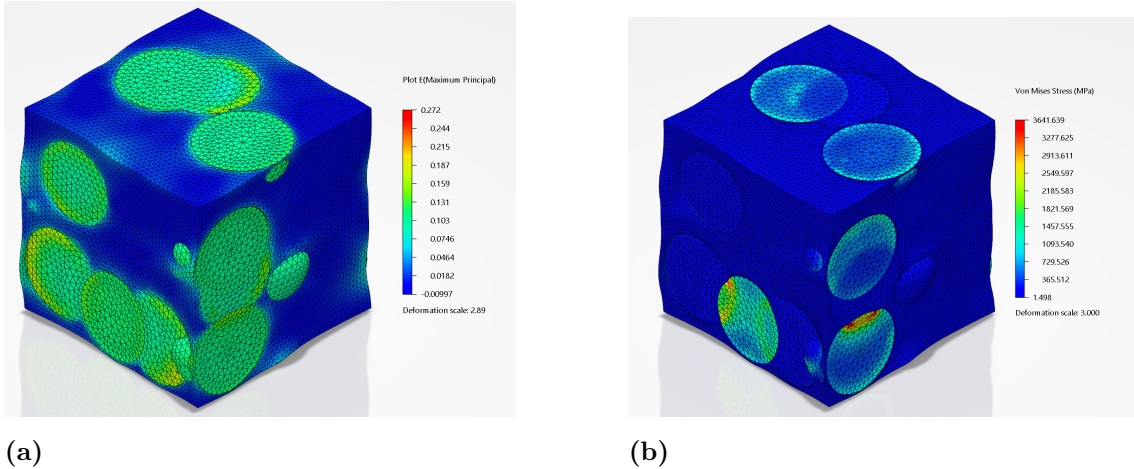


**Figure 4.7:** Contour plot illustrating the a) Maximum strain distribution in the RVE, b) Von-Mises Stress distribution in the RVE due to the swelling of the graphite inclusions.

As mentioned earlier, the inclusions are randomly distributed within the matrix. Consequently, some inclusions intersect the boundaries of the RVE, but the overall arrangement is not periodic. As a result, the generated mesh does not exhibit perfect periodicity. When PBC are applied to not a perfect periodic mesh, interactions between inclusions located on opposite faces of the RVE can be observed. This influence is evident in the contour plots of maximum principal strain and Von-mises stress, as shown in Figures 4.7a and 4.7b.

Figure 4.8 illustrates the evolution of the effective stress as a function of normalized lithium ion concentration.

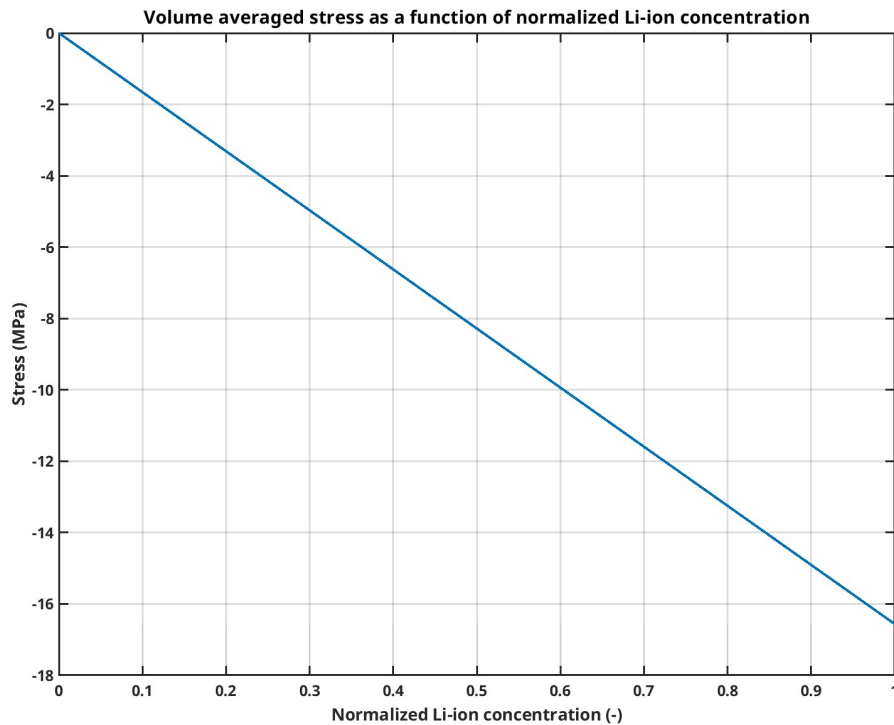


**Figure 4.8:** Volume averaged stress as a function of normalized Li-ion concentration.

From Figure 4.8, it can be observed that the swelling induces a compressive stress. This behavior arises from the volumetric expansion of the inclusions, which leads to an overall expansion of the RVE. In this context, swelling is treated as a positive deformation, hence the strain is positive. However, due to the presence of the surrounding matrix, the free expansion of the inclusions is constrained. As a result, the matrix experiences compressive stress. Given that the volume fraction of the matrix is significantly higher than that of the inclusions, the compressive stress contribution from the matrix dominates the overall response. Also, it can be observed that the maximum compressive stress arises when the lithium ion concentration becomes maximum which is as expected.

**Calculation of the effective swelling coefficient of the negative electrode**  
As observed in Figure 4.8, the maximum stress is induced when the Li-ion concentration reaches 1. In this case, the maximum volume-averaged stress in the negative electrode RVE is approximately  $-16$  MPa. The calibrated effective elastic modulus of the negative electrode RVE, as reported in Table 4.3, is  $0.988$  MPa.

Now, using Equation 3.8, which defines the effective swelling coefficient for the fully lithiated state as:

$$\Omega^{el} = -\bar{\mathbf{E}}^{-1} : \bar{\boldsymbol{\sigma}}_o(1) \quad (4.2)$$

The effective swelling coefficient  $\Omega^{el}$  can be determined as  $0.016$ .

It is important to note that if the matrix were omitted and the inclusions were allowed to swell freely without constraints, a 10% volume expansion of inclusions at a volume fraction of 30% would result in an overall volumetric expansion of approximately 3%. In this idealized case, the effective swelling coefficient would be  $\Omega = 0.03$ , which represents the theoretical upper bound for the selected RVE configuration. However, due to the presence of the matrix, this overall expansion is reduced to 1.6%. Therefore, it should be recognized that increasing the volume fraction of inclusions tends to increase the swelling coefficient, while an increase in the matrix volume fraction leads to a decrease in the swelling coefficient.

### Shrinking of the positive electrode

The extraction of Li-ions decreases the volume of the  $\text{LiMn}_2\text{O}_4$  inclusions. The overall strain and the stress distribution in the RVE due to the shrinkage of the inclusions are shown in the Figure 4.9a and 4.9b

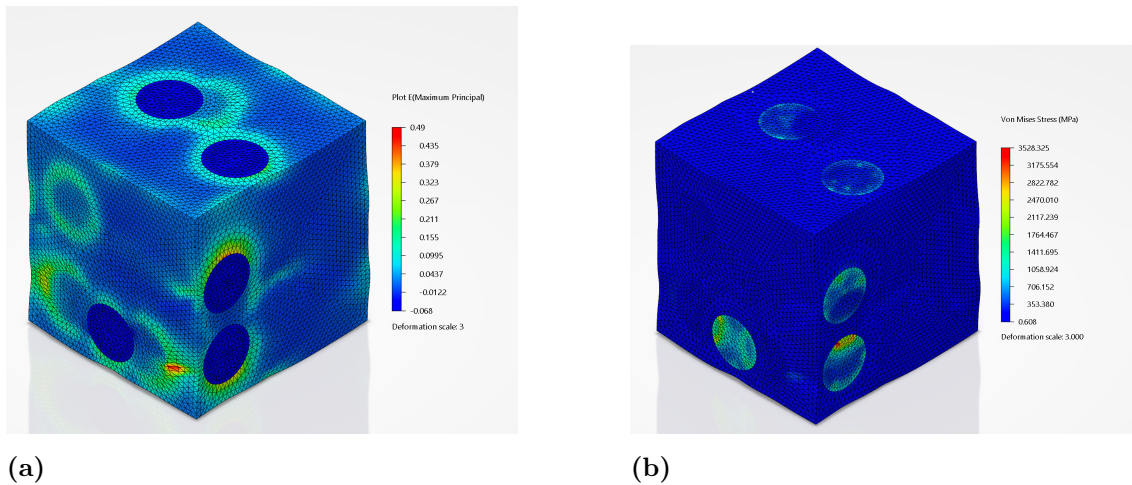


**Figure 4.9:** Contour plot illustrating the a) Maximum strain distribution in the RVE, b) Von-mises Stress distribution in the RVE due to the shrinking of the  $\text{LiMn}_2\text{O}_4$  inclusions.

From the above figures, it can be observed that the maximum strain occurs near the interface between the inclusion and the matrix. Due to the shrinkage of the inclusion, the surrounding matrix experiences tensile stress, resulting in an overall tensile response of the RVE. Since shrinkage is considered as a negative deformation, the effective strain is negative.

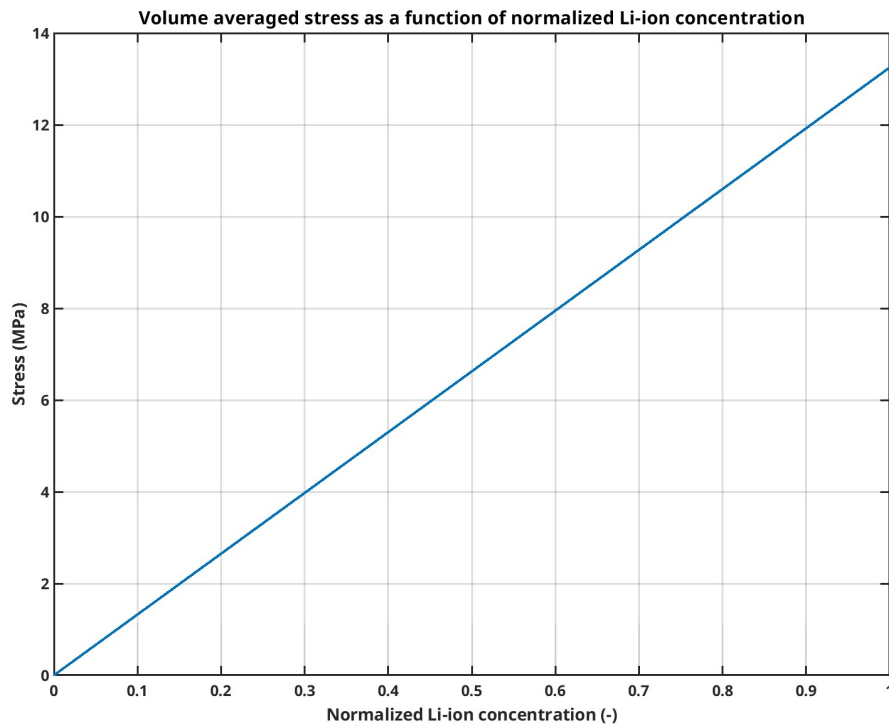


**Figure 4.10:** Volume averaged stress as a function of normalized Li-ion concentration.

From Figure 4.10, it can be seen that for positive electrode, the initial normalized concentration starts at 1 when the charging process begins. In this study, it is assumed that the 100 % Li-ions present in the positive electrode is utilized in the electrochemical reactions to simplify the calculations. In reality, the consumption of 100 % Li-ions might lead to structural collapse of the positive electrode.

#### Calculation of effective shrinking coefficient of the positive electrode

As observed in Figure 4.10, the maximum stress in the positive electrode RVE occurs when the Li-ion concentration reaches 1. In this case, the volume-averaged stress is approximately 13.5 MPa. The calibrated effective elastic modulus of the positive electrode RVE, as presented in Table 4.3, is 1.024 MPa.

Now using the equation 3.8, the effective swelling coefficient can be computed at fully delithiated state as

$$\Omega^{el} = -\bar{\mathbf{E}}^1 : \bar{\boldsymbol{\sigma}}_o(1) \quad (4.3)$$

The effective swelling coefficient  $\Omega^{el}$  can be determined as 0.012.

If the matrix phase is excluded from the analysis and the inclusions are allowed to shrink freely, the effective swelling coefficient is found to be  $\Omega_{eff} = 0.020$ , which represents the theoretical upper bound for the current RVE configuration under shrinkage. Comparing this value with the calculated effective swelling coefficient,

it can be inferred that, unlike during swelling, the influence of the binder on the overall shrinkage behavior is minimal.

#### 4.1.2 Case 2: Non-linear constitutive model

##### 4.1.2.1 Load case 1: Homogenized material response

###### Negative electrode RVE:

Similar to the linear elastic material response, the load case 1 is used to characterize the homogenized response of the RVE by macroscopic strain along six distinct loading directions. The resulting response under both normal and shear loading directions is illustrated in Figures 4.11 and 4.12, respectively.

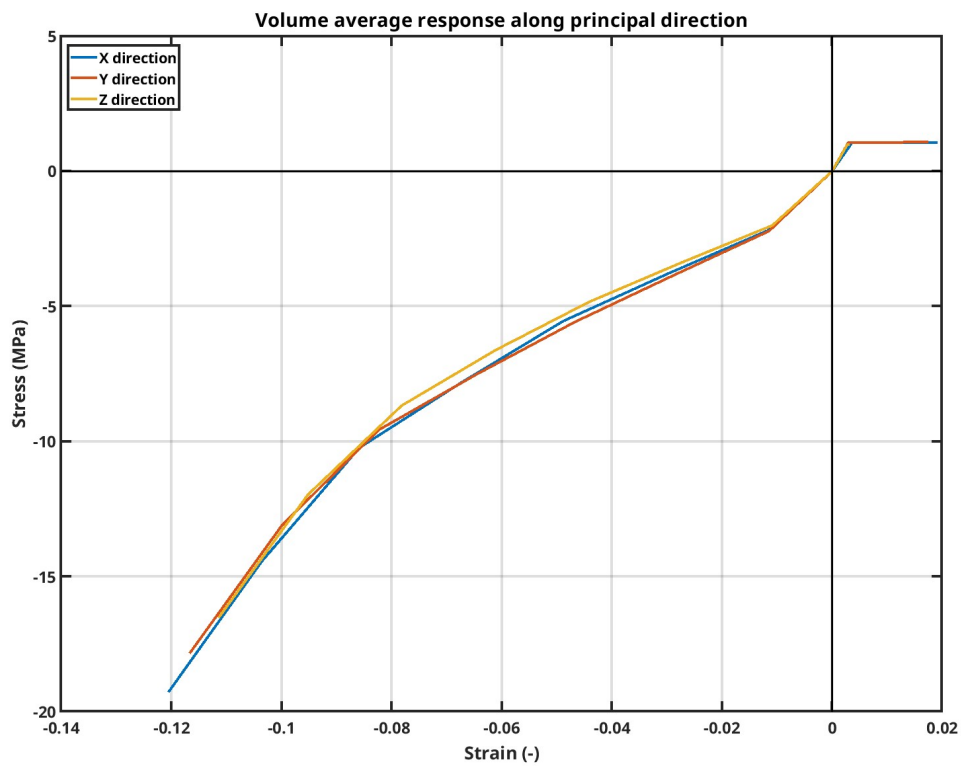


**Figure 4.11:** Response of the RVE along normal directions.

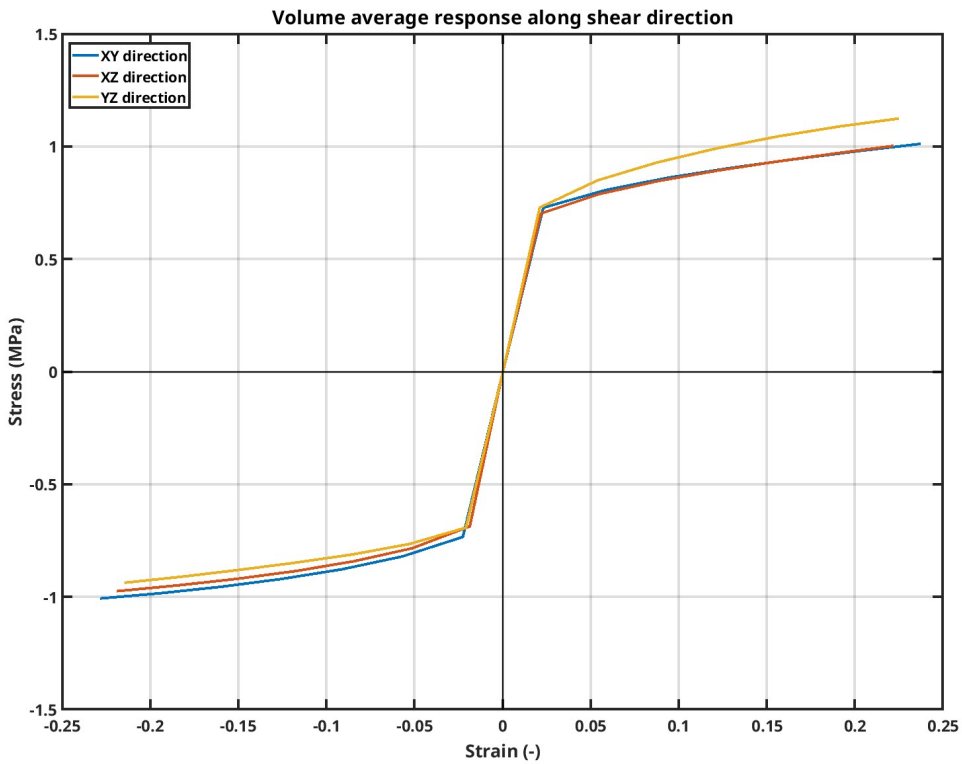


**Figure 4.12:** Response of the RVE along shear directions.

The characterized response curves were employed as test data to calibrate the homogenized material model. To facilitate the calibration process, the RVE was assumed to exhibit isotropic behavior. Under this assumption, the response curves in the normal and shear directions were averaged separately, yielding representative curves for each mode of deformation. Figure 4.13 illustrates the averaged test data along with the corresponding calibrated response of the homogenized material model. The accuracy of the calibration is determined using root square error (RSE) as the error measure. The error between the test data and the calibrated model response is quantified in Table 4.5. The resulting calibrated material parameters are listed in Table 4.6 and calibrated hardening curve is shown in the Figure 4.14.

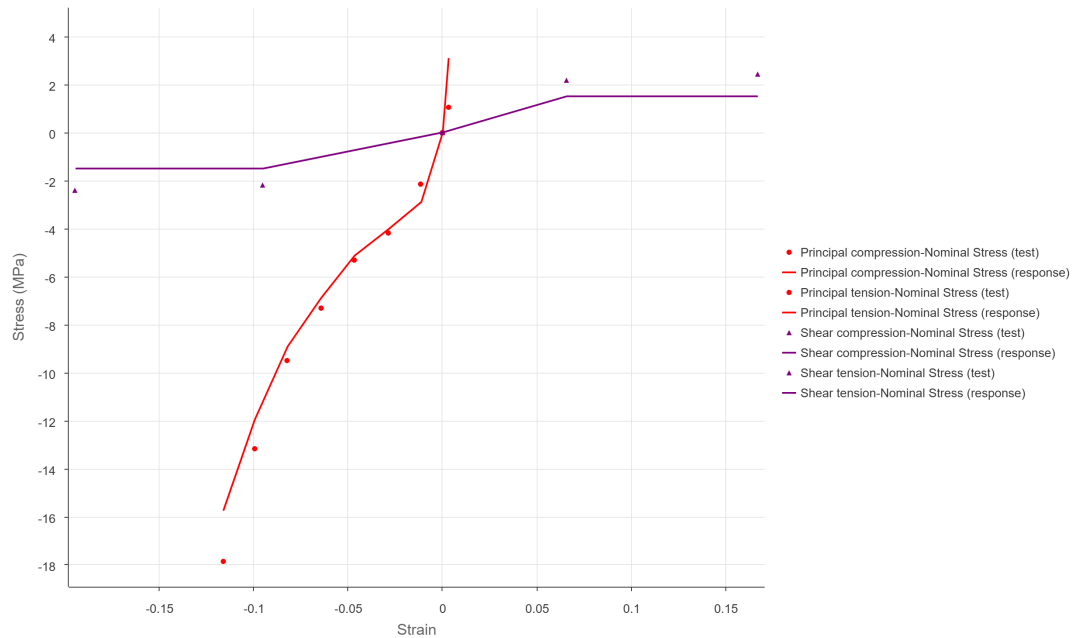


**Figure 4.13:** Calibrated curve and the test data points considering the isotropic response.

Loading direction	Root square error
Tension along normal direction	0.02
Compression along normal direction	1.994
Tension along shear direction	0.082
Compression along shear direction	0.08

**Table 4.5:** Error between the test data point and the calibrated curve.

Parameter	Magnitude
Young's Modulus (GPa)	0.988
Poisson's ratio	0.01
Compression stress ratio	1
Hydrostatic stress ratio	2.8

**Table 4.6:** Calibrated homogenized response of the negative electrode microscale RVE.

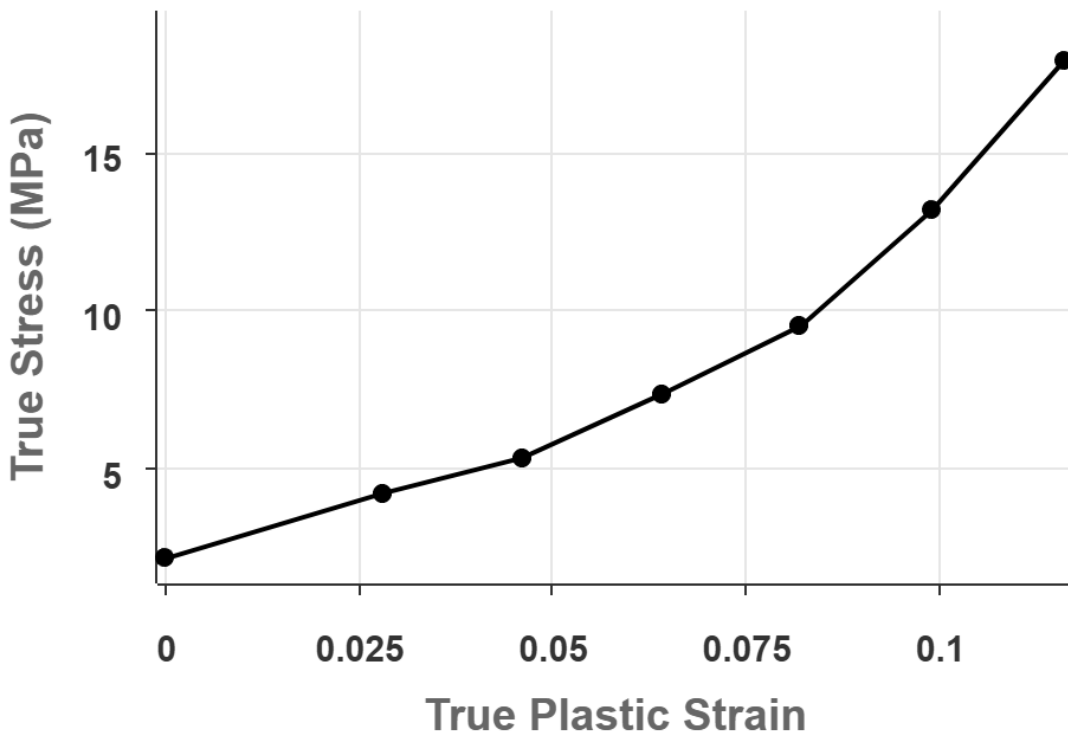


**Figure 4.14:** Calibrated hardening curve.

**Positive electrode RVE:**

Similarly, the homogenized response for the positive electrode was also characterized. Figure 4.15 and Figure 4.16 shows the obtained responses along the normal and shear directions.

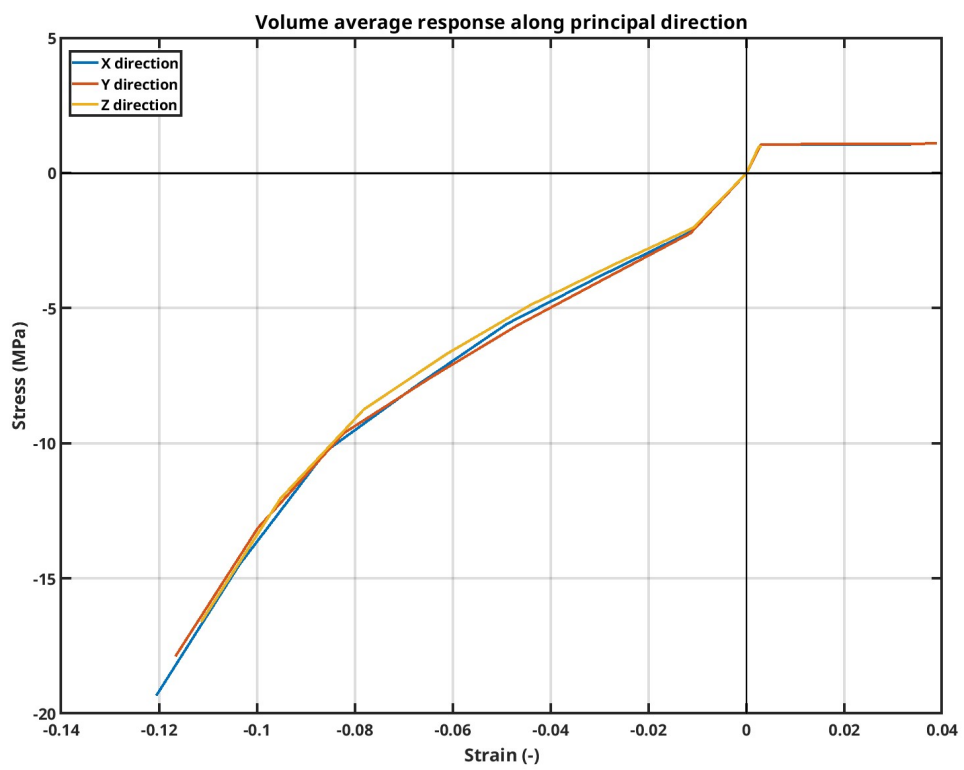


**Figure 4.15:** Response of the RVE along normal directions.

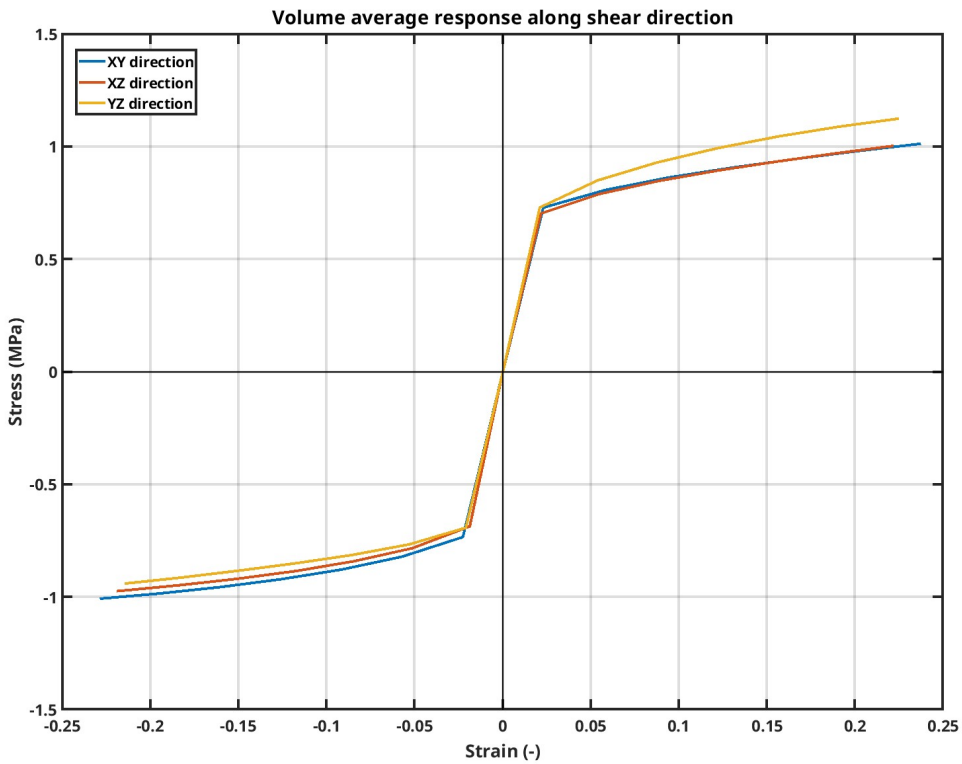


**Figure 4.16:** Response of the RVE along shear directions.

Under the assumption of isotropy, the response data were averaged separately in the normal and shear directions. Figure 4.17 illustrates the calibrated response curve alongside the corresponding averaged test data points. RSE was also used to measure the accuracy of the calibration. The corresponding error between the test data and the calibrated curve is summarized in Table 4.7. The calibrated material parameters are listed in the Table 4.8 and Figure 4.18 shows the calibrated hardening curve.

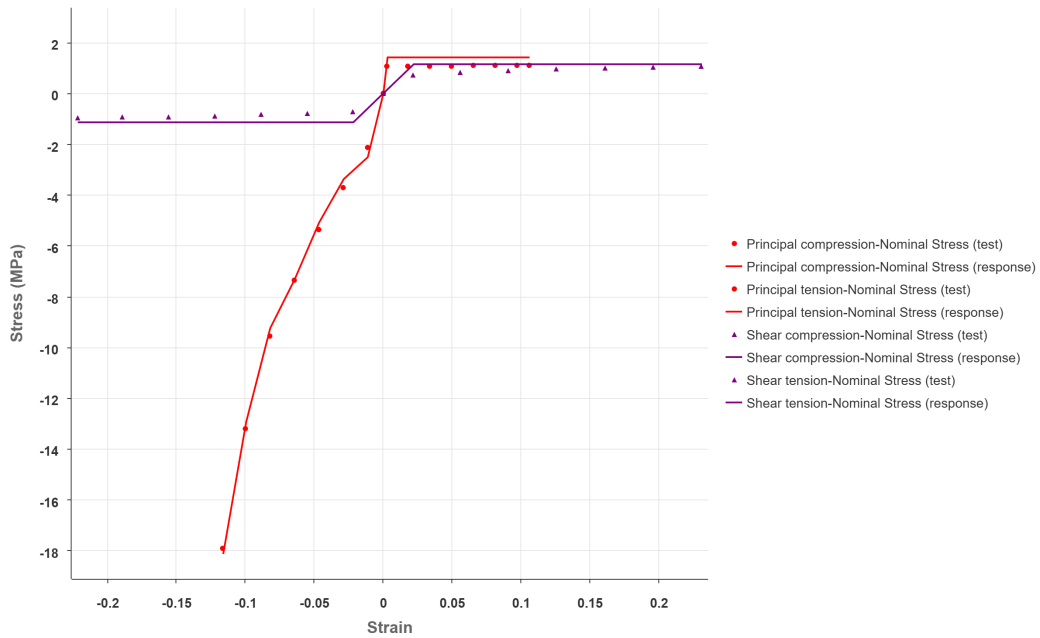


**Figure 4.17:** Calibrated curve and the test data points considering the isotropic response.

Loading direction	Root square error
Tension along normal direction	0.005
Compression along normal direction	0.085
Tension along shear direction	0.113
Compression along shear direction	0.077

**Table 4.7:** Error between the test data point and the calibrated curve.

Parameter	Magnitude
Young's Modulus (GPa)	0.988
Poisson's ratio	0.01
Compression stress ratio	1
Hydrostatic stress ratio	0.5

**Table 4.8:** Calibrated homogenized response of the positive electrode microscale RVE.

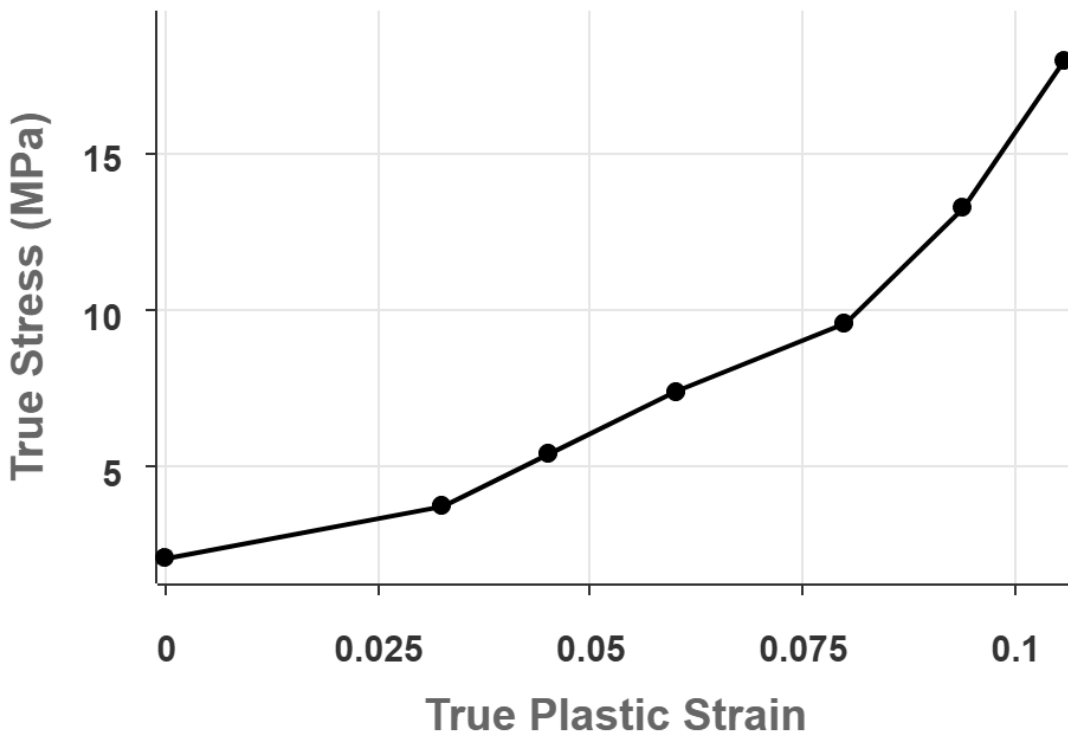
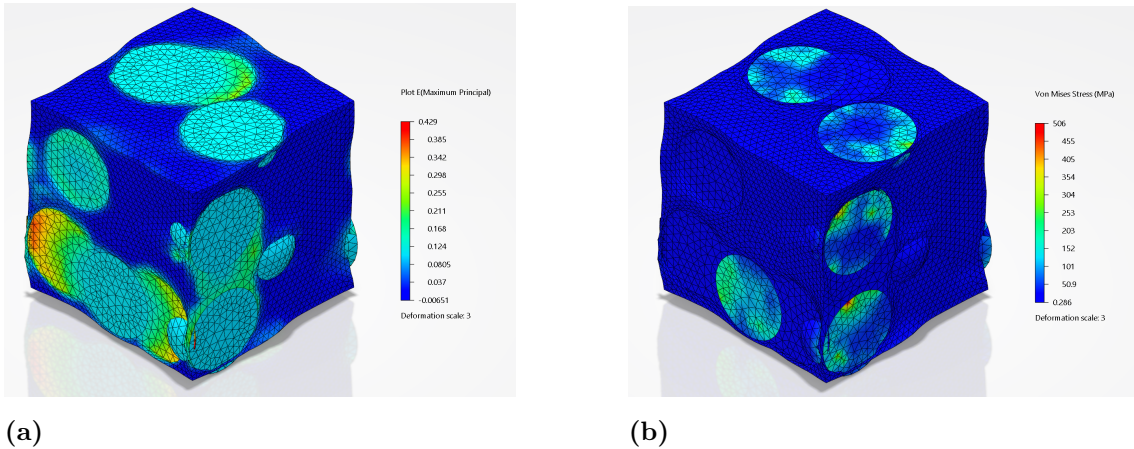


Figure 4.18: Calibrated hardening curve.

#### 4.1.2.2 Load case 2: Effective response due to lithiation

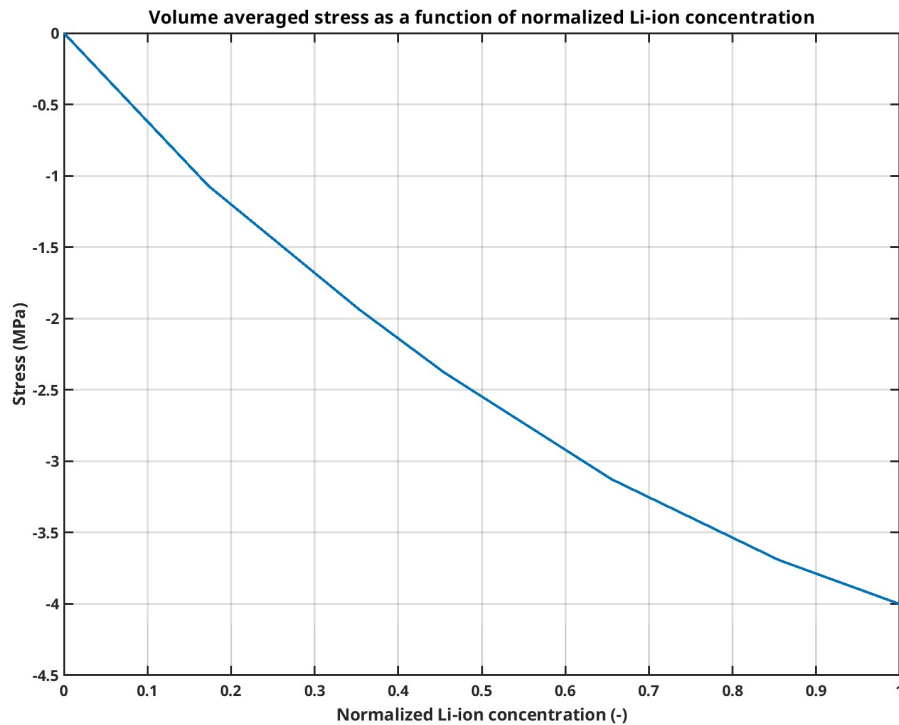
**Swelling of negative electrode:** Due to increase in lithium-ion concentration, the graphite inclusions undergo swelling. However, the surrounding matrix constrains this swelling, preventing it from occurring in a stress-free manner. As a result, internal stresses develop and the overall RVE deforms. Figure 4.19a illustrates the resulting distribution of maximum principal strain within the RVE, while Figure 4.19b shows the corresponding Von-mises stress distribution induced by the swelling of the inclusions.



**Figure 4.19:** Contour plot illustrating the a) Maximum strain distribution in the RVE, b) Von-Mises Stress distribution in the RVE due to the swelling of the graphite inclusions.

It can be observed from the contour plots that the von Mises stresses are lower, while the maximum principal strains are higher compared to the linear elastic case. This behavior is attributed to the lower stiffness of the crushable foam material relative to the linear elastic model, allowing it to accommodate a greater degree of swelling.

The response of the RVE due to the change in the lithium ion concentration is plotted in the Figure 4.20.



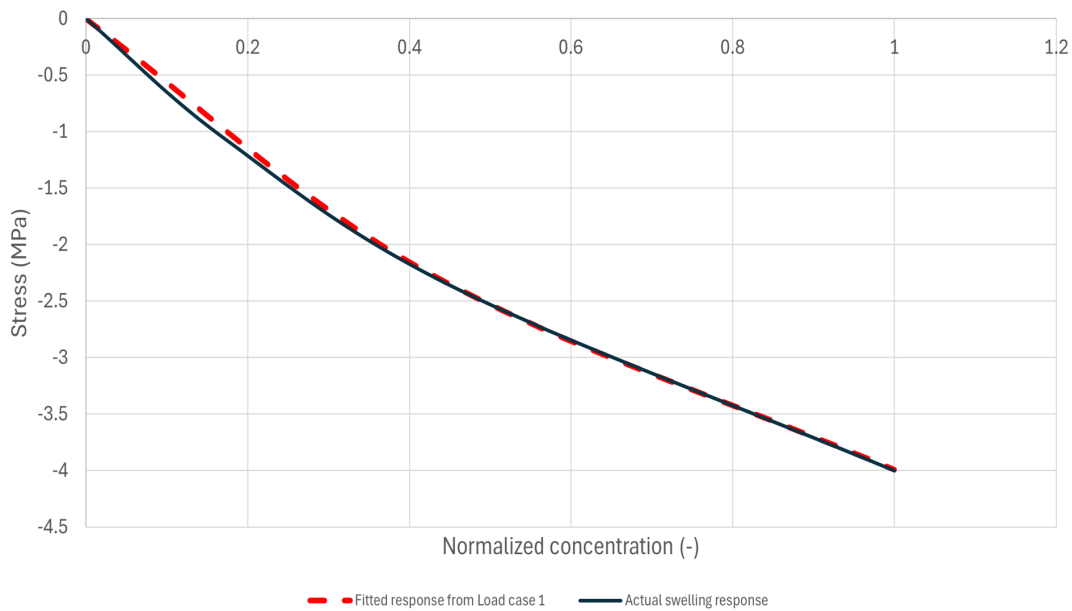
**Figure 4.20:** Volume averaged stress as a function of normalized Li-ion concentration.

Figure 4.20 shows that the swelling of the inclusions induces compressive stress in the matrix, similar to the behavior observed in the linear elastic case. However, in this case, the compressive stress slightly exceeds the elastic threshold and enters the nonlinear regime.

#### Calculation of effective swelling coefficient of the negative electrode

According to the strategy outlined in Subsection 3.3, the homogenized response of the RVE is first characterized using Load Case 1 by applying a macroscopic strain of 10%. To simulate the effect of inclusion swelling under zero applied macroscopic strain, this external strain is removed and replaced by an imposed strain of magnitude  $\Omega^{el} \Delta c_{s,p}^{avg}$ , where  $c_{s,p}^{avg} = 1$  corresponds to the fully lithiated state. The value of  $\Omega^{el}$  is then iteratively adjusted until the predicted response matches that obtained from Load Case 2.

Using this strategy, an effective swelling coefficient of  $\Omega^{el} = 0.027$  was found to yield a calibrated response from Load Case 1 that closely matches the response obtained from Load Case 2. Figure 4.21 illustrates the comparison between the fitted and actual response curves.



**Figure 4.21:** Figure showing the actual response curve and the fitted response curve for  $\Omega^{el} = 0.027$ .

#### Shrinking of positive electrode:

As the lithium-ion concentration decreases, the  $\text{LiMn}_2\text{O}_4$  inclusions undergo shrinkage. However, since these inclusions are embedded within the matrix, the surrounding matrix resists their contraction, resulting in the development of internal stresses. Figure 4.22a illustrates the distribution of maximum principal strain within the RVE, while Figure 4.22b presents the corresponding Von-mises stress distribution caused by the shrinkage of the inclusions.

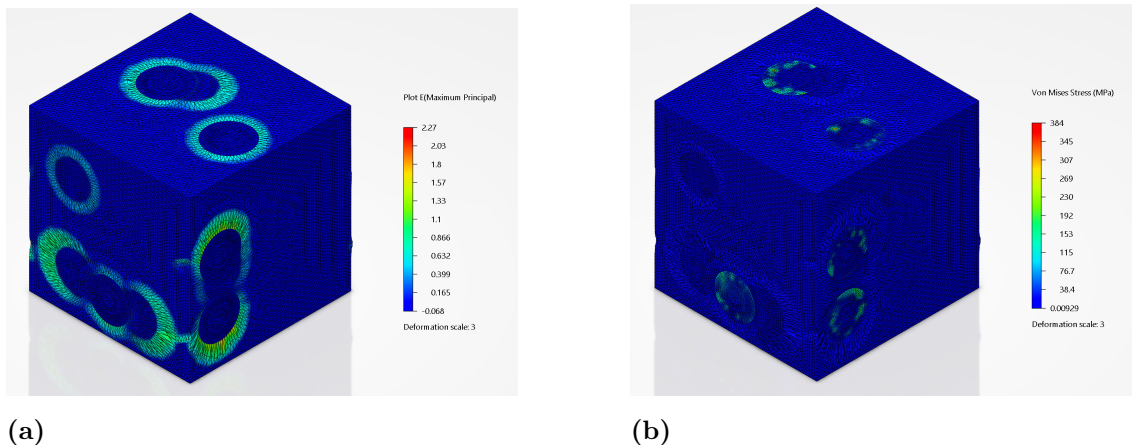


**Figure 4.22:** Contour plot illustrating the a) Maximum strain distribution in the RVE, b) Von-mises Stress distribution in the RVE due to the shrinking of the  $\text{LiMn}_2\text{O}_4$  inclusions.

It can be observed from the contour plots that the von Mises stresses are lower, while the maximum principal strains are higher compared to the linear elastic case.

This behavior arises because the crushable foam material offers minimal resistance to the shrinkage of the inclusions.

The response of the RVE due to the change in the lithium ion concentration is plotted in the Figure 4.23.

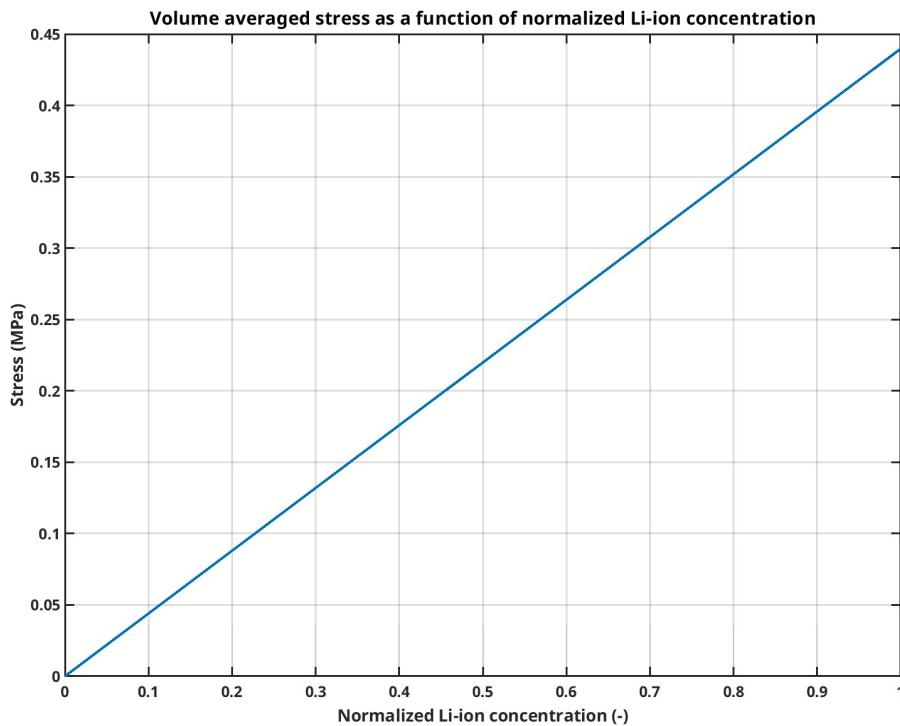


**Figure 4.23:** Volume averaged stress as a function of normalized Li-ion concentration.

Figure 4.23 shows that the shrinkage of the inclusions induces tensile stresses within the RVE. However, the magnitude of the generated tensile stress remains below the tensile cutoff limit. As a result, the material response remains within the linear elastic regime.

#### Calculation of effective shrinking coefficient of the positive electrode

As outlined in the above negative electrode case, for calculating the effective swelling coefficient, the homogenized response of the RVE is first characterized using Load Case 1 by applying a macroscopic strain of 10%. To simulate the effect of inclusion shrinking under zero applied macroscopic strain, this external strain is removed and replaced by an imposed strain of magnitude  $\Omega^{el} \Delta c_{s,p}^{avg}$ , where  $c_{s,p}^{avg} = -1$  corresponds to the fully delithiated state. The value of  $\Omega^{el}$  is then iteratively adjusted until the predicted response matches that obtained from Load Case 2.

Using this strategy, an effective swelling coefficient of  $\Omega^{el} = 0.00125$  was found to yield a calibrated response from Load Case 1 that closely matches the response

obtained from Load Case 2. Figure 4.24 illustrates the comparison between the fitted and actual response curves.

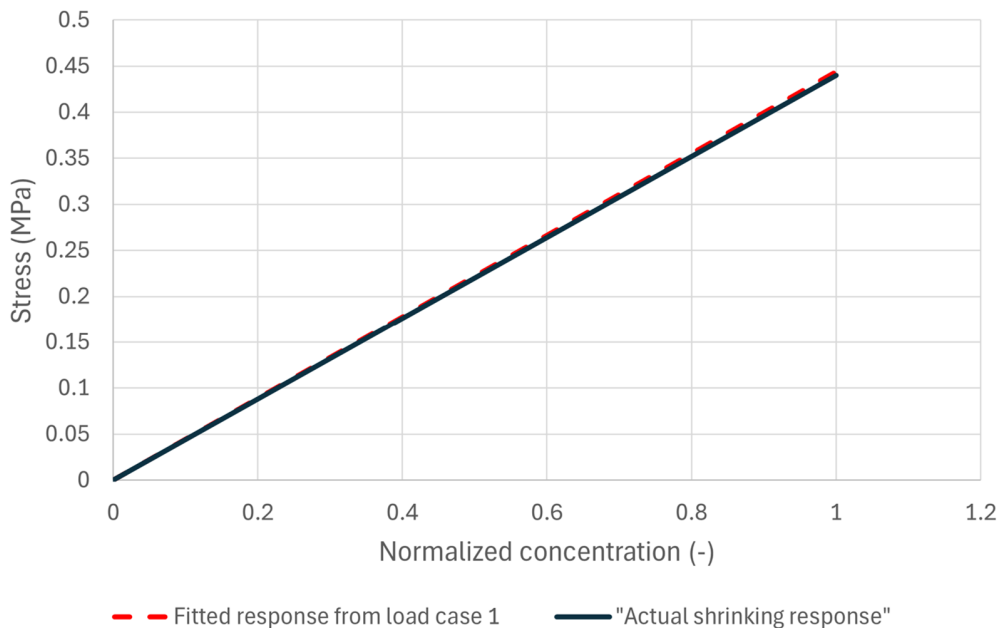


**Figure 4.24:** Figure showing the actual response curve and the fitted response curve for  $\Omega^{el} = 0.00125$ .

#### 4.1.3 Comparison between effective swelling coefficients computed from linear elastic and non-linear constitutive models

Electrode	Linear Elastic Model	Non-Linear Model
Negative Electrode	0.016	0.027
Positive Electrode	0.012	0.00125

**Table 4.9:** Comparison of effective swelling coefficients for linear elastic and non-linear material models.

Table 4.9 compares the effective swelling coefficients computed using both linear elastic and non-linear material models for the negative and positive electrodes. For the negative electrode, the effective swelling coefficient obtained using the non-linear material model is slightly higher than that from the linear elastic model. This increase is attributed to the lower stiffness of the crushable foam model, which allows for greater volumetric expansion of the inclusions, thereby resulting in a higher effective swelling response.

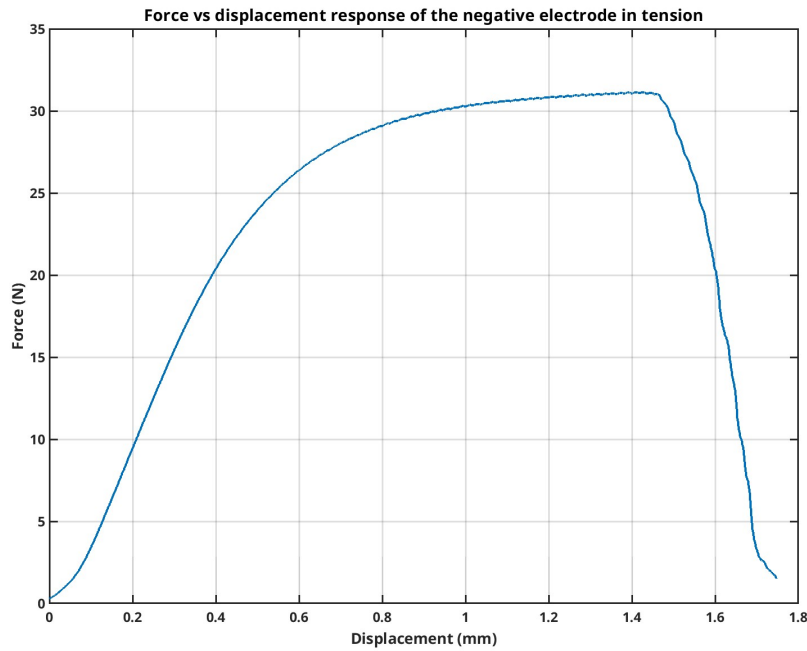
In contrast, for the positive electrode, the swelling coefficient obtained from the non-linear model is lower than that of the linear elastic case. This reduction arises

because the crushable foam offers less resistance to shrinkage of the inclusions, leading to a decreased effective swelling response.

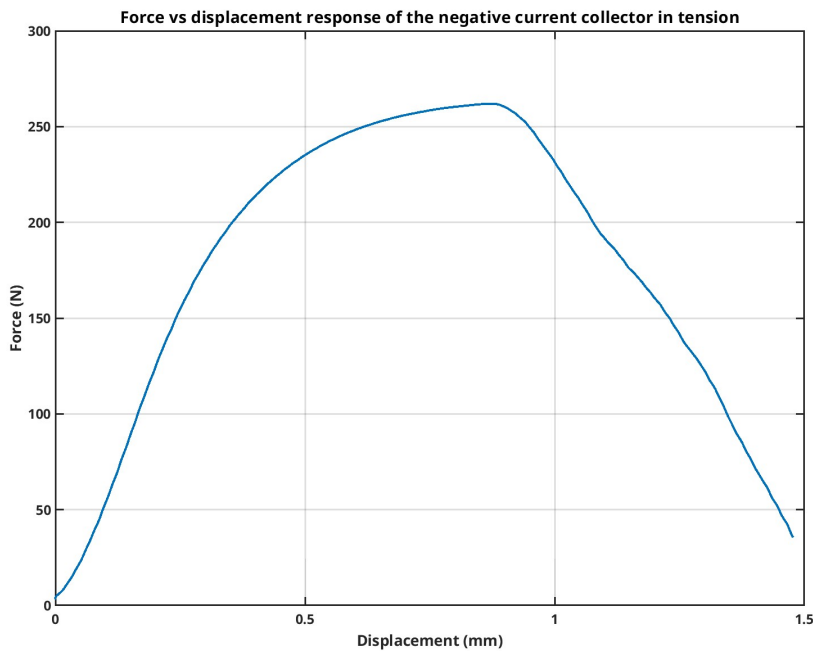
## 4.2 Mesoscale model

### 4.2.1 Material characterization: Tested response

Negative electrodes and the separator were tested uniaxially to characterize their response under tension. Figure 4.25a and 4.25b shows the resulting force vs displacement curves for negative current collector and negative electrode and Figure 4.26a and 4.26b shows the obtained force vs displacement curve of the separator along the  $0^\circ$  and  $90^\circ$  respectively for a loading rate of 20 mm/min.

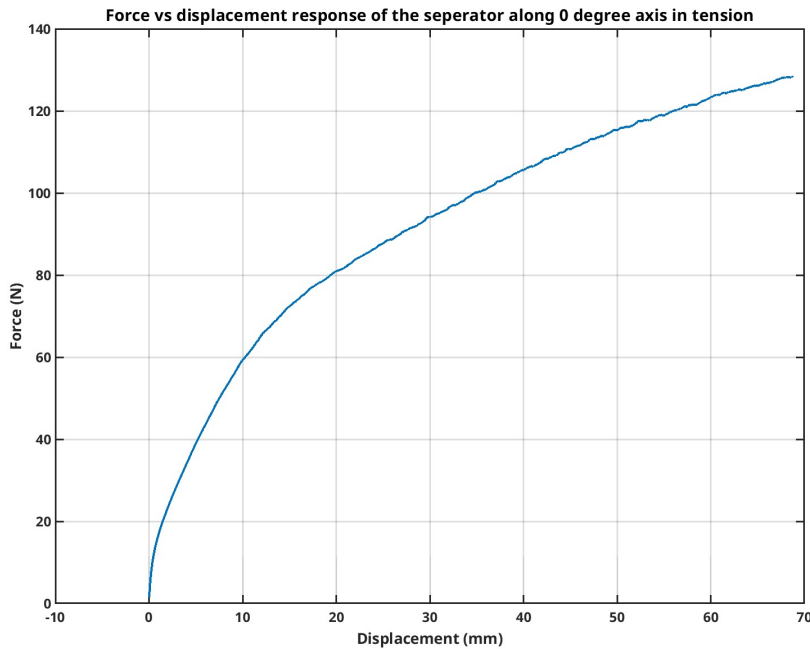


(a)

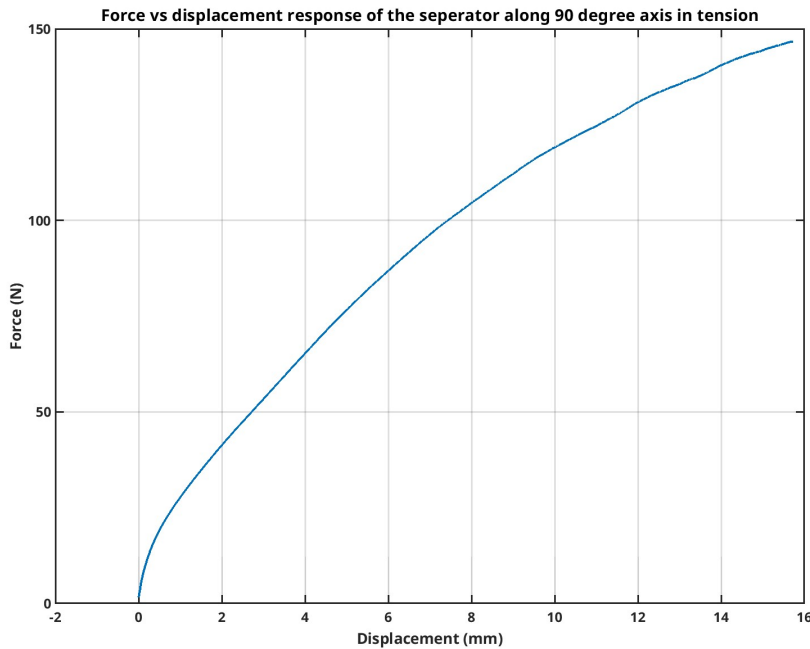


(b)

**Figure 4.25:** Force vs Displacement response of (a) negative electrode active material and (b) negative electrode current collector.



(a)



(b)

**Figure 4.26:** Force vs Displacement response of (a) separator along  $0^\circ$  and (b) separator along  $90^\circ$ .

Due to the very thin nature of the separator specimen, to effectively perform compression test, more number of specimens are required. Due to time constraints in preparing the test specimen of separators for the compression load case, only the

negative electrodes were evaluated. The resulting Force vs displacement curves for 2 mm/min loading rate for the negative electrode is shown in the Figure 4.27.

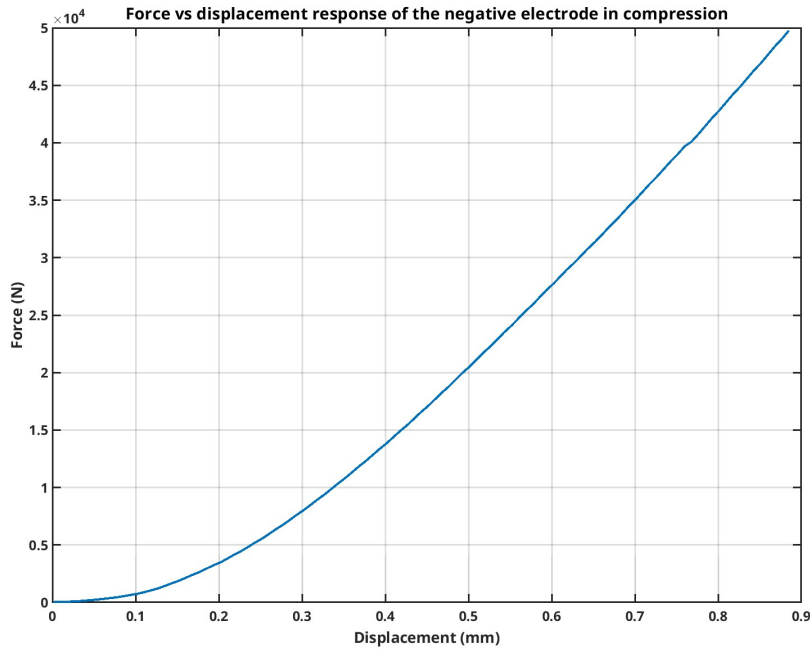


**Figure 4.27:** Force vs Displacement response of the negative electrode in compression.

It has to noted here that the curve presented in the Figure 4.27 is the combined response of the current collector and the electrode material.

#### 4.2.2 Material calibration

The test curves used for the material calibration are adopted from the literature [21]. As mentioned, the electrodes and separator responses are calibrated using crushable foam material model and the current collectors were modeled as elasto-plastic material model. The calibrated response along with the test data for each component are shown in the Figure B.1 to Figure 4.32. The Root square error between the calibrated and the test curve are depicted in the Table 4.10. The calibrated material parameters are attached in Appendix B.

Layer	Root square error
Negative active material	0.113
Negative current collector	0.002
Separator	0.013
Positive active material	0.223
Positive current collector	0.002

**Table 4.10:** Table depicting the root square error between the calibrated and the test curves.

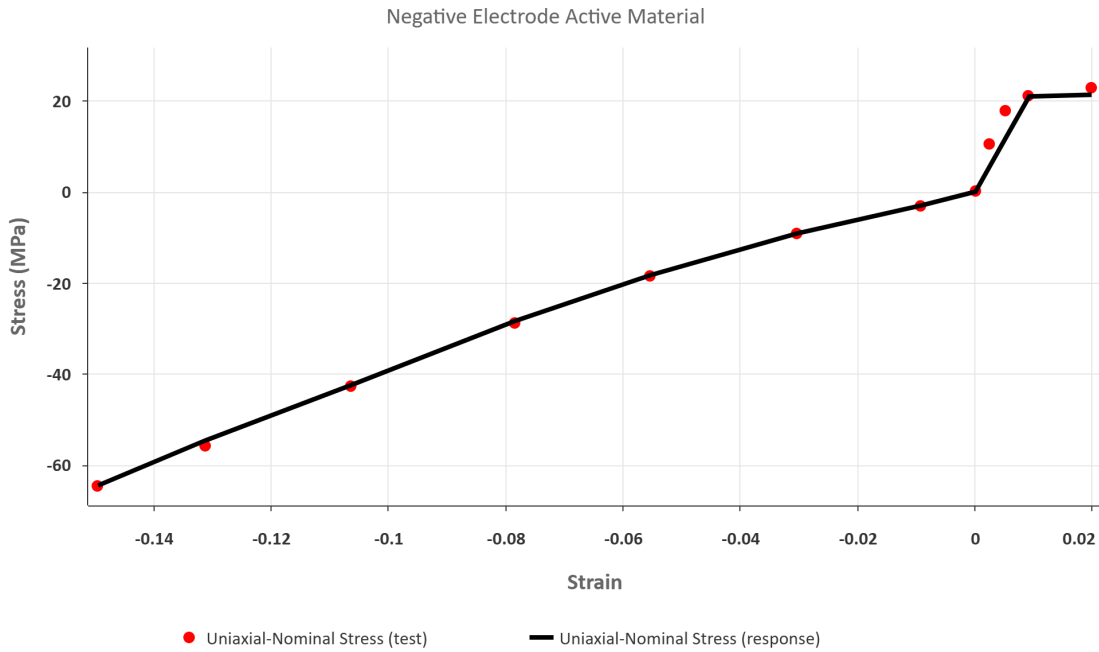


**Figure 4.28:** Plot illustrating the test data points and the calibrated response of the negative active material.

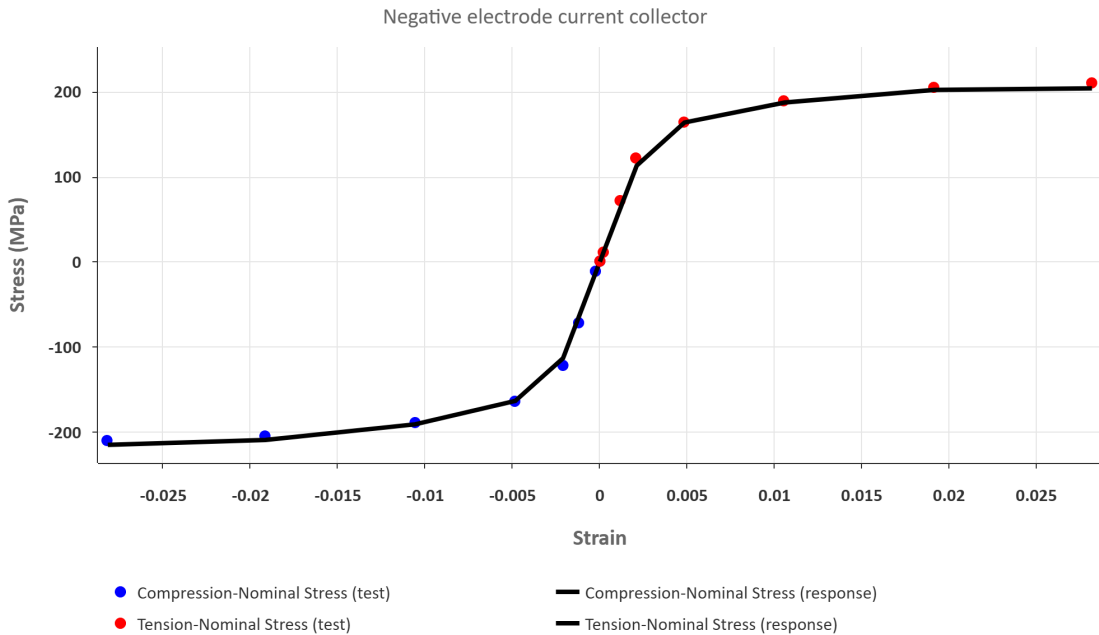


**Figure 4.29:** Plot illustrating the test data points and the calibrated response of the negative current collector.

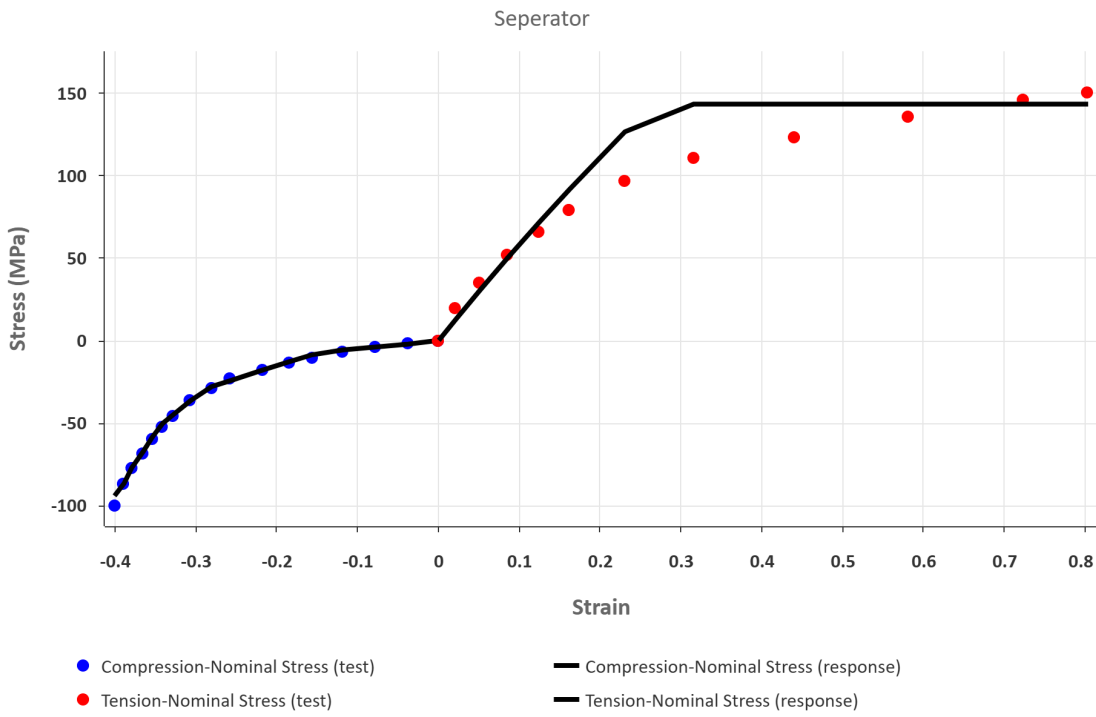


**Figure 4.30:** Plot illustrating the test data points and the calibrated response of the separator.

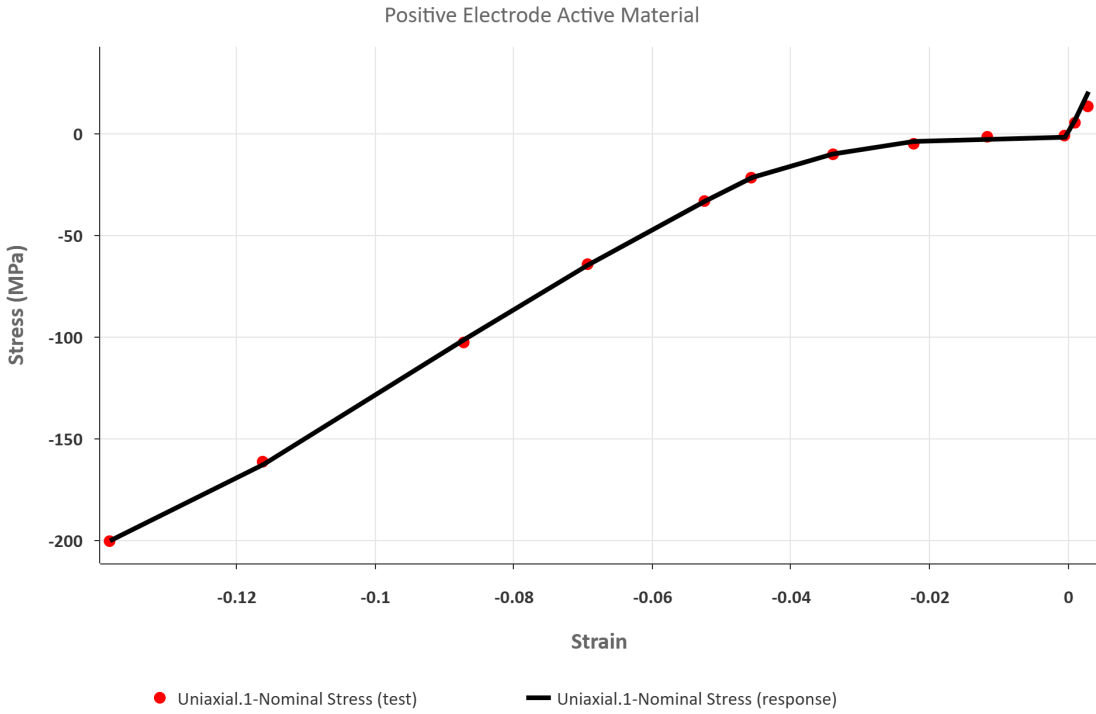


**Figure 4.31:** Plot illustrating the test data points and the calibrated response of the positive active material.

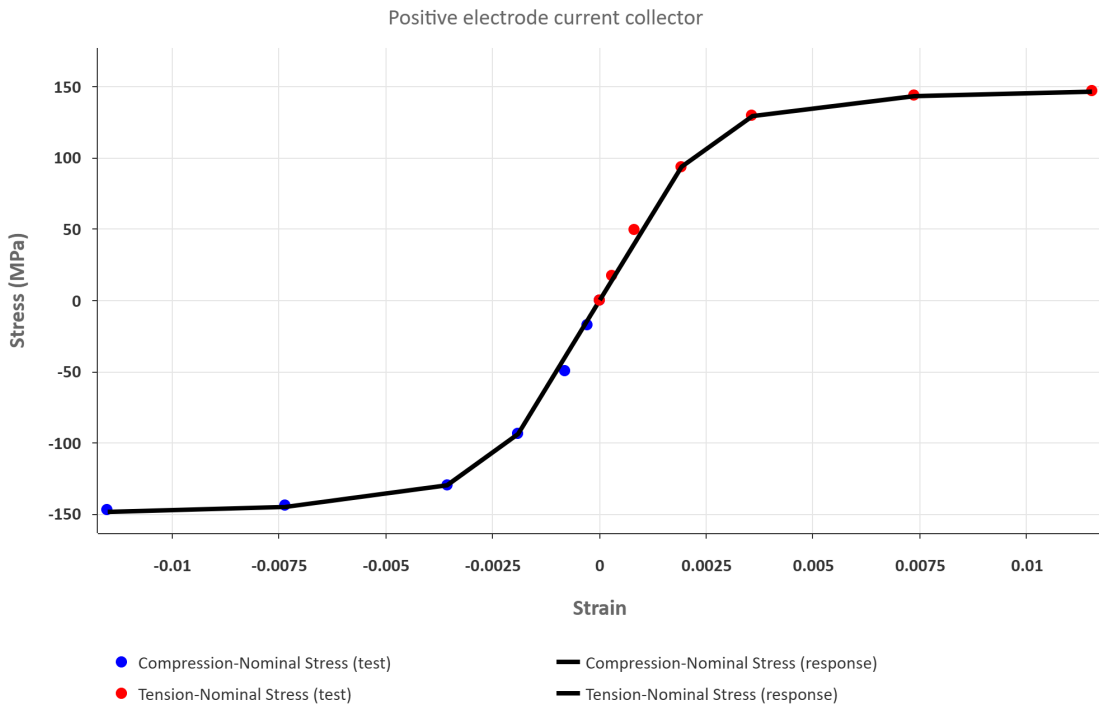


**Figure 4.32:** Plot illustrating the test data points and the calibrated response of the positive current collector.

### 4.2.3 Coupled Electrochemical-mechanical simulation

#### 4.2.3.1 Mechanical response under periodic boundary condition

As detailed in subsection 2.2.2, the key electrochemical variables like solid-phase potential ( $\phi_s$ ), electrolyte potential ( $\phi_e$ ), electrolyte concentration ( $c_e$ ), and solid-phase lithium concentration ( $c_s$ ) are computed using the DFN electrochemical model implemented within the 3DEXPERIENCE platform. Utilizing the specified periodic boundary conditions, initial conditions, and the galvanostatic load described in subsection 3.4, a coupled electrochemical-mechanical simulation is set up and executed. The simulation is initialized with a solid-phase potential  $\phi_s = 3$  V, corresponding to a state of charge (SOC) of 0, and proceeds until the terminal voltage reaches 4.1 V, representing a fully charged state (SOC = 1). The evolution of  $\phi_s$  over the course of the simulation is illustrated in Figure 4.33.

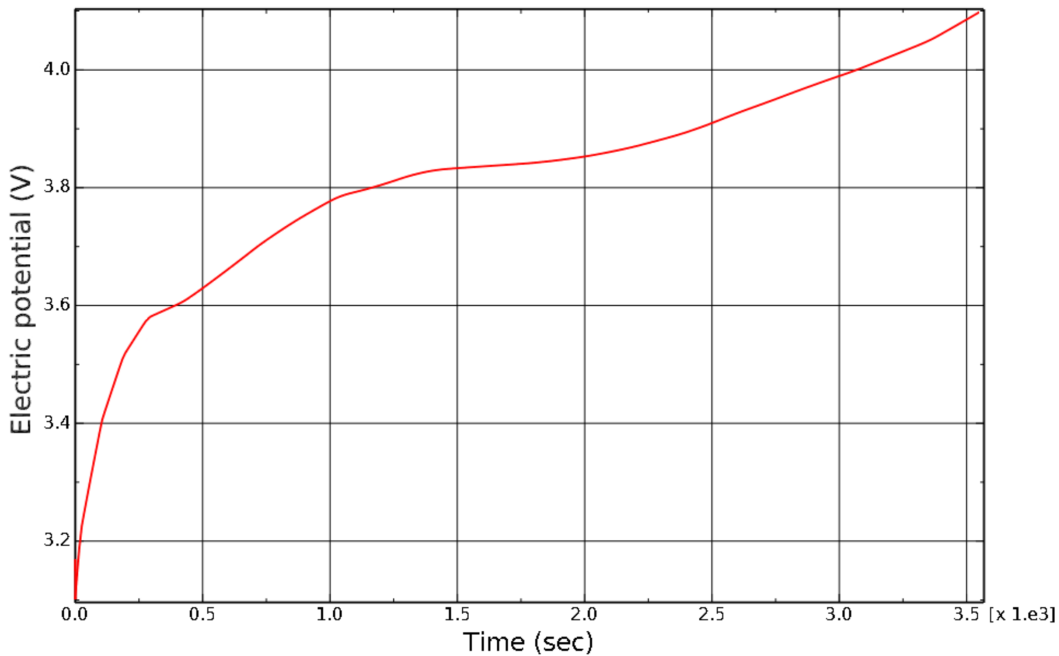


**Figure 4.33:** Evolution of  $\phi_s$  for a 1C charging rate.

As discussed in subsection 3.4, the simulation begins with a specified initial concentration of lithium ions in both the solid and electrolyte phases. When a constant current is applied (galvanostatic load), lithium ions begin to deintercalate from the positive electrode and enter the electrolyte. This causes a decrease in lithium concentration within the positive electrode, as shown in Figure 4.35. Correspondingly, an increase in lithium ion concentration is observed in the electrolyte near the positive electrode, particularly close to the current collector where the current is applied, as depicted in Figure 4.34.

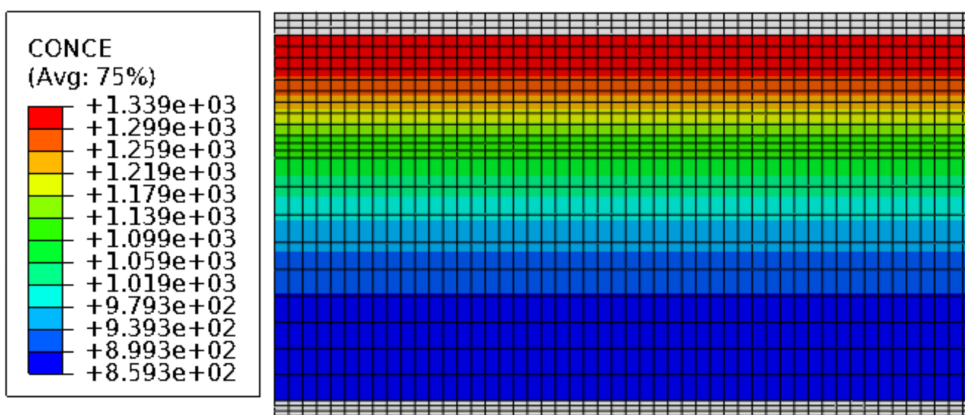


**Figure 4.34:** Contour plot illustrating the Li-ion concentration in the electrolyte at SOC=1.

At the negative electrode, the opposite process occurs. Lithium ions from the elec-

trolyte intercalate into the solid particles, resulting in a reduction in electrolyte-phase lithium concentration on that side, again observable in Figure 4.34. The lithium concentration within the negative electrode increases over time, as shown in Figure 4.35.

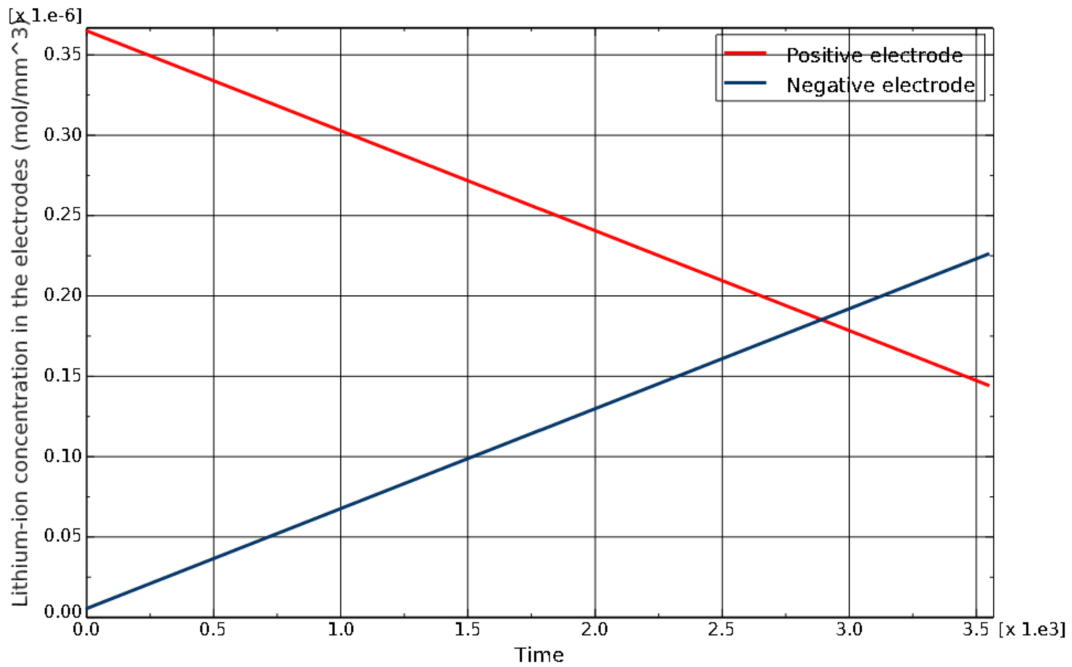


**Figure 4.35:** Li-ion concentration in the electrodes for 1C charging rate.

The extraction of lithium ions from the positive electrode results in volumetric shrinkage of the electrode material, whereas the intercalation of lithium ions into the negative electrode leads to swelling. These mechanical deformations are driven by the intercalation and deintercalation processes occurring during cell operation. Due to the applied periodic boundary condition, the mesoscale stack is allowed to deform freely in both inplane and in the out of plane directions. Figure 4.36 depicts the induced strains in the stack due to lithium intercalation and deintercalation and Figure 4.37 illustrates the change in the dimensions of the stack along the three principal directions.

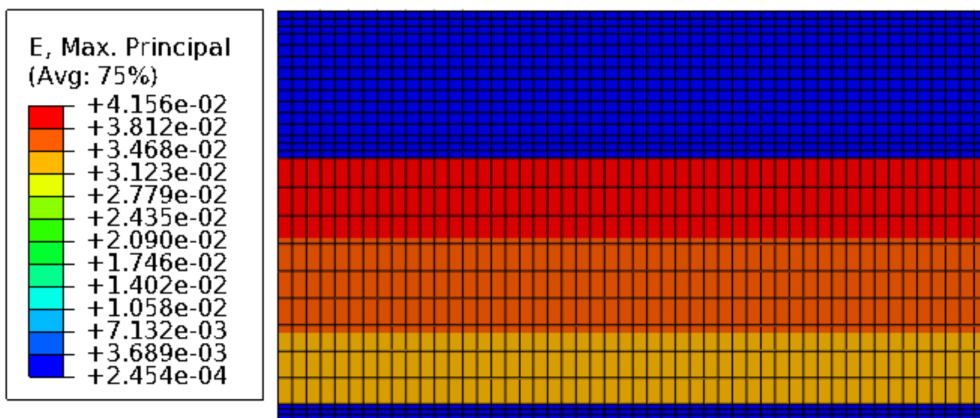


**Figure 4.36:** Contour plot depicting the lithiation induced strain in the thickness direction.

From Figure 4.36 it can be seen that the maximum strain is induced in the negative electrode side particularly close to the separator. This is because, the lithium ions chooses the shortest path to intercalate. When all the potential intercalation sites are filled close to the separator, the intercalation progresses towards the negative current collector.

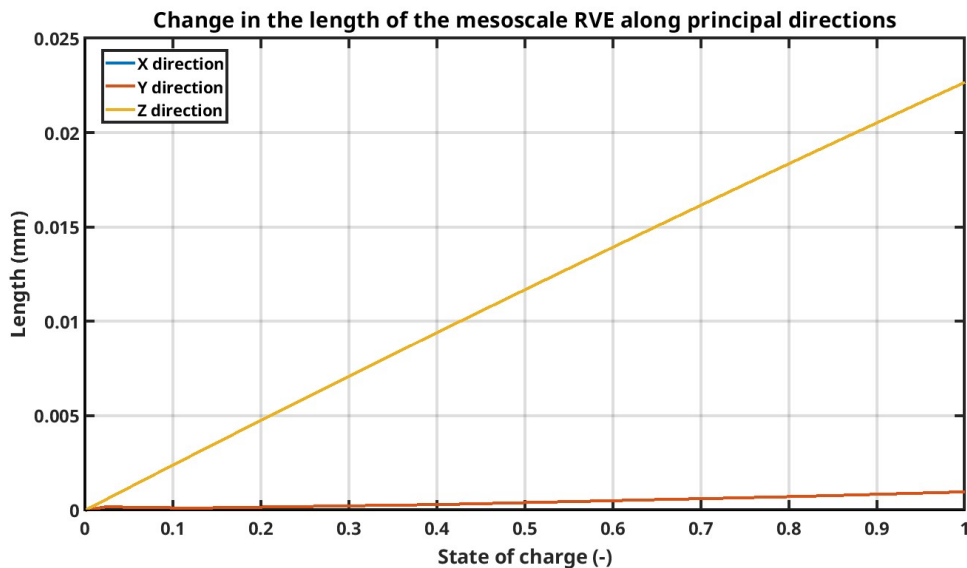


**Figure 4.37:** Plot illustrating the change in the dimension of the mesoscale stack along the three principal directions.

From Figure 4.37, it can be observed that the change in the dimensions of the stack in the principal Z direction i.e. the out of plane direction supersedes the inplane changes. Along the plane of the electrodes, the deformation is uniform.

The resulting effective volumetric strain in the stack is plotted in the Figure 4.38.

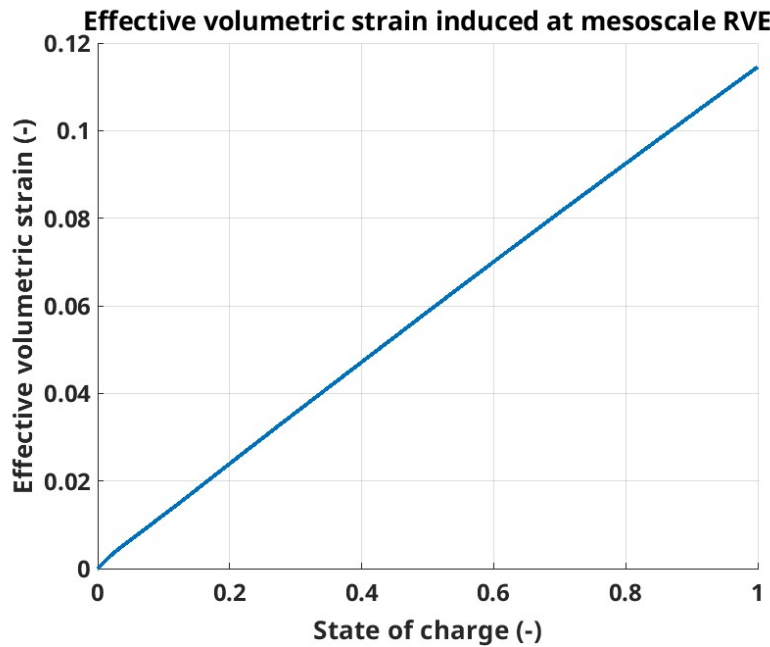


**Figure 4.38:** Effective strain induced in the mesoscale RVE due to lithiation.

The volume change of the electrodes during charging is evaluated as described in subsection 3.4. Figure 4.39 illustrates the evolution of volume in both the positive and negative electrodes. As observed, the swelling of the negative electrode exceeds the shrinkage of the positive electrode. Consequently, the net mechanical response of the mesoscale electrode stack during charging is an overall expansion. Figure 4.40 shows the effective expansion of the stack.

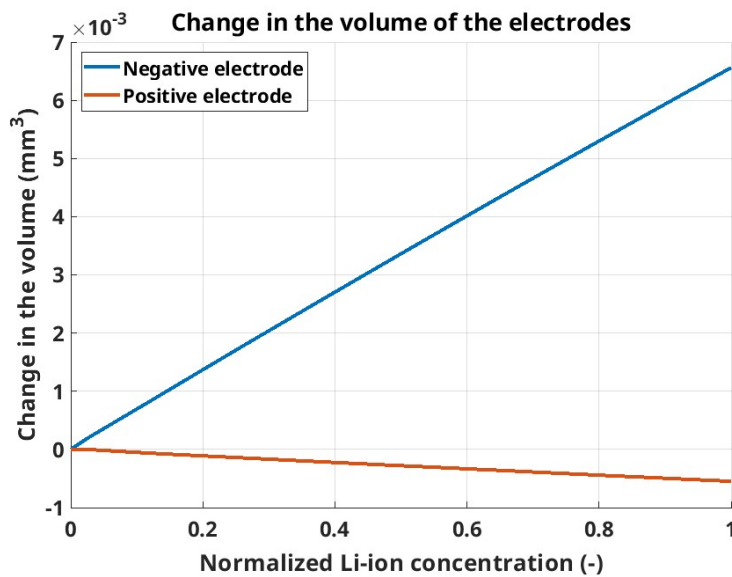


**Figure 4.39:** Change in the volume of the electrodes due to lithiation and delithiation.

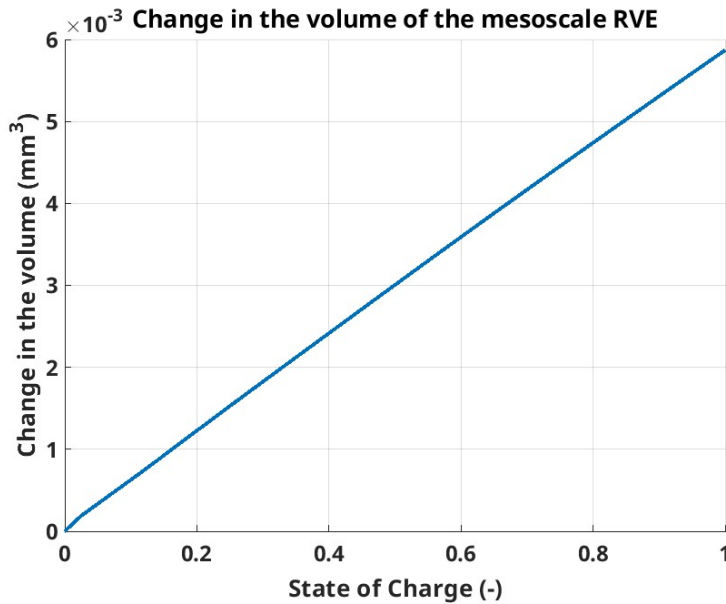


**Figure 4.40:** Effective change in the volume of the mesoscale stack.

#### 4.2.3.2 Mechanical response under symmetry boundary condition

Based on the observations from Figure 4.37, it can be concluded that out-of-plane deformations are more significant than in-plane deformations. As a result, symmetry boundary conditions were applied to constrain the in-plane deformations, and the problem was re-solved under these conditions. The evolution of the solid-phase potential,  $\phi_s$ , throughout the simulation is shown in Figure 4.41.

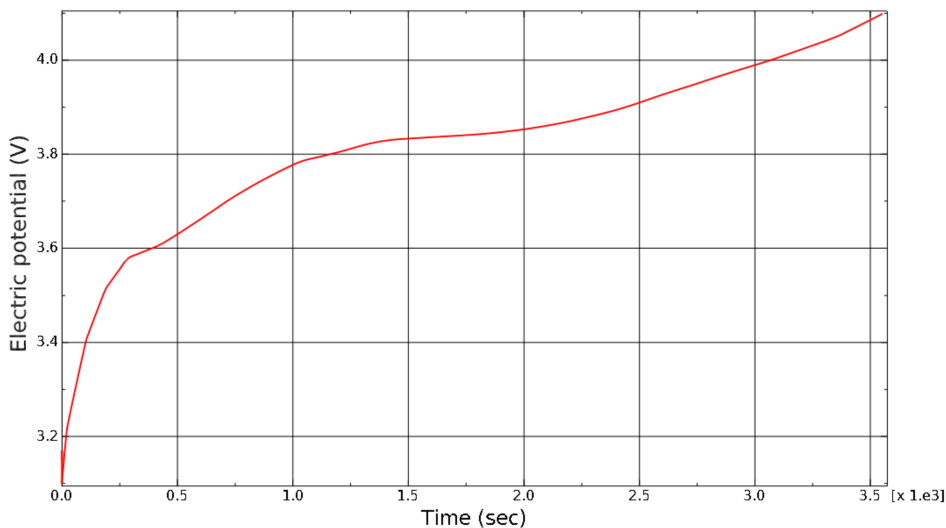


**Figure 4.41:** Evolution of  $\phi_s$  for a 1C charging rate.

The evolution of the electrochemical variables like  $c_e$  and  $c_s$  are shown in the Figure 4.42 and 4.43 respectively.

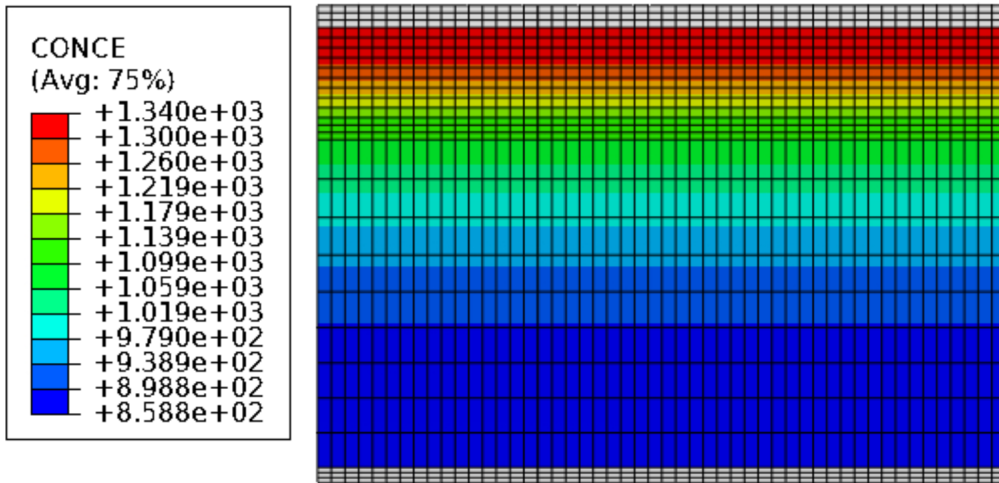


**Figure 4.42:** Contour plot illustrating the Li-ion concentration in the electrolyte at SOC=1.

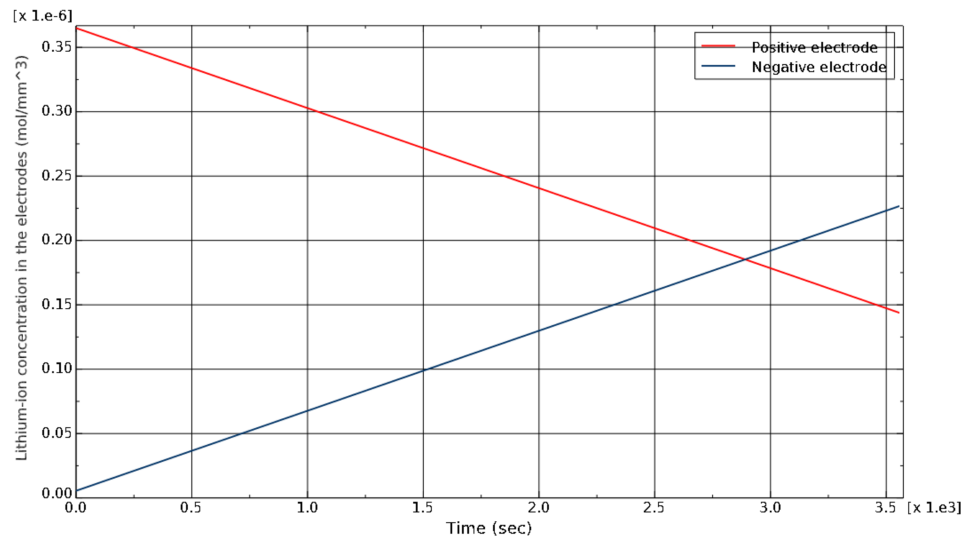


**Figure 4.43:** Li-ion concentration in the electrodes for 1C charging rate.

The strain resulting from lithiation and delithiation is illustrated in Figure 4.44. In this case, the maximum induced strain exceeds that observed under periodic boundary conditions. This increase in strain is attributed to the additional mechanical constraints imposed by the symmetry boundary conditions. The dimensional changes of the stack during charging are also shown in the Figure 4.45. Due to the applied constraints, the deformation in the in-plane directions is negligible.

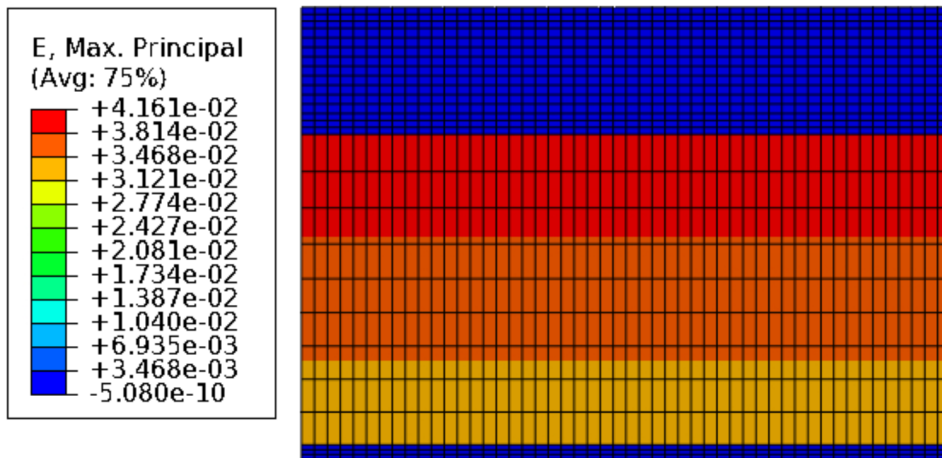


**Figure 4.44:** Contour plot depicting the lithiation induced strain in the thickness direction.

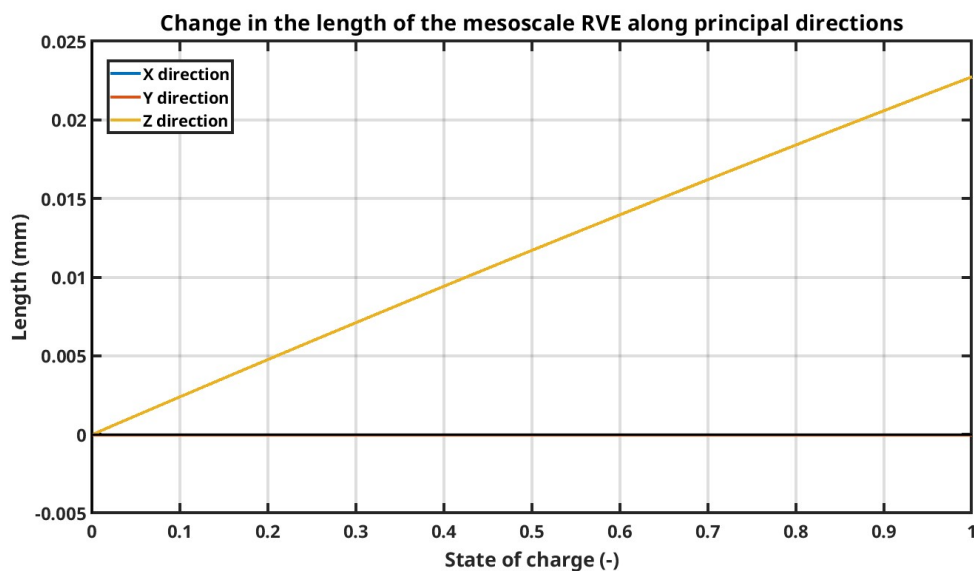


**Figure 4.45:** Plot illustrating the change in the dimension of the mesoscale stack along the three principal directions.

The effective volumetric strain induced in the stack is plotted in the Figure 4.46

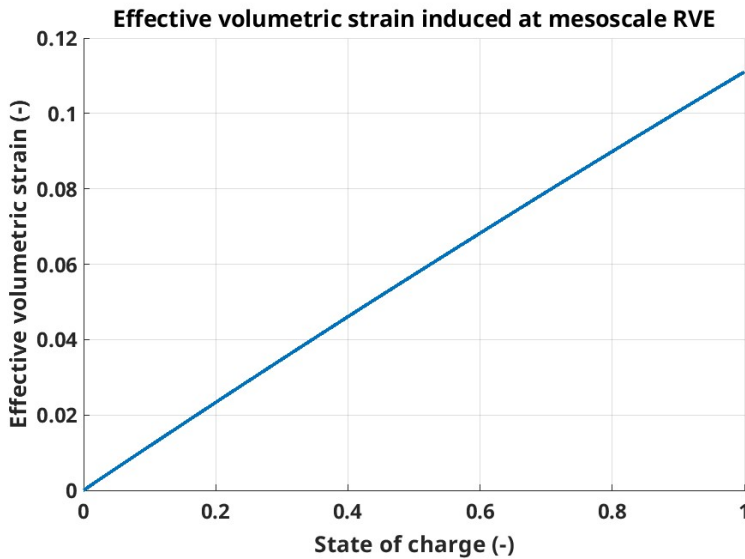


**Figure 4.46:** Effective strain induced in the mesoscale RVE due to lithiation.

Figure 4.47 illustrates the evolution of volume in both the positive and negative electrodes. As observed, the swelling of the negative electrode exceeds the shrinkage of the positive electrode. Consequently, the net mechanical response of the mesoscale electrode stack during charging is an overall expansion. Figure 4.48 shows the effective expansion of the stack.

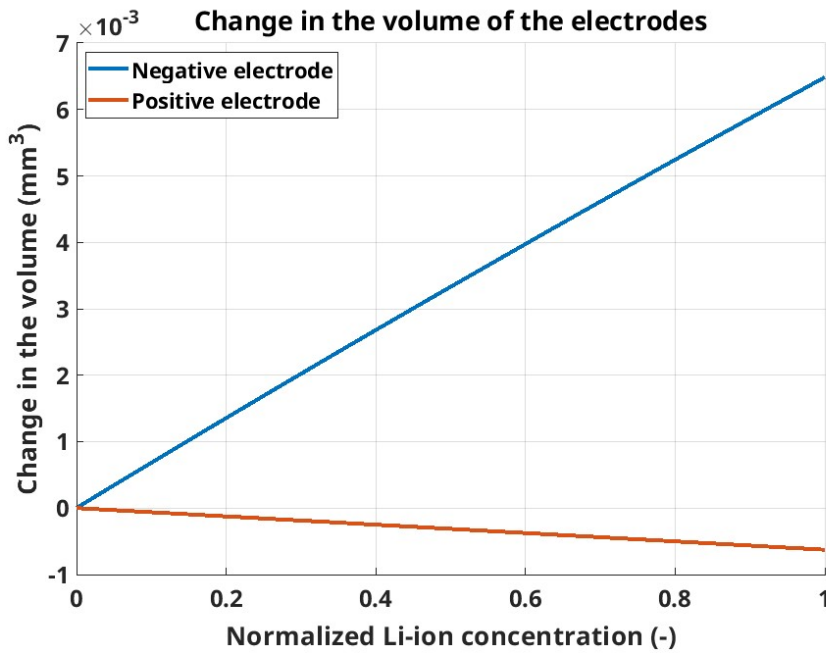


**Figure 4.47:** Change in the volume of the electrodes due to lithiation and delithiation.

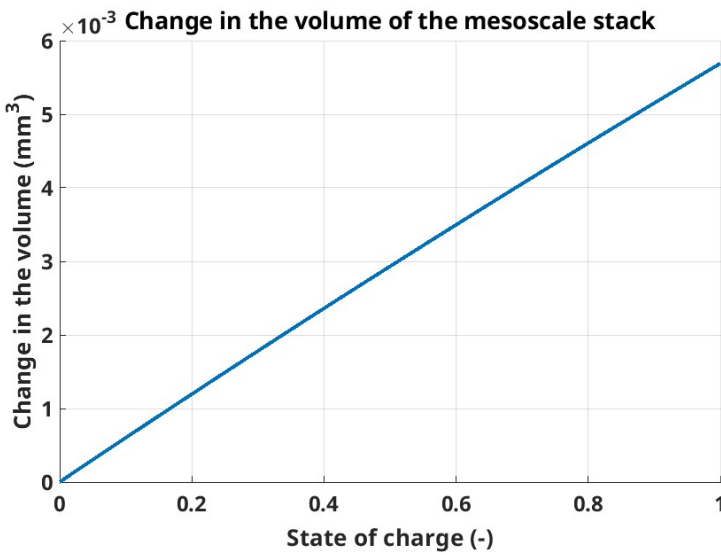


**Figure 4.48:** Effective change in the volume of the mesoscale stack.

#### 4.2.3.3 Swelling effects comparison between periodic and symmetry boundary condition

In this study, two distinct boundary conditions were investigated to assess their impact on the volumetric expansion of both the electrodes and the overall stack. The resulting volumetric expansion under each condition is plotted to facilitate a comparative analysis and to better understand their influence on the overall swelling behavior. Figure 4.49 and 4.50 shows the positive and negative electrodes volume expansion respectively.

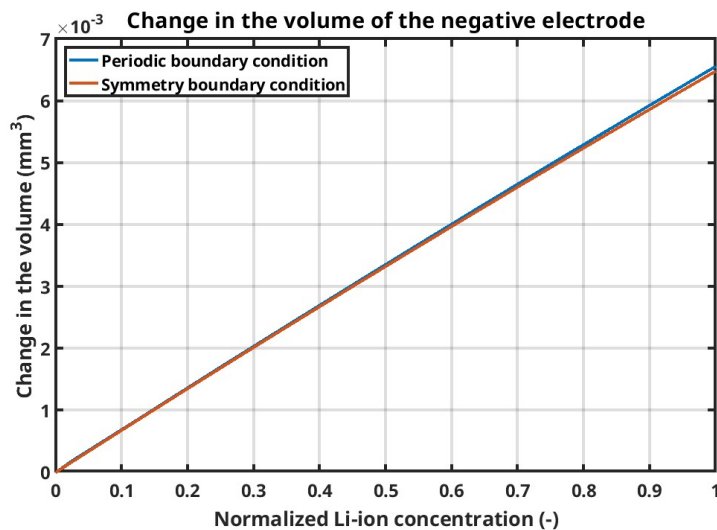


**Figure 4.49:** Change in the volume of the negative electrode.

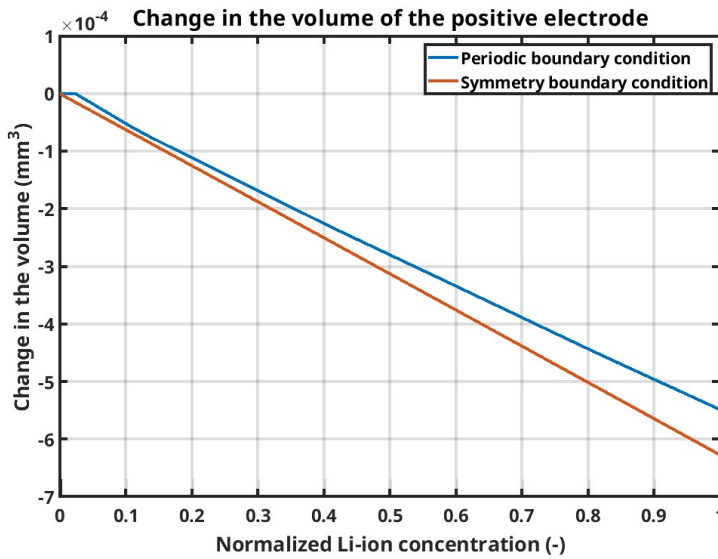


**Figure 4.50:** Change in the volume of the positive electrode.

From Figures 4.49 and 4.50, it is evident that the choice of boundary conditions has minimal impact on the expansion of the negative electrode. In contrast, the positive electrode exhibits a more pronounced response: under symmetry boundary conditions, the imposed constraints lead to a greater restriction on its volume expansion compared to the unconstrained case.

Figure 4.51 illustrate the effective volume expansion of the entire stack under both types of boundary conditions. Notably, the overall expansion is reduced when symmetry boundary conditions are applied, primarily due to the additional mechanical constraints imposed by this boundary setup.

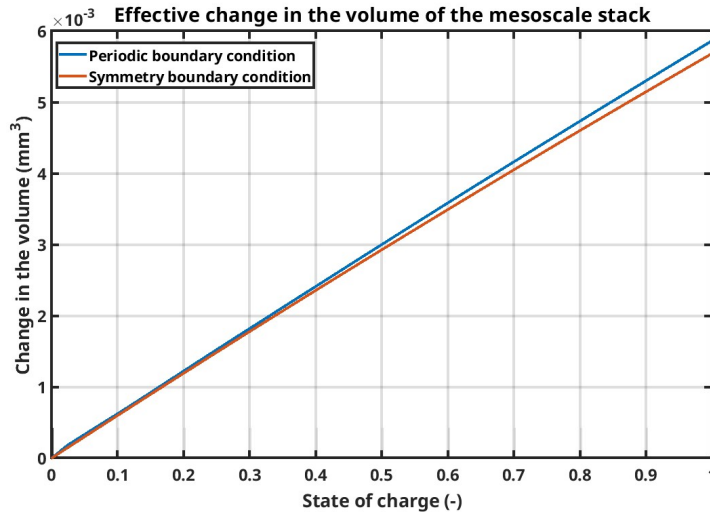


**Figure 4.51:** Effective change in the volume of the mesoscale stack.

## 4.3 Macroscale model

### 4.3.1 Homogenized material model characterization

The homogenized material behavior was characterized by virtually testing the mesoscale Representative Volume Element (RVE) under a macroscopic strain of 10%. The resulting stress-strain response was subsequently used to calibrate the effective material properties, using a crushable foam material model. Figure 4.52 illustrates the characterized response. This characterized response is further calibrated using crushable foam material model. The calibrated material properties are depicted in Table 4.11 and the hardening curve is depicted in Figure 4.53. The accuracy of the calibration was evaluated using the Root Mean Square Error (RMSE), which was found to be 0.003. It is important to note that the Poisson's ratio was not calibrated but was instead assigned a very small value, consistent with the behavior of foam-like materials.

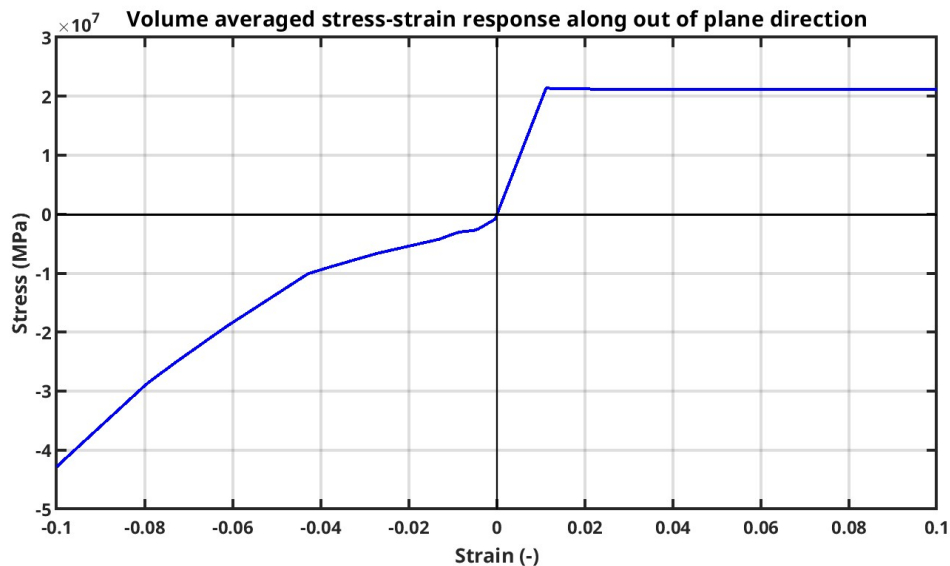
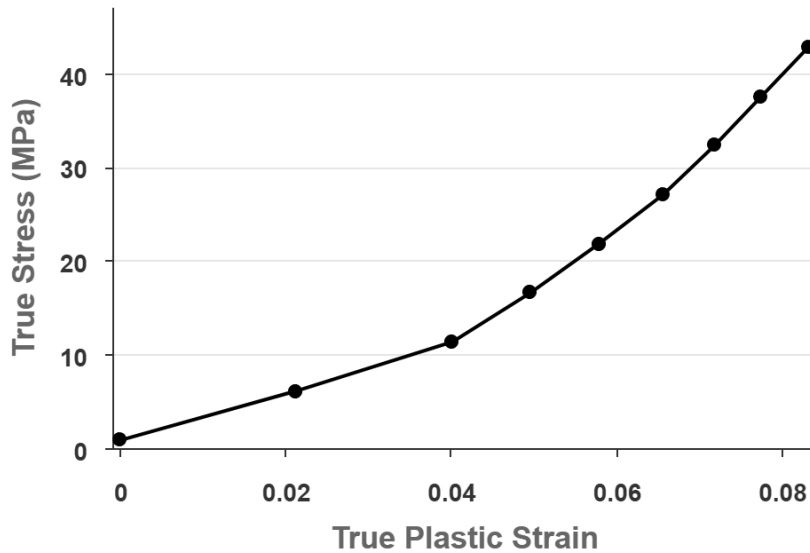


Figure 4.52: Characterized stress strain response along out of plane direction.

Parameter	Magnitude
Young's modulus (GPa)	1.9
Poisson's ratio	0.01
Compression stress ratio	2.99
Hydrostatic stress ratio	200

Table 4.11: Calibrated material properties of a homogenized jelly-roll.



**Figure 4.53:** Calibrated hardening curve.

As described in Subsection 3.4, the crushable foam formulation available in *3DEXPERIENCE* assumes an isotropic response in the elastic regime. Consequently, the material response is characterized in only one principal direction. However, in a typical jelly roll configuration comprising multiple layers, the material is often assumed to exhibit transversely isotropic behavior. In such cases, it becomes necessary to characterize the response not only in the out-of-plane direction but also in at least one of the in-plane directions to capture the transversely isotropic nature of the structure.

### 4.3.2 Cell level swelling response

The volumetric expansion of the mesoscale stack under periodic boundary conditions provides a more representative characterization of the jellyroll's expansion behavior. Consequently, the effective volumetric strain derived from this case is upscaled to the macroscale. This effective volumetric strain  $\bar{\varepsilon}_v^{ch}$  is used in the equation 3.23 to calculate the effective swelling coefficient of the homogenized jellyroll. Since, the change in the SOC is taken as 1, the calculated effective swelling coefficient of the homogenized jellyroll is equal to the effective volumetric strain.

The calculated effective swelling coefficient is introduced as a pseudo thermal expansion coefficient in the material card to model the swelling of the jellyroll due to change in the SOC. It has to be noted here that for the sake of simplicity, an isotropic volume expansion of the jellyroll is assumed. The Von-mises stress distribution in the homogenized jellyroll due to change in the SOC is illustrated in Figure 4.54.

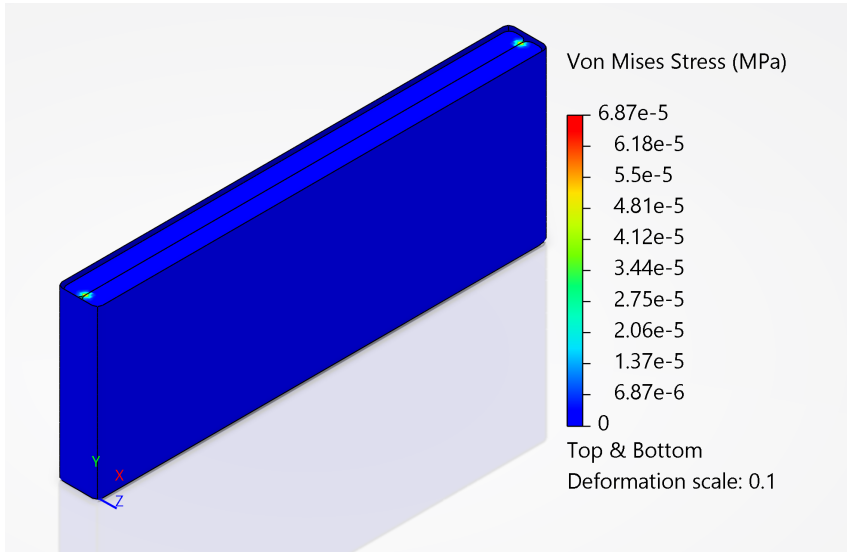


**Figure 4.54:** Contour plot illustrating the Von-mises stress distribution in the jellyroll.

The figures above show that the highest stress occurs near the junction of the two jellyrolls, caused by the sharp curvature at their interface.

The expansion of the jellyroll is assumed to be isotropic hence the expansion of the jellyroll along the three principal directions are identical. Figure 4.55 shows the expansion along X principal direction.

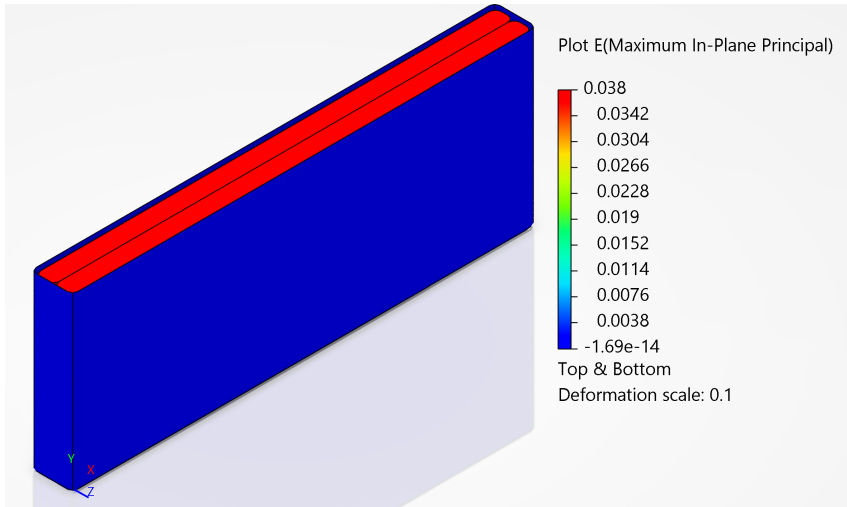


**Figure 4.55:** Strain induced in the jellyroll along X principal direction.

The effective volumetric strain induced due to the swelling of the jellyroll as a function of state of charge is shown in the Figure 4.56.

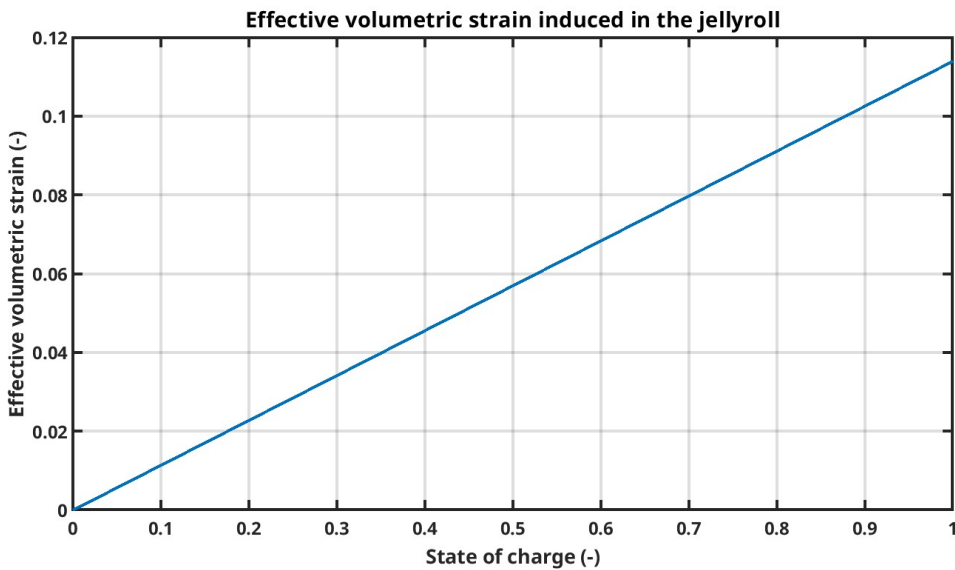


**Figure 4.56:** Effective volumetric strain induced in the jellyroll as a function of the state of charge.

It should be noted that the CAD model of the cell casing used in this study was constructed based on nominal dimensions. As a result, the expansion of the jellyroll does not lead to contact with the casing. Therefore, the effective stress response of the cell arises only due to the change in the SOC within the homogenized jellyroll. However, in reality, the expansion of the jellyroll leads to contact with the casing and that leads to introduction of the compressive stress on the jellyroll.

# 5

## Conclusion

This study presents a comprehensive multiscale modeling framework to simulate battery swelling induced by lithium-ion intercalation. The approach begins at the microscale, where the electrode microstructure is explicitly represented using a RVE. Within this RVE, the expansion of active material particles due to intercalation is simulated, and the mechanical contribution of the surrounding matrix is also accounted. The influence of matrix stiffness and volume fraction on the overall swelling behavior of the active particles is analyzed. Based on the microscale response, an effective swelling coefficient is derived for each electrode type, considering both linear and nonlinear material models. For simplicity, certain features such as the electrolyte and conductive additives are modeled as homogenized materials within the matrix phase. However, their explicit representation remains an important direction for future work to improve model fidelity. Moreover, since swelling is a long-term process involving electrolyte interactions, the use of more appropriate material models such as viscoelastic or viscoplastic formulations for the matrix phase is recommended. Strategies for determining the effective swelling coefficient under these material models require further investigation.

The effective swelling behavior derived from the microscale model is subsequently upscaled to the mesoscale by incorporating the effective swelling coefficients as functions of normalized lithium-ion concentration into the material cards of the electrodes. At this level, the model captures the behavior of an electrode stack, consisting of alternating layers of active materials, current collectors, and separators. Mechanical material response for these layers were characterized by performing uniaxial tensile and compression tests. Due to the time limitations, the physical tests were only performed on the negative electrode and separators. Due to limited availability of experimental data, stress-strain curves from the literature were utilized to calibrate the mechanical response of the electrodes, current collectors, and separators. At the mesoscale, both positive and negative electrodes are present. Therefore, coupled electrochemical-mechanical simulations were conducted to evaluate the change in stack volume as a function of change in the state of charge. Both free and constrained mechanical boundary conditions were applied and the sensitivity of effective volume change of the stack to external mechanical constraints were observed. The volumetric strain generated due to variations in the state of charge was then used to further upscale the expansion to the macroscale. For simplicity, the volume expansion was assumed to be isotropic. However, to improve the fidelity of the model, further characterization of anisotropic swelling behavior is recommended.

At the macroscale, the simulation is extended to the cell level, focusing on the volumetric expansion of the jellyroll in a prismatic cell as the state of charge evolves. Homogenization techniques are used to characterize the jellyroll as an effective material, eliminating the need to model each individual layer. For simplicity, the material response of the jellyroll is assumed to be isotropic. However, it should be noted that the actual material behavior of the jellyroll is transversely isotropic due to its layered structure. Therefore, future work should consider the implementation of transverse isotropy to improve model accuracy.

Through the developed methodology, the active particle level volume change can be efficiently upscaled to simulate the cell level volume expansion. The developed multiscale methodology enables both forward and reverse analysis. Swelling can be tracked from the particle level up to the full cell or electrode level, and conversely, deformations observed at the macroscopic level such as those induced by external constraints or pack integration can be projected back to assess their impact on the microstructure. Overall, this multiscale framework serves as a powerful tool for understanding and predicting failure mechanisms associated with swelling, including and not limiting to particle cracking and fracture at the microscale, binder detachment and electrode delamination at the mesoscale, and structural deformation or integrity loss at the cell and pack levels.

# 6

## Future scope

In this section, some recommendations for future works are presented based on the observations carried out in the work

### **Implementation of transversely isotropic crushable foam material and anisotropic swelling coefficient at the cell level:**

At the cell level, a homogenized material model was constructed by virtually testing the mesoscale model in a single direction, under the assumption of isotropic behavior. This simplification was necessitated by modeling limitations within the 3DEXPERIENCE platform. However, it is important to recognize that the mechanical response of the jellyroll structure is inherently transversely isotropic, due to its layered architecture and directional material properties. To more accurately capture this anisotropic behavior, future modeling strategies should aim to incorporate transverse isotropy into the homogenized model. One potential approach is to decouple the in-plane and out-of-plane responses, analogous to the transversely isotropic material formulations available in LS-DYNA. Additionally, incorporating anisotropic swelling coefficients would further enhance the fidelity of the cell-level response. This would allow for a more realistic representation of the jellyroll's mechanical behavior, particularly under conditions involving non-uniform swelling or directional loading.

### **Consideration of state of charge induced stiffness change:**

As discussed in the theoretical background, the lithiation and delithiation of lithium ions cause phase changes in the electrodes. These phase changes result in alterations to the material properties of the electrodes. Studies, such as [9] and [12], have shown that the lithiation process affects mechanical properties, leading to changes in stiffness, shifts in yield strength, and even a transition from ductile to brittle behavior. Therefore, to accurately predict the performance of batteries under operating conditions or during a mechanical abuse, it is essential to consider changes in material properties alongside swelling effects.

### **Consideration of irreversible swelling effects:**

Over time, the repeated cycling of batteries can lead to several irreversible effects that significantly impact their performance and safety. Key among these are the growth of the SEI layer, lithium plating, and degradation of the electrolyte. These

processes are not only detrimental to the battery's efficiency but also contribute to swelling, which can be a major safety concern. The swelling observed in batteries due to these irreversible changes can lead to a range of serious issues, including thermal runaway, separator failures, and an overall reduction in battery life. Given the potential consequences of these swelling effects, it is essential that the methodology developed in this study has to be extended to account for these irreversible processes.

**More accurate material model formulation for the microscale model:**

In this study, to access the binder's influence on the swelling behavior of active particles, both linear and crushable foam material models are used. It is essential to acknowledge that swelling occurs as a long-term process. Therefore, more advanced material models, such as viscoelasticity and viscoplasticity, are required to enhance the accuracy of the simulations regarding the binder's impact. These models provide a more comprehensive representation of the time-dependent properties of materials, facilitating a deeper understanding of how binders interact with active particles over time. By integrating the complexities associated with viscoelastic and viscoplastic behaviors, a methodology has to be created to simulate the mechanical and thermal responses of the binder as it deforms and evolves alongside the swelling of active particles.

**Improving the fidelity of the microscale model:**

In this study, the microscale model was developed by simplifying the microstructural complexity of the electrode. Only the binder phase and active material particles were considered, with the binder modeled as a homogenized medium, neglecting its inherent porosity. Additionally, the active particles were assumed to be uniform in size and shape, which further reduces the fidelity of the model. To enhance the accuracy and representativeness of the microscale model, future work should focus on incorporating more realistic microstructural features. One promising approach is to generate a RVE directly from high-resolution CT scan data, enabling the capture of actual particle geometries, size distributions, and binder-pore networks. This would allow for a more faithful representation of the mechanical interactions and failure mechanisms at the microscale. Moreover, improving the finite element formulation used in the microscale simulations is essential. Higher order and reduced integration element types or mesh refinement strategies could be employed to better capture the mechanical response without significantly increasing computational cost.

**Implementation of failure mechanisms to accurately capture the mechanical response due to swelling:**

In this study, failure mechanisms were not implemented to analyze the mechanical response to swelling. However, the developed methodology provides a robust framework that can be effectively applied to investigate failure phenomena across multiple length scales. For instance, at the microscale, the model can be used to study particle cracking induced by lithiation and the debonding of binder materials

resulting from volumetric expansion. At the electrode scale, it can capture critical failure modes such as the loss of electrical contact between active materials and current collectors, as well as mechanical degradation of the separator due to uneven swelling. At the cell level, the methodology is capable of simulating irreversible deformations and structural instabilities driven by cumulative swelling effects, which can compromise the mechanical integrity and performance of the entire battery system.

### **Characterizing Mechanical Properties of Electrodes and Separator**

To improve the accuracy of the multiscale modeling framework presented in this thesis, future work should focus on experimentally characterizing the material behavior of the electrodes and separator. Due to the time constraints and safety concerns, the physical testings to characterize the material response were limited to negative electrode and separator. Therefore, this study mainly relied on material data from existing literature, which limits the reliability in the calibrated results. For more reliable predictions, future experiments should include standard tests such as uniaxial tension and compression, as well as biaxial tension tests, to capture how each material responds under different types of loading. Achieving consistent and accurate results will require careful sample preparation, multiple sample tests under same load condition, strict environmental control, and use of advanced techniques like Digital Image Correlation (DIC) to capture strain distribution across the entire sample. Furthermore, investigating the effects of different strain rates will support the development of more comprehensive material models, including viscoelastic or viscoplastic formulations, for future simulations.

# A

## Appendix A: Electrochemical definitions

This section discusses the key terms involved in the DFN model.

**Exchange current Density  $I_o$ :** Exchange current density describes the baseline electrochemical reactions when there is no overpotential. The higher the exchange current density, the faster the reaction takes place.  $I_o$  is typically expressed in  $\text{A}/\text{m}^2$ .

**Overpotential  $\eta$ :** Overpotential describes the additional voltage required from the open circuit voltage to drive the electrochemical reactions. For Potentiostatic charging case, the applied voltage corresponds to the overpotential. Whereas for the galvanostatic case, the overpotential is computed through the applied current. The unit of overpotential is Volts (V).

**Lithium ion concentration in solid  $c_s$ :** Lithium ion concentration in solid represents the amount of lithium ions present in the active particle and usually given in  $\text{mol}/\text{m}^3$ .

**Lithium ion concentration in electrolyte  $c_e$ :** Lithium ion concentration in electrolyte represents the amount of lithium ions present in the liquid phase in the battery domain and usually given in  $\text{mol}/\text{m}^3$ .

**Transference number  $t_+$ :** represents the fraction of current carried by the lithium ions in the electrolyte phase. Transference number is dimensionless.

**Charge transfer coefficients of anode and cathode  $\alpha_a$  and  $\alpha_c$ :** represents how the applied voltage affects the rate of the oxidation and reduction reactions. The charge transfer coefficients are dimensionless.

**Faraday's constant  $F$ :** represents the charge of one mole of electrons. The magnitude is approximately 96485 C/mol.

**Universal gas constant  $R$ :** represents the amount of energy associated with each mole of gas molecules for each degree of temperature increase. The magnitude is approximately 8.314 J/(mol·K).

**Open circuit potential  $E_{ocp}$ :** represents the potential of the electrodes when no

external current is applied. The open circuit potential is usually measured in volts (V).

# B

## Appendix B: Calibrated material properties of electrodes and separator

In this Appendix, the calibrated material hardening curves are depicted along with the calibrated material properties.

**Negative electrode active material:**

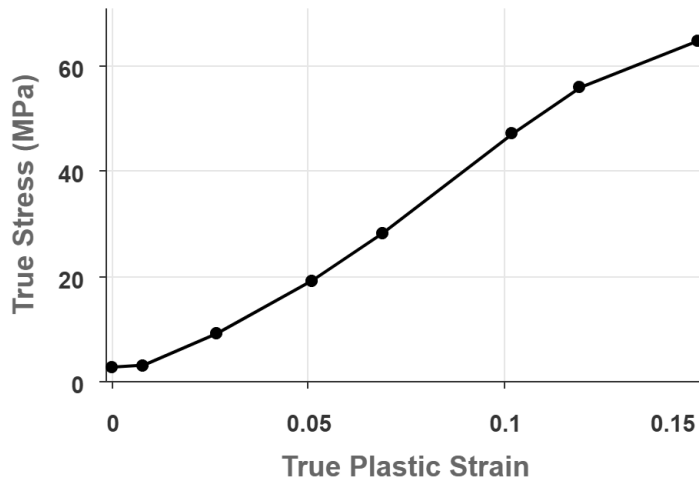


**Figure B.1:** Calibrated hardening curve of the negative electrode.

Parameter	Magnitude
Young's modulus (GPa)	2.293
Poisson's ratio	0.01
Compression stress ratio	2.99
Hydrostatic stress ratio	8.258

**Table B.1:** Calibrated properties of the negative electrode active material.

**Negative current collector:**

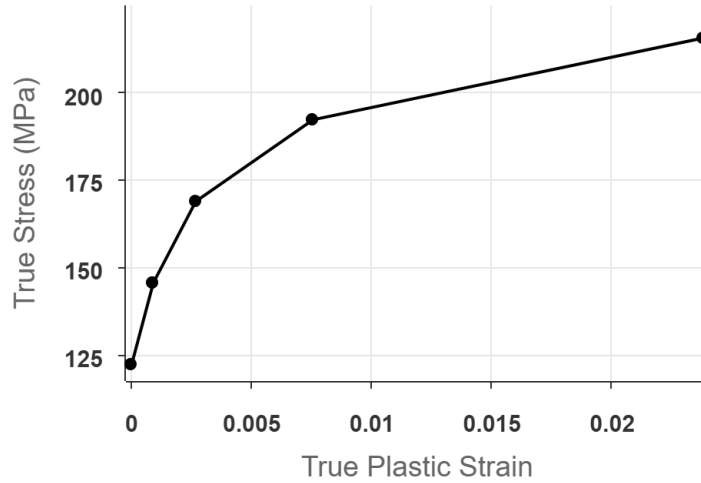


**Figure B.2:** Calibrated hardening curve of the negative current collector.

Parameter	Magnitude
Young's modulus (GPa)	53.6
Poisson's ratio	0.33

**Table B.2:** Calibrated properties of the negative electrode current collector.

Separator:

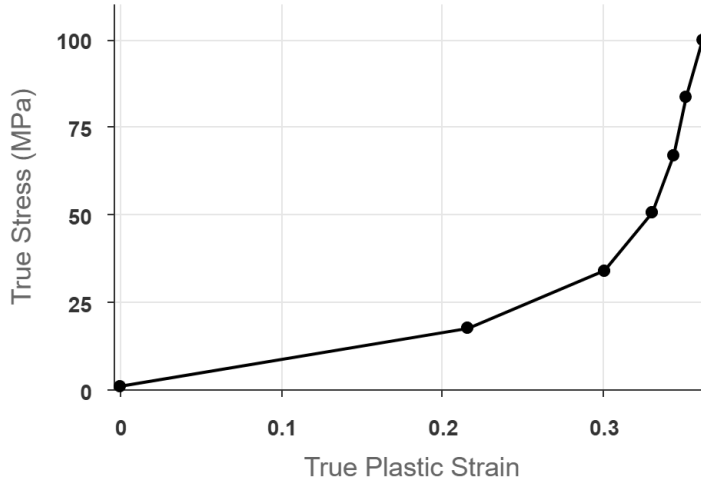


**Figure B.3:** Calibrated hardening curve of the separator.

Parameter	Magnitude
Young's Modulus (GPa)	0.612
Poisson's ratio	0.01
Compression stress ratio	2.99
Hydrostatic stress ratio	190.97

**Table B.3:** Calibrated properties of separator.

**Positive electrode active material:**

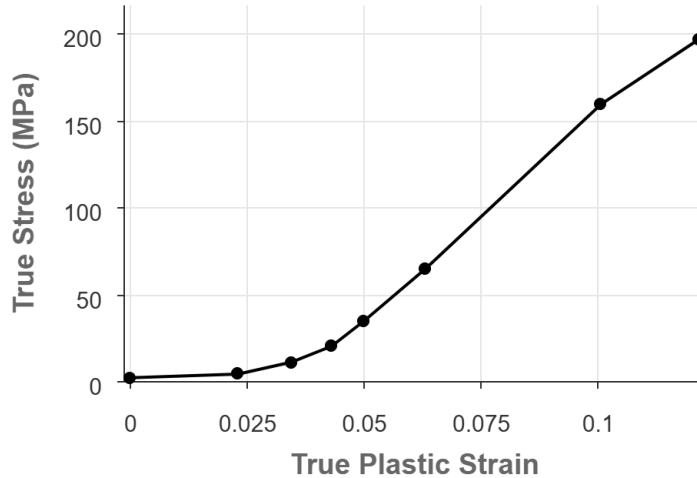


**Figure B.4:** Calibrated hardening curve of the positive electrode active material.

Parameter	Magnitude
Young's modulus (GPa)	1.78
Poisson's ratio	0.01
Compression stress ratio	2.99
Hydrostatic stress ratio	8.79

**Table B.4:** Calibrated properties of positive electrode active material.

**Positive electrode current collector:**

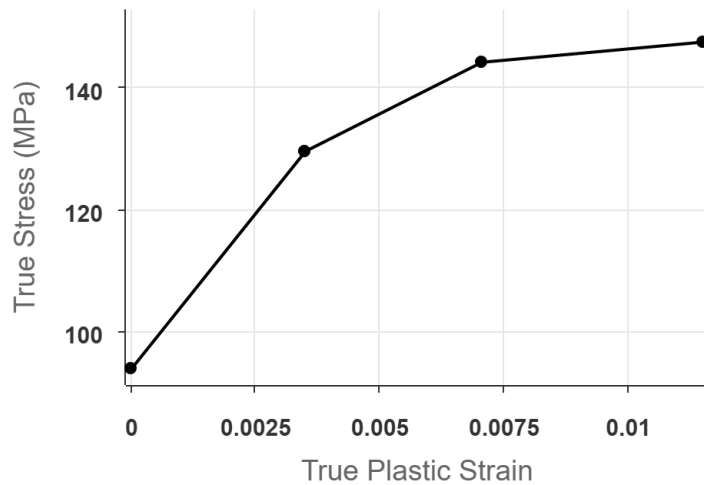


**Figure B.5:** Calibrated hardening curve of the positive current collector.

Parameter	Magnitude
Young's modulus (GPa)	490.09
Poisson's ratio	0.33

**Table B.5:** Calibrated properties of positive electrode active material.

# Bibliography

- [1] Elham Sahraei, Emanuela Bosco, Brandy Dixon, and Benjamin Lai. Microscale failure mechanisms leading to internal short circuit in li-ion batteries under complex loading scenarios. *Journal of Power Sources*, 319:56–65, 2016.
- [2] R. Spotnitz and J. Franklin. Abuse behavior of high-power, lithium-ion cells. *Journal of Power Sources*, 113(1):81–100, 2003.
- [3] S. S. Zhang. The effect of the charging protocol on the cycle life of a li-ion battery. *Journal of Power Sources*, 161(2):1385–1391, 2007.
- [4] Ankeet Mohan Purantagi. Predicting short circuit of li-ion battery cells during mechanical abuse. *MSc Thesis, Chalmers University of Technology*, 2024.
- [5] Amit Chetry. Mechanical material modelling and characterisation of li-ion battery. *MSc Thesis, Chalmers University of Technology*, 2024.
- [6] Albin Knutsson and Jonas Trombatti. Finite element modelling of cell swelling for traction batteries. *MSc Thesis, Chalmers University of Technology*, 2021.
- [7] Priyank Gupta and Peter Gudmundson. Modeling of local electrode stresses and pressures in lithium-ion battery packs using three-dimensional homogenization. *Journal of Power Sources*, 582:233514, 2023.
- [8] Dassault Systèmes. Coupled thermal-electro-chemical analysis, 2025.
- [9] Yue Qi, Louis G Hector, Christine James, and Kwang Jin Kim. Lithium concentration dependent elastic properties of battery electrode materials from first principles calculations. *Journal of The Electrochemical Society*, 161(11):F3010, 2014.
- [10] Yangzheng Cao, Huacui Wang, Binghe Liu, and Jun Xu. Modeling, validation, and analysis of swelling behaviors of lithium-ion batteries. *Journal of Energy Storage*, 74:109499, 2023.
- [11] Mehdi Gilaki and Elham Sahraei. Modeling state-of-charge dependent mechanical response of lithium-ion batteries with volume expansion. *Energy Reports*, 12:3607–3619, 2024.
- [12] Yanan Wang, Ruke Ni, Xingbao Jiang, Mingyue Yin, Dejun Zhang, and Zongfa Xie. An electrochemical-mechanical coupled multi-scale modeling method and full-field stress distribution of lithium-ion battery. *Applied Energy*, 347:121444, 2023.
- [13] Lubing Wang, Sha Yin, Chao Zhang, Yong Huan, and Jun Xu. Mechanical characterization and modeling for anodes and cathodes in lithium-ion batteries. *Journal of Power Sources*, 392:265–273, 2018.
- [14] Kannan Zhao, Matt Pharr, Joost J Vlassak, and Zhigang Suo. Large deformation and electrochemically induced mechanical degradation of high-capacity

- lithium-ion battery electrodes. *Journal of the Mechanics and Physics of Solids*, 60(10):1810–1822, 2010.
- [15] M Doyle, TF Fuller, and J Newman. Modeling of galvanostatic charge and discharge of the lithium/polymer/insertion cell. *Journal of the Electrochemical Society*, 140(6):1526–1533, 1993.
  - [16] Sandeep Kulathu, Juan A Hurtado, Kingshuk Bose, Youngwon Hahn, Pavel A Bouzinov, Robert L Taylor, and Victor Oancea. A three-dimensional thermal-electrochemical-mechanical-porous flow multiscale formulation for battery cells. *International Journal for Numerical Methods in Engineering*, 125(13):e7464, 2024.
  - [17] Xuekun Lu, Antonio Bertei, Donal P Finegan, Chun Tan, Sohrab R Daemi, Julia S Weaving, Kieran B O'Regan, Thomas MM Heenan, Gareth Hinds, Emma Kendrick, et al. 3d microstructure design of lithium-ion battery electrodes assisted by x-ray nano-computed tomography and modelling. *Nature communications*, 11(1):2079, 2020.
  - [18] Golriz Kermani and Elham Sahraei. Characterization and modeling of the mechanical properties of lithium-ion batteries. *Energies*, 10(11):1730, 2017.
  - [19] Kenneth Runesson and Ragnar Larsson. Constitutive modeling of engineering materials - theory and computation. *Lecture Notes, Department of Industrial and Materials Science, Chalmers University of Technology, Gothenburg*.
  - [20] LJ Gibson and MF Ashby. The mechanics of foams: basic results. *Cellular Solids: Structure and Properties*, 2:175–234, 1997.
  - [21] Markus Spielbauer, Franziska Peteler, András Németh, Jonas Soellner, Philipp Berg, Oliver Bohlen, and Andreas Jossen. An analysis of the current state and obstacles in discrete layered finite element simulation of crushing cylindrical lithium-ion cells. *Journal of Energy Storage*, 72:108029, 2023.
  - [22] Johannes Landesfeind and Hubert A Gasteiger. Temperature and concentration dependence of the ionic transport properties of lithium-ion battery electrolytes. *Journal of The Electrochemical Society*, 166(14):A3079–A3097, 2019.
  - [23] Madeleine Ecker, Thi Kim Dung Tran, Philipp Dechent, Stefan Käbitz, Alexander Warnecke, and Dirk Uwe Sauer. Parameterization of a physico-chemical model of a lithium-ion battery: I. determination of parameters. *Journal of The Electrochemical Society*, 162(9):A1836, 2015.

**Department of Industrial and Materials Science**

**CHALMERS UNIVERSITY OF TECHNOLOGY**

Gothenburg, Sweden

[www.chalmers.se](http://www.chalmers.se)



**CHALMERS**  
UNIVERSITY OF TECHNOLOGY